DESIGN AND DEVELOPMENT OF NOVEL ELECTRIC DRIVES FOR SYNCHRONOUS RELUCTANCE AND PM SYNCHRONOUS MACHINES

Lesedi Melton Masisi

A Thesis

In the Department

of

Electrical and Computer Engineering

In Partial Fulf llment

of the Requirements for the Degree

Doctor of Philosophy (Electrical and Computer Engineering) at

Concordia University

Montreal, Quebec, Canada

April 2015

CONCORDIA UNIVERSITY
SCHOOL OF GRADUATE STUDIES

This is to certify that the thesis prepared

By: Lesedi Melton Masisi

Entitled: Design and Development of Novel Electric Drives for Synchronous Reluctance and PM Synchronous Machines

and submitted in partial fulfillment of the requirements for the degree of

Doctor of Philosophy (Electrical and Computer Engineering)

complies with the regulations of the University and meets the accepted standards with respect to originality and quality.

Signed by the final examining committee:

_____ Chair
Dr. A. Dolatabadi

_____ External Examiner
Dr. B.N. Singh

_____ External to Program
Dr. S. Rakheja

_____ Examiner
Dr. S. Hashtrudi Zad

_____ Examiner
Dr. L.A.C. Lopes

_____ Thesis Co-Supervisor
Dr. P. Pillay

_____ Thesis Co-Supervisor
Dr. S. Williamson

Approved by: _____
Dr. A.R. Sebak, Graduate Program Director

March 26, 2015 _____
Dr. A. Asif, Dean
Faculty of Engineering & Computer Science

ABSTRACT

Design and Development of Novel Electric Drives for Synchronous Reluctance and PM Synchronous Machines

Lesedi Melton Masisi, PhD.
Concordia University, 2015

Permanent magnet synchronous machines (PMSMs) with rare-earth magnets are widely used by the hybrid electric and electric vehicle industry due to their high torque density and efficiency. However the increasing fluctuating prices of the rare earth magnets have triggered the search for other alternative electrical machines such as the induction machine (IM), synchronous reluctance machine (SynRM) and a variable flux machine (VFM). The SynRM and the variable flux machine have been identified as potential PMSMs replacement. This is because the control strategy for the SynRM is closer to the PMSM and that the VFM is a PMSM. Therefore the same hardware used for the PMSM drive can be used for the SynRM and the VFM.

There has also been an increasing demand for higher dc bus voltage on the electric drive train for better performance. A three level inverter has been identified as the best candidate to meet this demand. Hence the thesis presents a three level inverter neutral point clamped SynRM drive for traction applications. A new space vector modulation scheme is also

proposed for the three level inverter SynRM drive. A comparison between a three and two level inverter SynRM drives was also conducted.

Due to high cost associated with EV/HEVs, a low cost high resolution position sensor is proposed for the SynRM and the variable flux machine drives. The low cost position sensor is also compared to the position sensor used in electric power steering (EPS) machine. The EPS machines are predominantly used in vehicles and the low cost position sensor is proposed as a best alternative for the position sensor used in the EPS machine due to their simpler algorithm for position information, higher resolution and cost reduction benefits.

The effect of the three level inverter supply on the core losses of the SynRM was also conducted. The SynRM experienced lower core losses when supplied from a three level inverter. The reduction in the core losses is more significant in the stator tooth which is harder to cool as compared to the stator yoke. Hence the additional benefit of a three level inverter SynRM drive is that the burden of the cooling system will be reduced and hence a reduction in the cost associated with machine cooling.

The thesis also presents a novel control strategy for a variable flux machine (VFM) which uses low cost aluminum-nickel-cobalt (AlNiCo) permanent magnets (PMs). The strategy implements field weakening for speed extension and takes into account the de-magnetization characteristics of the AlNiCo magnets. The magnet flux is reduced from the armature current pulses thus eliminating the additional copper losses associated with the

f ux weakening current in conventional rare earth PMSMs. The performance of the core losses on the VFM are also evaluated and quantif ed.

ACKNOWLEDGEMENTS

I want to thank my supervisor and co-supervisor, Dr Pragasen Pillay and Dr Sheldon S. Williamson for their scientif c input and guidance during my PhD program. I am forever grateful to have been under the supervision of a visionary and deeply caring person. I would also like to thank the committee members, who helped me sharpen the research work i was involved in through their recommendations.

My deepest gratitude goes to my mother and late father who remained patient and supported me to achieve my goals. Many thanks to my lab-mates through whom i could experience a world class research environment. Special thanks to Mr Chirag Desai who helped with gaining necessary tools to complete my experimental work. I feel that my supervisor, co-supervisor and all my lab-mates were a family. We had times of great sadness and i am thankful for the support i received. I thank God for this priceless experience in my life.

This work was f nancially supported in part by the R&D program of the NSERC Chair entitled ”Design and Performance of Special Electrical Machines” at Concordia University. The authors acknowledge the support of the Natural Sciences & Engineering Research Council of Canada, Hydro-Qubec and the National Research Foundation (NRF) of South Africa.

DEDICATION

To my Mother, Elva Modiegi Masisi and late father Mr Rathapelo Samuel Masisi who as a teacher contributed to the education of young people for the betterment of our society...

TABLE OF CONTENTS

LIST OF TABLES

LIST OF FIGURES

Nomenclature

HEV	Hybrid Electric Vehicle
EV	Electric Vehicle
PMSM	Permanent Magnet Synchronous Machine
IM	Induction Machine
SynRM	Synchronous Reluctance Machine
VF-IPMSM	Variable Flux Insert Permanent Magnet Synchronous Machine
VFM	Variable Flux Machine
NPC	Neutral Point Clamped
3L-INV	Three Level Inverter
2L-INV	Two Level Inverter
NP	Neutral Point
dc	Direct Current
SVM	Space Vector Modulation
PWM	Pulse Width Modulation
FOC	Field Oriented Control
EPS	Electric Power Steering

List of Symbols

D	Direct
Q	Quadrature
i_d	D-axis current
i_q	Q-axis current
I_s	Peak Input stator current
i_a	Armature phase a current
i_b	Armature phase b current
i_c	Armature phase c current
L_d	D-axis inductance
L_q	Q-axis inductance
λ_{af}	Magnet linkage Flux
λ_d	D-axis Llnkage Flux
λ_q	Q-axis linkage Flux
R_s	Phase resistance
V_q	Q-axis voltage
V_d	D-axis voltage
T_L	Load torque
T_e	Electrical torque
P	Pole pairs
k	Saliency ratio

m_i	Modulation index
d_S	Duty cycle of small vectors
d_M	Duty cycle of medium vectors
d_L	Duty cycle of Large Vectors
V_S	Small vector voltage state
V_M	Medium vector voltage state
V_L	Large vector voltage state
Δ_n	Triangle n
θ_r	Rotor position
θ_s	Current phasor angle
ω_m	Mechanical speed
ω_e	Inverter frequency in rad/s
φ	Power factor angle
U	Eff ciency
P_o	Power output
P_{in}	Power input
f	Frequency
I_o	Output current
V_{NP}	Neutral point voltage
V_{NPn}	Normalized neutral point voltage
I_{np}	Neutral point current
B	Flux density

B_r	Remnant f ux density
B_i	Intrinsic f ux density
H_a	Demagnetization f eld intensity
B_s	Saturated f ux density

CHAPTER I

INTRODUCTION

1.1 Research Background

The demand for hybrid electric vehicles (HEVs) has been at an increase in the recent years. Already the province of Quebec has invested 250 million dollars to have 15 % of the vehicles electric by 2025 [2]. The desire to reduce the carbon footprint in many countries means that electric vehicles play an integral role in the carbon emissions reduction. The permanent magnet synchronous machine (PMSM) is one of the desirable candidates for HEV applications. This is because it has a relatively high torque density and energy per mass [3, 4]. Considering the limited space in the vehicles these machines can be designed to f t in relatively small areas in the vehicle.

The PMSM makes use of rare earth permanent magnets which inherently create a magnetic f ux in the machine. Hence there is no need for the stator excitation current to establish the magnetic f ux. In general the performance of this machine far outweighs machines that do not have permanent magnets because of the presence of the magnetic f eld in the machine. This has led to such machines being the most preferred for HEV applications where both space and energy supply are limited. However the great challenge with the rare earth permanent magnets is that they are predominantly produced in China and their prices f uctuates often. In recent years rare earth permanent magnets have recorded an increase in prices. This has raised concerns in the HEV vehicle industry on the use of PM machines

for mass HEV production. Alternate machines are therefore being explored as a substitute. These alternatives include the SynRM and the variable f ux PM machine.

Firstly the preference for the SynRM is due to the following:

- The SynRM like the induction machine does not make use of permanent magnets
- It uses a similar stator to that of the PM machine and induction machine
- Unlike the induction machine (IM) and other machines, the control strategies used for the the PMSM machine are similar to that of the SynRM. This means that the same hardware used for the PM machine can be used for the SynRM
- Due to the absence of magnets it is more reliable than the PMSM
- Unlike the induction machine, there are no rotor coils, hence depending on the size of the machine the SynRM may have higher eff ciencies as compared to the IM at almost the same power densities

However it has the following challenges:

- Poor power factor
- Limited constant power range in the f eld weakening region due to poorer power factor and cross coupling effects

The SynRM is regarded as a good alternative to the induction machine (IM) since the same hardware used to drive the PMSM can be used for the SynRM. When compared to the IM the SynRM has a higher eff ciency with a competitive torque/ampere, this was extensively illustrated by [5] and [4]. It is shown in [6] that the SynRM competes well

with the induction machine counterpart at rated power of 110 kW for traction applications. Extensive work has also been conducted validating the viability of the SynRM as compared to the induction machine [7, 8, 9]. The work in [10, 11, 12] proved that the SynRM is a potential candidate for traction applications.

Secondly, the reason why the variable flux machine VFM which uses AlNiCo magnets was identified as an alternative is because of the following:

- The VFM makes use of low coercive magnetic field magnets which are relatively low cost magnets as compared to rare earth magnets
- AlNiCo magnets can operate at flux densities close to rare earth magnets
- The VFM is a permanent magnet synchronous machine hence the same hardware can be used for the control
- The efficiency of the machine can be improved most especially in the field weakening region. This is a great advantage for HEV/EVs due their limited energy supply

However one major disadvantage is that the VFM requires a relatively larger inverter due to the remagnetization currents which are higher than the continuous machine current. However as compared to other low coercive magnetic field magnets such as samarium cobalt (Sm-Co), the AlNiCo magnets have a relatively lower coercive magnetic field. Hence they have a relatively lower remagnetization current which contributes to the reduction of the converter size.

For traction applications there is an increasing demand for higher dc bus voltage for better performance (acceleration and braking) and a three level neutral point clamped (NPC)

inverter has been identif ed as the suitable converter to satisfy this demand. As compared to a two level inverter the three level inverter uses four switches in a leg. This allows for higher dc bus voltages at lower power rated switches since each switch experiences almost half the dc bus voltage.

Since the switching of the devices occurs across a lower voltage, the three level inverter has lower THD as compared to the two level inverter due to lower voltage change rate (dV/dt). The three level inverter is part of the multilevel converter family which were introduced in the year 1975. The other two most basic well known topologies are the cascaded H-bridge multilevel converter (CHB) and the f ying capacitor multilevel converter (FCC) [13].

With the increase dc bus voltage demand a two level inverter will result in higher common mode voltage which worsens at higher switching frequencies [14]. The common mode voltages appear across the motor shaft and ground which in turn results in shafts currents which cause early bearing failures. The three level inverter can be used to combat these problems, since it generates lower dv/dt as compared to the two level inverter.

The three level inverter makes use of two capacitors so as to create a zero voltage state. Thus one of the major challenges with a three level inverter is to have the same voltage across the capacitors. Hence in recent years there has been a number of research works for balancing algorithms [15, 16, 17]. A suitable balancing algorithm is required for the SynRM due to the relatively low power factor of the machine. The effects of the three level inverter supply on the SynRM needs to be established, most especially for traction applications where the energy source is limited.

The SynRM and the PMSM have unique rotor geometries and hence require rotor position information. The rotor position information is necessary for the implementation of vector control for the machine. However conventional position sensors are costly which results in higher production costs of the electric drive. For this reason there has been a number of research works on the use of sensor-less electric drives. However due to safety concerns sensor-less control has not gained much conf dence for traction applications. In line with reducing the production cost of HEV/EVs another alternative is to use a low cost position sensor in the electric drive train, while retaining the robustness and safety of the electric drive.

A large number of electric power steering (EPS) machines makes use of digital Hall sensors for rotor position information which are more costly as compared to the low cost position sensor. It is a part of this research to propose the use of a Hall effect low cost high resolution position sensor to reduce the cost of electric vehicles.

1.2 Objectives

The objectives of this thesis are:

- The f rst goal of this thesis is to develop a three level inverter SynRM drive. A new space vector pulse width modulation (SV-PWM) scheme for the balancing of the dc link capacitor voltages is proposed. This scheme should be able to handle a non-linear load which has a low power factor such as a SynRM. This goal also entails a method of sizing the dc link capacitors taking to consideration the saliency ratio of the SynRM and other machine parameters. This also entails a comparison between certain parameters of the machine when driven from two or three level inverters.

- The second goal of this thesis is aimed at reducing the cost of the SynRM electric drive by the implementation of a low cost position sensor. A low cost position sensor is necessary for vector control. This further includes a comparison between the low cost position sensor and the position sensor predominantly used in the electric power steering machines. The aim here is to propose the low cost position sensor as better alternative for the position sensor used in the EPS machines.

- The third goal of the thesis is to quantify the effect of the use of a three and two level inverter on the core losses of the SynRM. The core losses of the machine contribute toward the heating of the machine. Hence this could result in the reduction of the burden of the cooling system on the machine and hence reduce cost associated with the cooling system.

- This thesis also aims to develop a control strategy for a variable flux machine for traction applications which uses AlNiCo magnets. The controller should have field weakening ability for speed extension and also take into account the demagnetization characteristics of the AlNiCo magnets.

- Examine the core loss performance of the VFM at different magnetization levels

1.3 Thesis Outline

The thesis is organized as follows:

Chapter 2 is concerned with the development of a three level neutral point clamped (NPC) inverter SynRM drive. Two space vector modulation (SVM) algorithms are implemented and compared. The sizing of the dc bus link capacitors using the SynRM saliency is also

investigated. The two and three level inverter drives are also compared with special attention to the d-axis current ripple which is an indicator for the iron losses in the machine.

Chapter 3 presents the use of a low cost position sensor for the retrieval of the rotor position information. In this work sources of errors are also reviewed. A comparison between the low cost position sensor and the position sensor used in the EPS machine is also conducted

Chapter 4 conducts a comparison between core losses of the SynRM machine under a two and three level inverter supply. Two methods are implemented, f rstly, the use of f nite element analysis software is used to extract the f ux densities for the core loss measurements. Secondly, the inverters are directly connected to the stator toroid of the SynRM for core loss measurements. Chapter 5 presents the characterization of the VFM and the development of a vector control strategy for a variable f ux machine (VFM) using AlNiCo magnets and the performance of the core loss at different magnetization levels. Chapter 6 presents the conclusion of the thesis.

1.4 Thesis Contributions

Chapter 2:

- A three level inverter SynRM electric drive was developed. In this work a new balancing algorithm for the capacitor voltages was developed called Mod-1. A comparison between the proposed modulation scheme and the existing modulation scheme was also conducted. Mod-1 scheme was further modif ed in order to attain a f xed switching frequency of the inverter. A comparison between the two and three level inverter SynRM drives was also conducted. The three level inverter provided relatively better power quality for the SynRM.

Chapter 3:

- The use of a low cost high resolution position sensor for a SynRM electric drive was also implemented. This work showed the feasibility of the use of a low cost position sensor for a SynRM and hence will contribute to the reduction of the SynRM drive cost. A comparison between the low cost position sensor with a position sensor used in the commercial EPS machine was also conducted. In this work the low cost position sensor is proposed as a best alternative for the position sensor used in the EPS machine due to a simpler algorithm for position information, higher resolution and cost reduction benef ts.

Chapter 4:

- The investigation of the effect of the three level inverter on the core losses of the SynRM was conducted. The SynRM under a three level inverter supply registered lower core losses as compared to the two level inverter SynRM drive. The core losses were more signif cant in the stator tooth which is usually harder to cool. The use of a three level inverter on the SynRM does not only provide good quality power, but will also reduce the burden of the cooling system.

Chapter 5:

- The development of a new vector control strategy for a variable f ux machine using AlNiCo magnets. The magnetization and demagnetization processes were conducted from the armature by a current pulse. The strategy took into account the demagnetization characteristics of the magnets and implemented f eld weakening for speed extension and smoother transitions through different magnetization levels. The magnet

f ux can be weakened avoiding the additional copper losses due to the f ux weakening current of the rare-earth PMSMs.

- Core loss performance of the VFM under difference magnet f ux levels was also examined.

The following are the technical output of the presented research work in this thesis:-

Journal Papers

1. L. Masisi, P. Pillay and S. Williamson, ”High-resolution Low-cost Rotor Position Sensor for Traction Applications,” submitted to the IEEE Transactions on Industrial Electronics (Letters to the Editor).

2. L. Masisi, P. Pillay and S. Williamson, ”Comparison of Two Modulation Strategies for a Three Level Inverter Synchronous Reluctance Motor (SynRM) Drive,” submitted to the IEEE Transactions on Industrial Applications.

3. L. Masisi, P. Pillay and S. Williamson, ”A Three Level Neutral Point Clamped (NPC) Inverter Synchronous Reluctance Machine (SynRM) Drive,” submitted to the IEEE Transactions on Industrial Applications.

4. M. Ibrahim, L. Masisi and P. Pillay, ”Design of High Torque Density Variable Flux Permanent Magnet Machine Using Alnico Magnets,” submitted to IEEE Transactions on Industry Applications.

5. M. Ibrahim, L. Masisi and P. Pillay, ”Design of Variable Flux Permanent Magnet Machine for Reduced Inverter Rating,” submitted to IEEE Transactions on Industry Applications (accepted).

Conference Papers

1. L. Masisi, M. Ibrahim, P. Pillay, ”Control Strategy of A Variable Flux Machine Using AlNiCo PMs,” submitted to the Energy Conversion Congress and Exposition (ECCE) 2015.

2. L. Masisi, M. Ibrahim, P. Pillay, ”The Effect of the Three Level Neutral Point Clamped (NPC) Inverter on the Core Loss of a Synchronous Reluctance Machine,” submitted to the Electric Machines and Drives Conference (IEMDC) 2015 (accepted).

3. L. Masisi, A. Takbash, P. Pillay, ”Core Loss Performance of a New PM Machine Topology for Electric Vehicles,” submitted to the Electric Machines and Drives Conference (IEMDC) 2015 (accepted).

4. L. Masisi, P. Pillay and S. Williamson, ”Comparison of Two Modulation Strategies For a Three Level Inverter Synchronous Reluctance Motor (SynRM) Drive,” in Industry Applications Society Annual Meeting, 2014 IEEE, Oct 2014, pp. 1-7.

5. L. Masisi, P. Pillay, and S. Williamson, ”Three Level NPC Inverter DC Capacitor Sizing For a Synchronous Reluctance Machine Drive,” in Energy Conversion Congress and Exposition (ECCE), 2014 IEEE, Sept 2014, pp. 2925-2931.

6. L. Masisi, A. Choudhury, P. Pillay, and S. Williamson, ”Performance comparison of a two-level and three-level inverter permanent magnet synchronous machine drives for hev application,” in Industrial Electronics Society, IECON 2013 - 39th Annual Conference of the IEEE, Nov 2013, pp. 7262-7266.

7. L. Masisi, S. Williamson, and P. Pillay, ”A Comparison Between a 2-Level and 3-Level Inverter For a Permanent Magnet Synchronous Motor Drive Under Different Inverter switching frequencies,” in Power Electronics, Drives and Energy Systems (PEDES), 2012 IEEE International Conference on, Dec 2012, pp. 1-5.

CHAPTER II

THREE LEVEL INVERTER SYNCHRONOUS RELUCTANCE MOTOR DRIVE

2.1 Introduction

The three level inverter makes use of two dc bus capacitors so as to create a neutral point (NP) for certain voltage states. A major challenge with a three level inverter is the balancing of the two dc bus capacitors. There has also been great interest in the development of the capacitor voltage balancing algorithms [15, 16, 17, 18]. Comprehensive work detailing the cause of the low frequency NP voltage was conducted by [19]. Hybrid modulation techniques have also been developed to completely suppress the NP voltage ripple [20, 21]. These strategies combine two modulation schemes, the nearest three vector (NTV) with a non-NTV algorithm. One drawback with the hybrid strategy is the increase in converter losses, such that a certain trade off has to be made between either suppressing the NP voltage ripple or increasing converter losses [20].

Most of the research has been focused on the converter. In this work two capacitor voltage balancing strategies used in a converter for a SynRM application are compared. The two strategies will be referred to as Mod-1 and Mod-2. Though both strategies are of the NTV family they suppress the neutral point (NP) voltage ripple differently. This work therefore aims to study the effects of these differences on the SynRM and the converter. Parameters of interest are the neutral point voltage, torque ripple, d-axis current ripple

(indication of the core losses) and the converter efficiency. However one disadvantage between the two modulation strategies is that, the switching frequency is not constant. Hence a modification of Mod-1 strategy is also proposed to attain a constant switching frequency.

A comprehensive study on the limitations of the voltage balancing algorithm depending on the loading conditions of the three level inverter was conducted by [19]. It was shown that a lower power factor require bigger capacitors to retain capacitor voltage balance. In the SynRM the power factor increases with the increase of the saliency ratio. The saliency ratio is the ratio between the direct (d) and quadrature (q) axis inductances and depending on the design it can be relatively low. This parameter depends on the geometry of the rotor and hence is a machine design issue.

There has been considerable research work aimed at increasing the saliency ratio of the SynRM in order to improve the performance of the SynRM. This means that the design of the SynRM machine has great influence on the size of the dc link capacitors since the power factor of the machine depends on the saliency ratio. One of the goals of this chapter is to also propose a relationship between the size of the SynRM and the size of the three level inverter dc link capacitors. The physical size of these capacitors is of integral importance since there is limited space in the electric vehicle. The capacitor would also contribute to the weight of the vehicle. In [22] a method to assist in the sizing of the dc link capacitors for various applications is outlined. However, this paper considers new parameters such as the machine saliency and the machine size.

This chapter therefore aims to accomplish a number of goals, firstly, a modulation scheme called Mod-1 which is able to archive a balance of the capacitor voltages with

a machine power factor below 0.5. Secondly, the comparison between Mod-1 strategy and the another modulation strategy called Mod-2. Thirdly, the sizing of the dc link capacitors. Fourth, the modif cation of mod-1 for a f xed switching frequency strategy and lastly the comparison with certain parameters when the SynRM is supplied by a two or three level inverter. Experimental work was conducted on a multiple SynRM.

2.2 Machine Model and Control

The use of vector control on a SynRM is a well known topic [23, 24]. A vector control policy was implemented on a SynRM for maintaining a constant speed. Fig. 2.2.1 shows the three level NPC inverter drive for a SynRM. The reference voltage vector for space vector pulse width modulation (SV-PWM) (v_d and v_q) were generated based on equations (2.2.1-2.2.4).

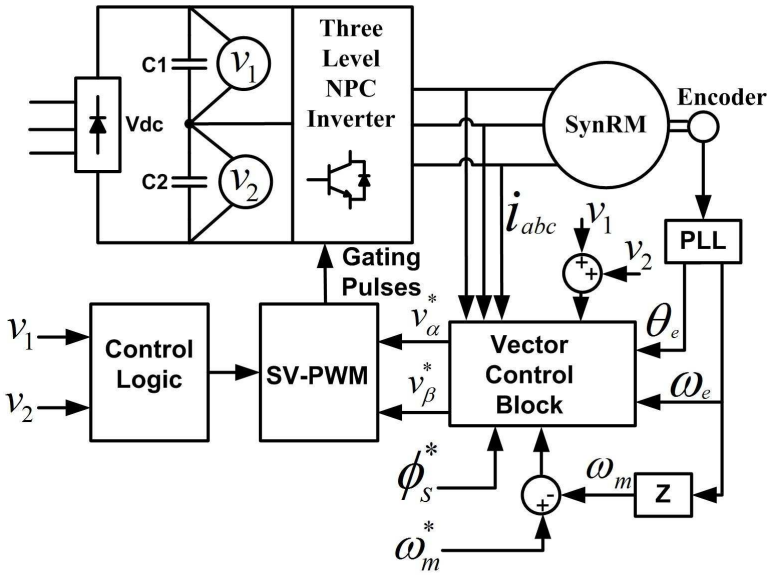

Figure 2.2.1: Three level NPC inverter SynRM electric drive

$$v_q = Ri_q + \frac{d\lambda_q}{dt} + \omega_e \lambda_d \tag{2.2.1}$$

$$v_d = Ri_d + \frac{d\lambda_d}{dt} - \omega_e \lambda_q \tag{2.2.2}$$

$$\lambda_d = L_d i_d \tag{2.2.3}$$

$$\lambda_q = L_q i_q \tag{2.2.4}$$

$$I_s = \sqrt{{i^2}_q + {i^2}_d} \tag{2.2.5}$$

$$T_e = \frac{3}{2} P(L_d - L_q) \frac{i_s^2 sin(2\theta_s)}{2} \tag{2.2.6}$$

$$Jp\omega_r = T_e - T_L - B\omega_m \tag{2.2.7}$$

v_d and v_q, i_d and i_q, L_d and L_q, λ_d and λ_q are the d, q axis voltages, stator currents and f ux linkages respectively. I_s, ω_e, R, ${\phi^*}_s$, ω_m and Z are the current vector, inverter frequency, stator resistance, reference current angle, mechanical speed, and the pole pairs number respectively.

Constant angle control was used for maintaining a certain d-q axis currents at a suitable load. The knowledge of this angle was acquired through a lock rotor test method. The shaft of the machine was locked at 9 different positions at approximately 10^0 resolution from 10^0 to 90^0 (electrical degrees) and the maximum dc current supplied was 16.2 A. A torque transducer was used to capture the generated torque at each rotor position, Fig. 2.2.2 shows the circuit model. From Fig. 2.2.2, I_a is equivalent to the magnitude of the current

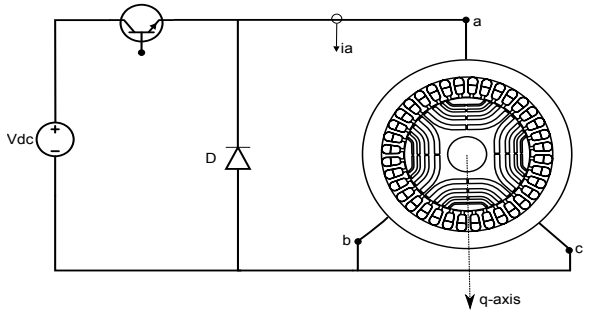

Figure 2.2.2: Experimental set up for torque measurements d-q axis inductances

vector I_s (2.2.5). Therefore since:

$$I_a = I_s$$

The reference d-q axis currents could be determined from (2.2.9)

$$\begin{aligned} i_q &= I_s * sin(\varphi_s) \\ i_d &= I_s * cos(\varphi_s) \end{aligned} \tag{2.2.8}$$

From Fig. 2.2.3, it can be seen that the best current angle was found within the range of 55^0-60^0 for maximum torque. The best angle was not constant due the magnetic cross coupling and saturation effects in the machine. For maximum torque at full load the current angle (θ_s^*) chosen for the experiments was 60^0.

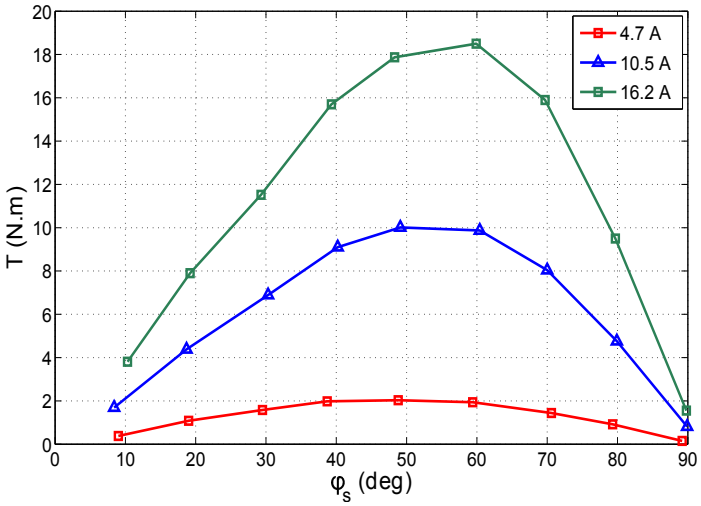

Figure 2.2.3: Torque angle prof le

2.3 Experimental Setup

A real time based operating system was used for the experimental studies. The inverter was operated at 10 kHz switching frequency. Fig. 2.3.1 shows the experimental set-up.

This work aims to accomplish a number of goals, the first, is the proposal of the modulation algorithm called Mod-1 which is able to archive capacitor voltage balancing on a machine with a low (below 0.5) power factor. Secondly, the comparison between Mod-1 strategy and the another modulation strategy called Mod-2. Thirdly, the comparison on certain parameters when the SynRM supplied by a two and three level inverter, fourthly the sizing of the dc link capacitors and lastly the modification of mod-1 for a fixed switching frequency strategy.

2.4 Three Level Inverter Operation

A prototype three level inverter was built in the lab see Fig. 2.4.1. The circuit model of the inverter is shown in Fig. 2.4.2. It has four switches per leg as compared to two switches in the two level inverter. Fig. 2.4.3 shows the voltage vector space, there are up to 27 voltage vectors of which 19 vectors are active and 8 are redundant vectors.

MV, SV, LV and ZV represent the medium, small, large and zero vectors respectively. Table 2.4.1 shows the physical representation of the switching states of Fig. 2.4.3. There are three different switching states as seen from the pole voltages, a positive (P), negative (N) and zero (0) voltages respectively. They are denoted as 1,0, and -1.

Table 2.4.1: Switching table on phase A

States	S_{A1}	S_{A2}	S_{A3}	S_{A4}	V_{ao}
P (Positive)	1	1	0	0	$\frac{1}{2}V_{dc}$
O (Zero)	0	1	1	0	0
N (Negative)	0	0	1	1	$-\frac{1}{2}V_{dc}$

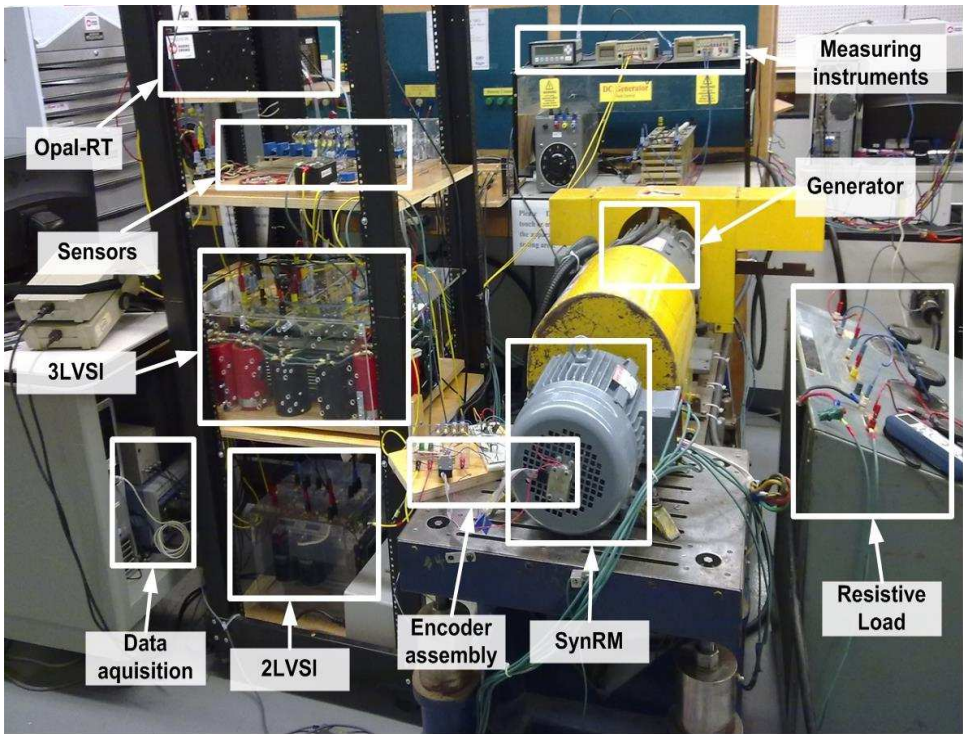

Figure 2.3.1: Experimental set-up

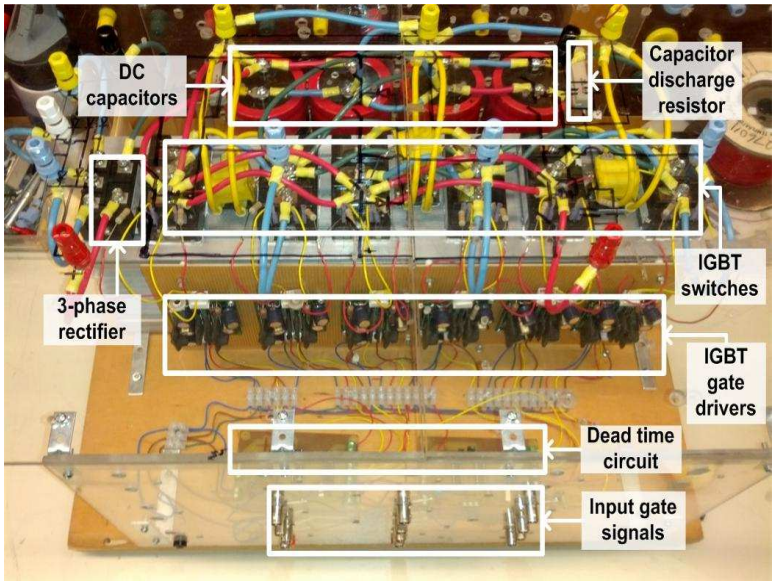

Figure 2.4.1: Prototype three level inverter

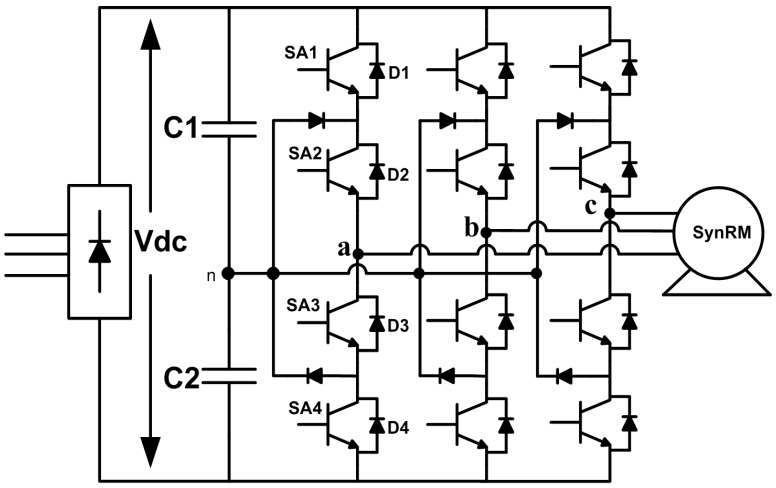

Figure 2.4.2: Three level inverter circuit model

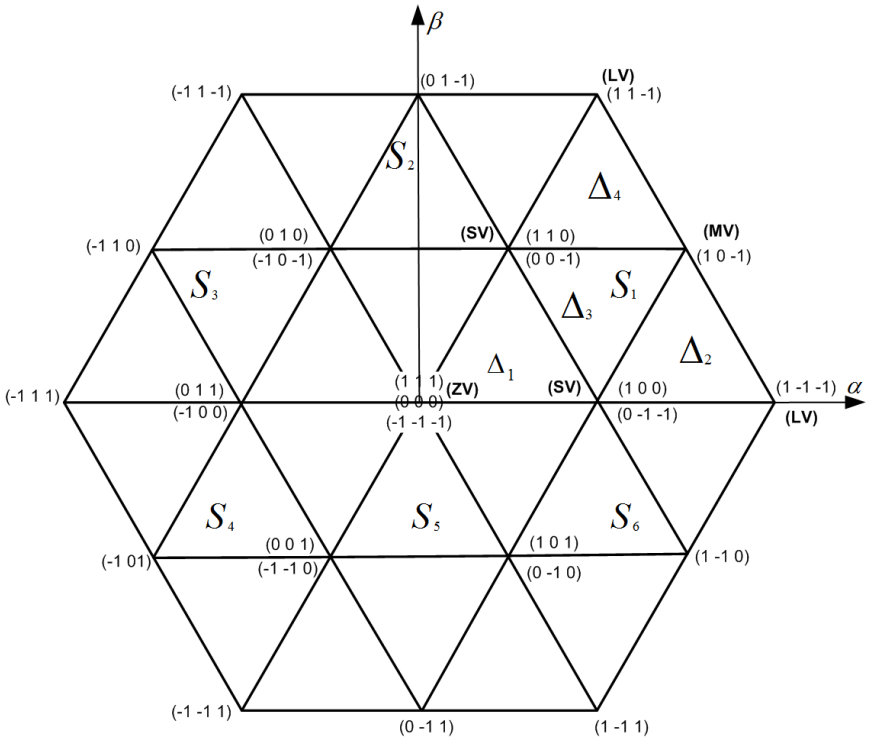

Figure 2.4.3: Three level space vector

2.4.1 Proposed Modulation Strategy

A new nearest three vector (NTV) modulation scheme is proposed in this work referred to as Mod-1. The large vectors (1-1-1,11-1,-11-1,-111,-1-11 and 1-11) and the zero vectors (000, 111 and -1-1-1) do not affect the voltage balance since no neutral current is drawn when they are active. The small vectors (100/0-1-1, 110/00-1, 010/-10-1, 011/-100, 001/-1-10 and 101/0-10) are the main reason for preserving the neutral point voltage balance. Careful utilization of the small vectors would result in a zero average neutral point current. However as the reference voltage moves outside the inner triangle the medium vectors would be activated.

The medium vectors (10-1, 01-1, -110, -101, 0-11 and 1-10) affect the neutral and contribute signif cantly to the imbalance depending on the nature of the load. There would be regions were the neutral point voltage ripple would not be able to be suppressed (capacitor voltage balance) [19]. The more the small triangles are utilized in the converter the better the neutral point voltage control. Take for example triangle 2 (Δ_2) and 4 (Δ_4), in those regions there is only one small vector that can be utilized hence it will be more diff cult to constrain the neutral point voltage. In triangle 1 there are two small vectors hence in this region the neutral point voltage can be suppressed. The neutral point voltage ripple develops due to the imbalance between the capacitor voltages.

The primary challenge of the three level inverter is the balancing of the two dc link capacitors. These capacitors are necessary for creating a neutral point to attain the zero pole voltage state. Mod-1 strategy is developed to choose the three voltage state vectors with the goal of maintaining a balance between the capacitor voltages. Table 2.4.2 shows

only sector I of the balancing algorithm used, the steps are the number of the switching states in a switching sequence. Table 2.4.3 shows the computation of the respective dwell times of the voltage vector states.

Table 2.4.2: Mod-1 switching table on phase A

NP Voltage	Triangle	Sequences	Steps
$V_{c1} > V_{c2}$	1	000,100,110 // 110-100-000	2
$V_{c1} < V_{c2}$	1	-1-1-1,0-1-1,00-1 // 00-1,0-1-1,-1-1-1	2
$V_{c1} > V_{c2}$	2	100,1-1-1,10-1 // 10-1,1-1-1,100	3
$V_{c1} < V_{c2}$	2	0-1-1,1-1-1,10-1 // 10-1,1-1-1,0-1-1	2
$V_{c1} > V_{c2}$	3	110,100,10-1 // 10-1,100,110	2
$V_{c1} < V_{c2}$	3	00-1,0-1-1,10-1 // 10-1,0-1-1,00-1	3
$V_{c1} > V_{c2}$	4	110,10-1,11-1 // 00-1,10-1,110	3
$V_{c1} < V_{c2}$	4	00-1,10-1,11-1 // 11-1,10-1,00-1	3

Figs. 2.4.4 and 2.4.5 is an illustration of table 2.4.2. As can be seen from these f gures by choosing vector ”100” there would be a negative NP current which would discharge the upper capacitor (C_1) whereas ”0-1-1” would result in a positive NP current and hence discharge the lower capacitor (C_2). Both of these vectors (100/0-1-1) generate the same output voltage however with different NP current directions.

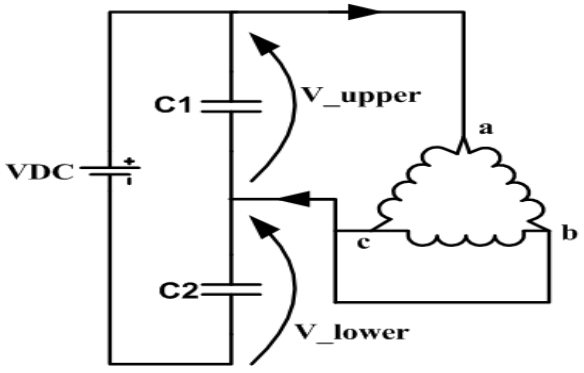

Figure 2.4.4: Discharging the upper capacitor using small a vector (100)

Table 2.4.3: Switching table on phase A

Triangles	Vectors	Dwell times
1	000,-1-1-1,111	$t_0 = T\left[1 - 2ksin(\gamma + \pi/3)\right]$
	100,0-1-1	$t_1 = 2kTsin(\pi/3 - \gamma)$
	110,00-1	$t_2 = 2kTsin(\gamma)$
2	100,0-1-1	$t_1 = 2T\left[1 - ksin(\gamma + \pi/3)\right]$
	10-1	$t_3 = 2kTsin(\gamma)$
	1-1-1,	$t_4 = T\left[2ksin(\pi/3 - \gamma) - 1\right]$
3	100,0-1-1	$t_1 = T\left[1 - 2ksin(\gamma)\right]$
	110,00-1	$t_2 = T\left[1 - 2ksin(\pi/3 - \gamma)\right]$
	10-1	$t_3 = T\left[2ksin(\pi/3 + \gamma) - 1\right]$
4	110,00-1	$t_2 = 2T\left[1 - ksin(\gamma + \pi/3)\right]$
	10-1	$t_3 = 2kTsin(\pi/3 - \gamma)$
	11-1	$t_4 = T\left[2ksin(\gamma) - 1\right]$

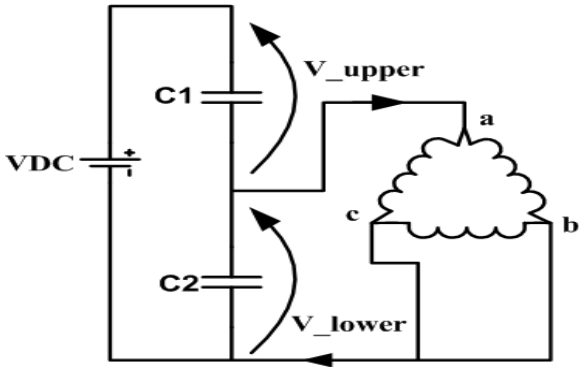

Figure 2.4.5: Discharging the lower capacitor using a small vector (0-1-1)

Equation (2.4.1) and (2.4.2) shows the computation of the reference vector.

$$V_{ref} = d_s V_s + d_M V_M + d_L V_L \quad (2.4.1)$$

$$d_s + d_M + d_L = 1 \quad (2.4.2)$$

d_S, d_M and d_L is the duty cycle of the small, medium and large switching state vectors respectively.

In [25], it was noted that there are two forms of voltage imbalance during the converter operation, f rstly, as a voltage deviation (typically during transients) and secondly, as a low frequency voltage oscillation (neutral point voltage ripple) during the converter steady state operation. Equation (2.4.3) describes the NP voltage as:

$$v_{NP} = V_{C1} - V_{DC}/2 \quad (2.4.3)$$

For steady state conditions the low frequency NP voltage ripple will also cause the output line to line voltages to contain low frequency harmonics [26]. This also means that the devices and the capacitors must withstand higher voltages than when balancing between the capacitor voltages is achieved. Hence the dc link capacitors must be sized for the attenuation of this NP voltage ripple.

The v_{NP} is a function of load power angle (power factor), modulation index, maximum output converter current, dc-link capacitor and the fundamental frequency of the converter [22]. Using the work done by [22] as a baseline, a method for assisting in the sizing of the dc-link capacitor for any SynRM can be developed. SynRMs with high saliency ratios have better power factors (above 0.7), there is a relationship between the saliency ratio and the machine's power factor. This in effect makes it possible for the characterization of the low frequency NP voltage ripple in terms of the machine saliency.

2.5 DC-link Capacitor Sizing Based on Mod-1 Strategy

The NP voltage was normalized by the use of equation (2.5.1) [22].

$$\frac{\Delta V_{NPn}(\varphi, m_i)}{2} = \frac{\frac{\Delta V_{NP}}{2}}{\frac{I_o}{fC}} \tag{2.5.1}$$

V_{NPn}, m_i, I_o, f, C and φ is the normalized NP voltage, modulation index, RMS output inverter current, fundamental inverter frequency, the dc-link capacitor and the power factor angle respectively.

As is clear from equation (2.5.1) the normalized voltage ripple depends on the load power angle. The SynRM is a non-linear load, the inductance of the machine is a function of the current and the magnetic f ux. The magnetic f ux in turn is a function of the magnetic material and design of the machine. Through the use of a simplif ed SynRM phasor diagram shown in Fig. 2.5.1, the saliency of the machine can be related to the power factor. This phasor diagram does not take into account the iron losses.

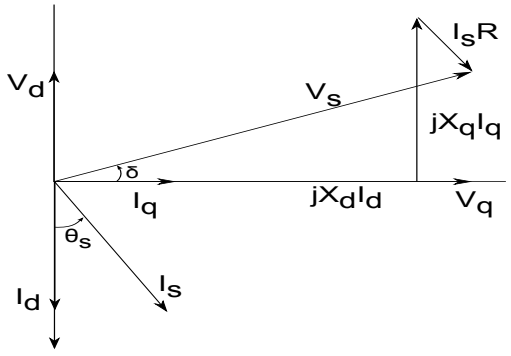

Figure 2.5.1: Simplif ed phasor diagram of SynRM

The derivation of power factor or load power angle as a function of the machine is articulated through equation (2.5.2)-(2.5.5) [27].

$$cos(\varphi) = \frac{V_q sin(\theta_s) + V_d cos(\theta_s)}{\sqrt{{V^2}_q + {V^2}_d}} \tag{2.5.2}$$

$$cos(\varphi) = \frac{\omega L_d I_d sin(\theta_s) - \omega L_q I_q cos(\theta_s)}{\sqrt{\omega L_d {I_d}^2 + \omega L_q {I_q}^2}} \tag{2.5.3}$$

$$cos(\varphi) = \frac{(L_d - L_q) cos(\theta_s) sin(\theta_s)}{\sqrt{L_d cos(\theta_s)^2 + L_q sin(\theta_s)^2}} \tag{2.5.4}$$

$$cos(\varphi) = \frac{k-1}{\sqrt{k^2 \frac{1}{sin^2(\theta_s)} + \frac{1}{cos^2(\theta_s)}}} \tag{2.5.5}$$

For maximum power factor condition:

$$cos(\varphi)_{max} = \frac{k-1}{k+1} \tag{2.5.6}$$

k (L_d/L_q), φ and θ_s is the saliency of the SynRM machine, load power angle and the current phasor angle (MMF angle).

Though the resistance of the machine is ignored in the derivation of equation (2.5.5), the resistance of the machine contributes to an increase in power factor. Therefore equation (2.5.5) gives the minimum power factor, what would be regarded as the worst case. This is good enough to provide a general relationship between the saliency and machine power factor. As can be seen from equation (2.5.5), the power factor is not only a function of the saliency but also of the current phasor angle (θ_s).

The SynRM is generally designed for a certain operating point and the maximum power factor operating point is an ideal operating condition to def ne the rated torque of the machine. Hence to further simplify equation (2.5.5), an equation describing a relationship between maximum power factor and saliency was used instead, see equation (2.5.6), detailed derivations can be found in [27]. Fig. 2.5.2 shows the relationship between maximum power factor and saliency ratio of the SynRM. This relationship was drawn from equation (2.5.6) and is a reproduction of [27].

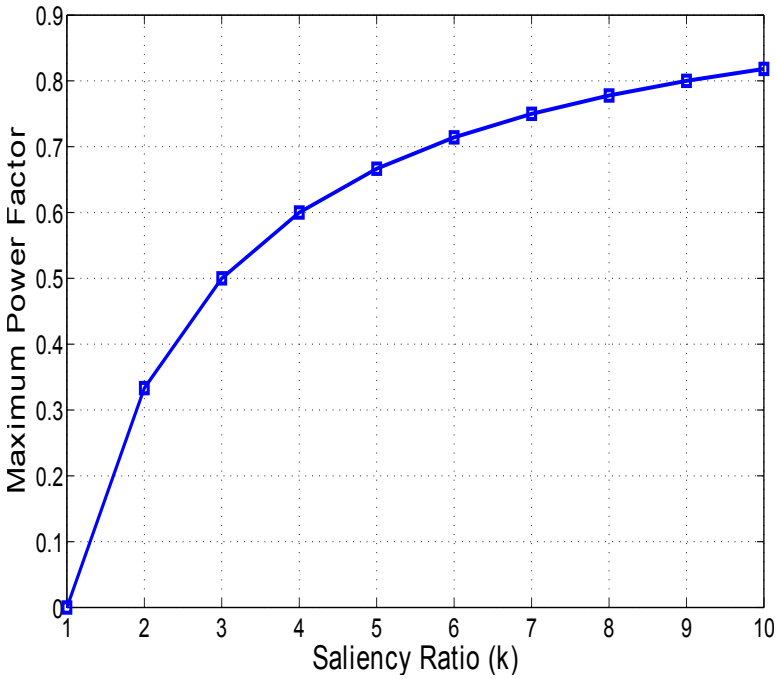

Figure 2.5.2: Maximum power factor V.s SynRM saliency ratio

The machine saliency ratio chosen in this work ranges from 1 to 10. This work considers the predominantly used axially laminated SynRM as opposed to radially laminated machine since they are easier to manufacture and more robust. This point is highlighted since radially laminated SynRM generally have higher saliency ratios. Axially laminated SynRM suffers from lower saliency ratios.

From Figs. 2.5.2 and 2.5.3, it is clear that with low modulation indexes the saliency of the machine does not affect the neutral point voltage. However with higher modulation indexes the saliency ratio of the machine becomes a signif cant factor in affecting the neutral point voltage.

Equation (2.5.7) to (2.5.10) describes the derivation of the sizing of the capacitors of a three level inverter SynRM drive using the machine size as one of the parameters. Equation (2.5.10) shows that poor eff ciency of the machine will contribute toward the increase

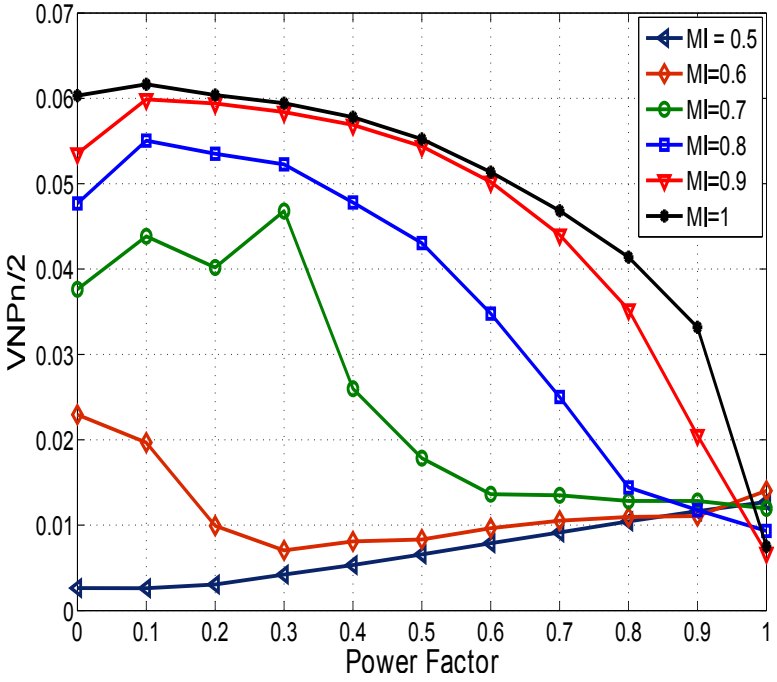

Figure 2.5.3: Normalized neutral point voltage vs power factor and modulation index

of the capacitor voltage ripple. This is because to obtain the same output voltage the input current of the machine will be much higher as compared to a higher eff ciency machine.

$$P_{in} = \sqrt{3}V_o I_o cos(\varphi) \tag{2.5.7}$$

$$I_o = \frac{P_o}{\sqrt{3}V_o cos(\varphi)} \tag{2.5.8}$$

By substituting equation (2.5.8) into (2.5.1) the following expressing can be deduced.

$$\frac{\Delta V_{NP}}{2} = \frac{\Delta V_{NPn}(\varphi, m_i)}{2} \frac{P_o}{\sqrt{3}V_o cos(\varphi)} \frac{1}{fC} \tag{2.5.9}$$

$$\frac{\Delta V_{NP}}{2} = \frac{\Delta V_{NPn}(\varphi, m_i)}{2} \frac{P_{out}}{U\sqrt{3}V_o cos(\varphi)} \frac{1}{fC} \tag{2.5.10}$$

V_o, P_o and U is the inverter output rms voltage, power output and the machine eff ciency respectively.

The machine was run at a constant speed of 900 rpm. Table 2.5.1 shows the SynRM operating point parameters. The machine had a poor power factor due to a poor saliency ratio and this is in agreement with Fig. 2.5.2. Given these operating points, the theoretical value of the ripple voltage was compared with the actual experimental data by the use of equation (2.5.9). By the use of Fig. 2.5.3 the normalized neutral point voltage ripple was

Table 2.5.1: SynRM running condition

Line voltage V_{L-L}	130 V
Input power	1.518 kW
Power factor	0.4
saliency ratio	2.2
Speed (rpm/Hz)	900 $rpm/30\ Hz$
Torque	12 $N.m$
Modulation index	0.8
Dc link capacitance C	4090 μF

found to be 0.055. The theoretical V_{NP} was calculated as:

$$\begin{aligned} \frac{\Delta V_{NP}}{2} &= \frac{\Delta V_{NPn}(\varphi, m_i)}{2} \frac{P_o}{\sqrt{3} V_o cos(\varphi)} \frac{1}{fC} \\ &= 0.055 \times \frac{1476}{\sqrt{3} \times 130 \times 0.4} \frac{1}{30 \times 4.09 \times 10^{-3}} \\ &= 7.3\ V \end{aligned} \tag{2.5.11}$$

The experimental voltage ripple was found to be 8.9 V. These results show that the proposed method is good enough to be used as a sizing method for the three level inverter dc link capacitors. Equation (2.5.9) makes use of the input parameters of the machine such as the input voltage and the input power (output power of the inverter). These parameters can generally be obtained at the industrial site. Through the use of Fig. 2.5.2, Fig. 2.5.3 and equation (2.5.6) the neutral point voltage was represented as function of the saliency

ratio and the modulation index ($\frac{\Delta V_{NPn}(k,m_i)}{2}$). Hence a relationship between the normalized neutral point voltage and the saliency ratio of the machine was developed as shown in Fig. 2.5.4. By using the desired neutral point voltage ripple, modulation index, saliency

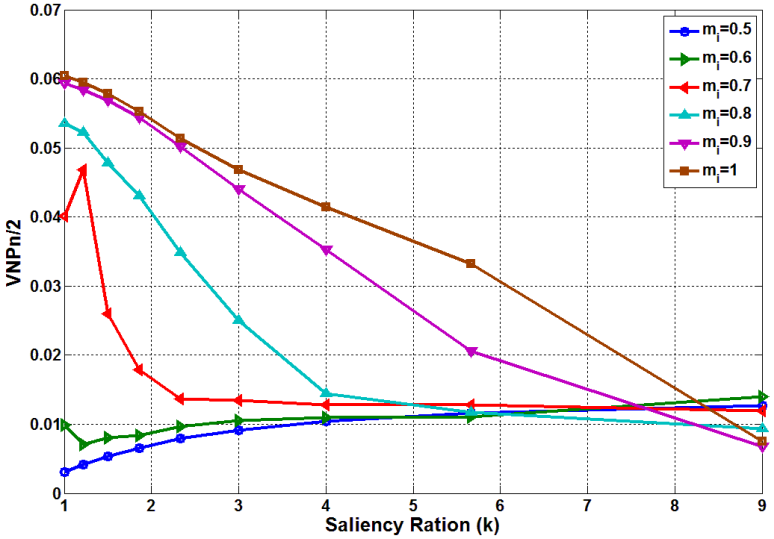

Figure 2.5.4: Neutral point voltage ripple as a function of the machine saliency ratio and modulation index

ratio, fundamental operating frequency and different machine input currents, a relationship between the machine input current and the capacitor size can be presented. However since knowledge of the power factor is by the use of equation (2.5.6), the machine input power can be computed through the use of equation (2.5.7).

Since the case studies were based on steady state operation of the machine a modulation index of 0.9 is used and the fundamental frequency used is 60 Hz, with saliency ratio ranging from 4 to 7. Fig. 2.5.5 to 2.5.8 show the dc link capacitor size as a function of the machine size (input power) and machine saliency ratio at different neutral point ripple voltages. From Fig. 2.5.5 to Fig. 2.5.6 the machine is operated at a dc voltage of 400 V, while in Fig. 2.5.7 to Fig. 2.5.8 the dc bus voltage is 600 V.

Fig. 2.5.5 (a) and 2.5.5 (b) shows that as the saliency ratio increases the required capacitor size drops which is in agreement with Fig. 2.5.4. The curves are shown at different neutral point ripple voltages, from 2% to 10% of the dc bus voltage with high capacitance required for lower a neutral point voltage ripple. From the curves it is clear that the capacitor size increased with the input power of the machine. Fig. 5 (a) to 8 (b) show that as the dc bus voltage increased the required capacitance droped. The saliency ratio of the machine contributes towards the reduction of the capacitor size.

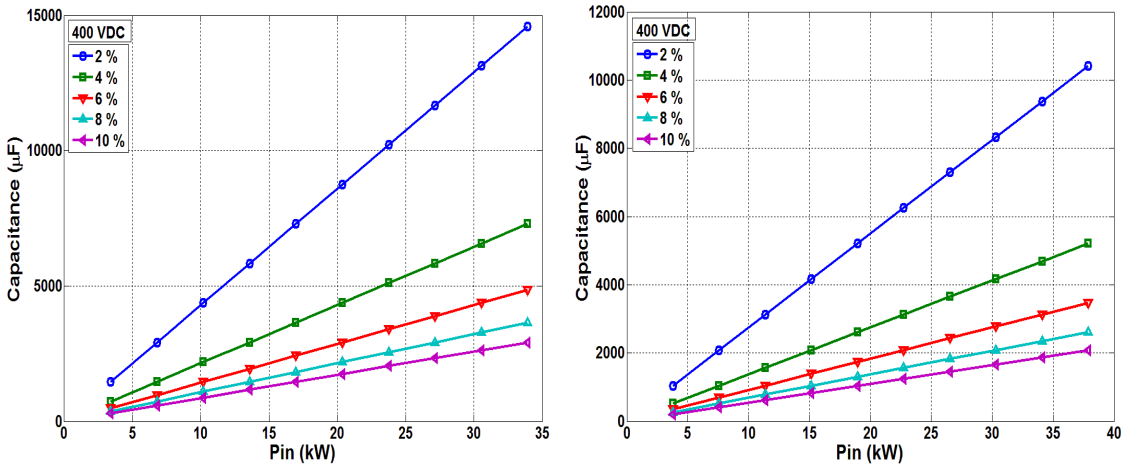

Figure 2.5.5: Dc link capacitance sizes at different machine input power at a saliency ratio of 4 (a) and 5 (b)

2.6 Comparison of Two Modulation Strategies

Another modulation strategy called Mod-2 was compared with the developed Mod-1 strategy. Mod-2 strategy balances the capacitor voltages based on the variation of the dwell time of the vector states. This means a vector state will be given more dwell time in support of suppressing the NP voltage ripple. Table 2.6.1 shows the vector states for each triangle for Mod-2 strategy and associated dwell times. Equation (2.6.1) and (2.6.2) describes the

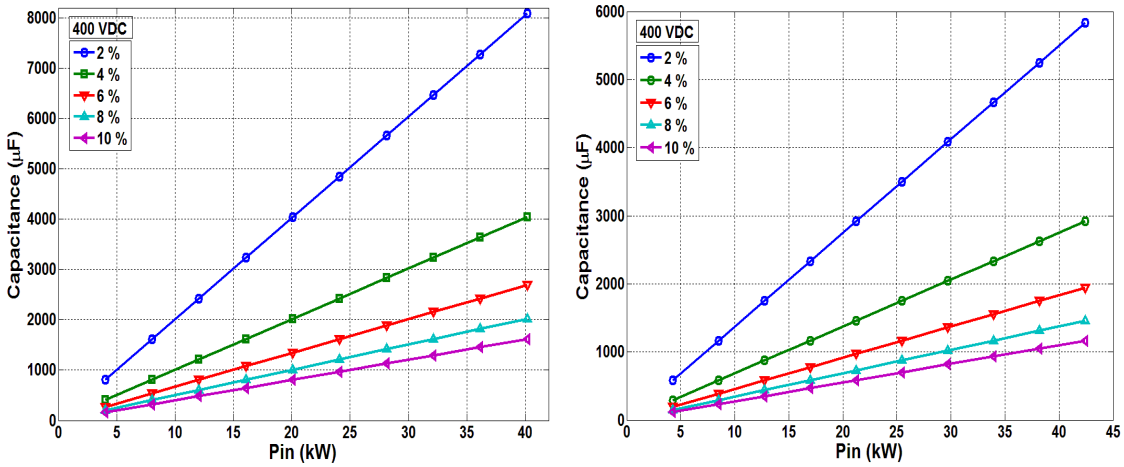

Figure 2.5.6: Dc link capacitance sizes at different machine input power at a saliency ratio of 6 (a) and 7 (b)

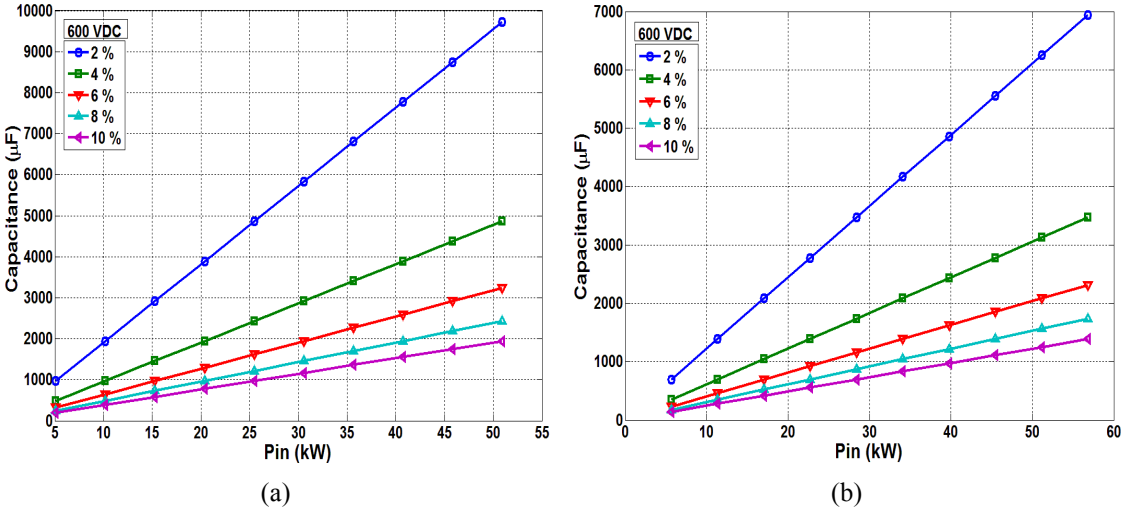

Figure 2.5.7: Dc link capacitance sizes at different machine input power at a saliency ratio of 4 (a) and 5 (b)

Table 2.6.1: Switching table for Mod-2

NP Voltage	Triangle	Sequences	Steps
T_{sv1} & T_{sv2}	1	-1-1-1,0-1-1,00-1,000,100,110	5
T_{sv1}	2	0-1-1,1-1-1,10-1,100	3
T_{sv1} & T_{sv2}	3	0-1-1,00-1,10-1,100,110	4
T_{sv2}	4	00-1,10-1,11-1,110	3

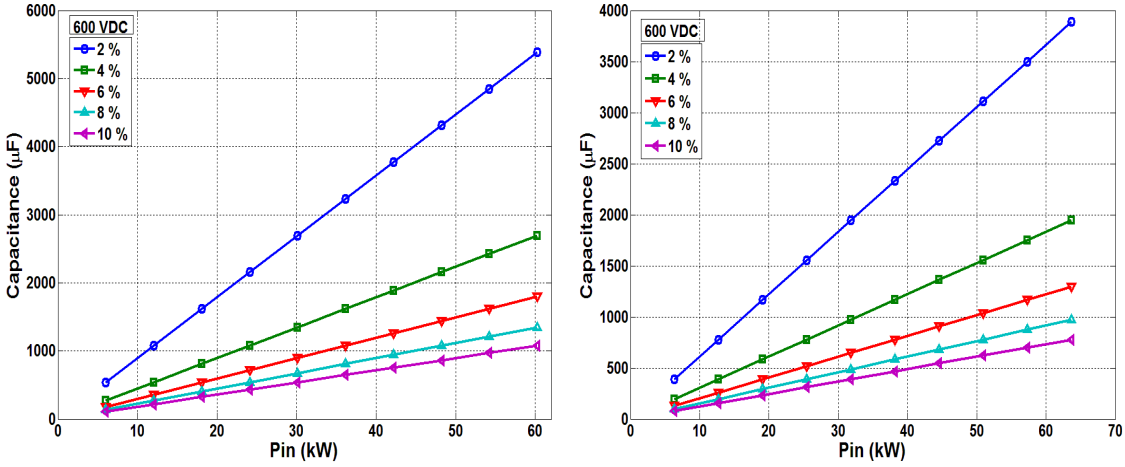

Figure 2.5.8: Dc link capacitance sizes at different machine input power at a saliency ratio of 6 (a) and 7 (b)

dwell times for Mod-2 strategy:

$$T_{(0-1-1)} = T_{sv1}\frac{1-x}{2} \;\&\; T_{(100)} = T_{sv1}\frac{1+x}{2} \tag{2.6.1}$$

$$T_{(00-1)} = T_{sv2}\frac{1-x}{2} \;\&\; T_{(110)} = T_{sv2}\frac{1+x}{2} \tag{2.6.2}$$

$T_{sv1} \in [T_{(0-1-1)}, T_{(100)}]$ and $T_{sv2} \in [T_{(00-1)}, T_{(110)}]$ represent the dwell times for the voltage vector states in triangle 1. Since the dwell times must be positive the interval for x is $x \in [-1, 1]$.

The parameter x was incremented in steps of 0.5. To illustrate the Mod-2 balancing strategy, suppose the reference voltage vector is in triangle 1 and $V_{c1} > V_{c2}$. Parameter x will be increased resulting in the following dwell times $T_{(100)} > T_{(0-1-1)}$.

This can also be illustrated in Figs. 2.4.4 and 2.4.5. Having $T_{(100)} > T_{(0-1-1)}$ means that the discharge process of $c1$ as shown in Fig. 2.4.4 will have a larger discharge duration than that of $c2$ as shown in Fig. 2.4.5. Conversely, if $V_{c2} > V_{c1}$, x will become more negative resulting in $T_{(0-1-1)} > T_{(100)}$. In this way $c2$ will experience a larger discharge

current duration than $c1$.

2.6.1 Experimental Results

Fig. 2.6.1 to Fig. 2.6.4 show the performance of a synchronous reluctance machine under Mod-1 and Mod-2 strategies.

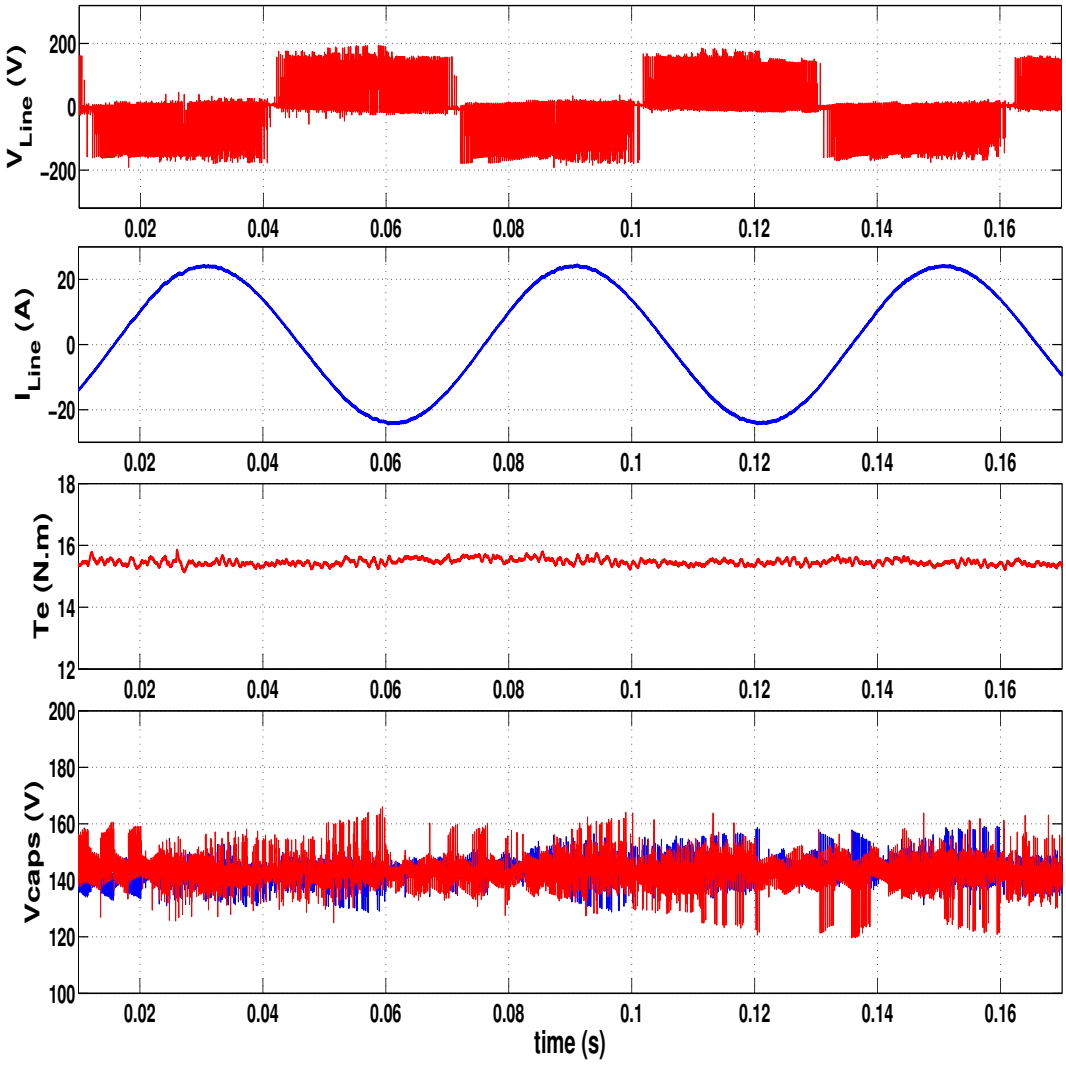

Figure 2.6.1: Mod-1 strategy @ $m_i = 0.4$, @ approximately 500 rpm, from top to bottom, (i) line voltage, (ii) line current, (iii) torque and (iv) capacitor voltages

Tables 2.6.2 and 2.6.3 show that the Mod-2 inverter produced lower torque ripple and THD as compared to the Mod-2 strategy at low modulation index, $m_i = 0.4$ and higher

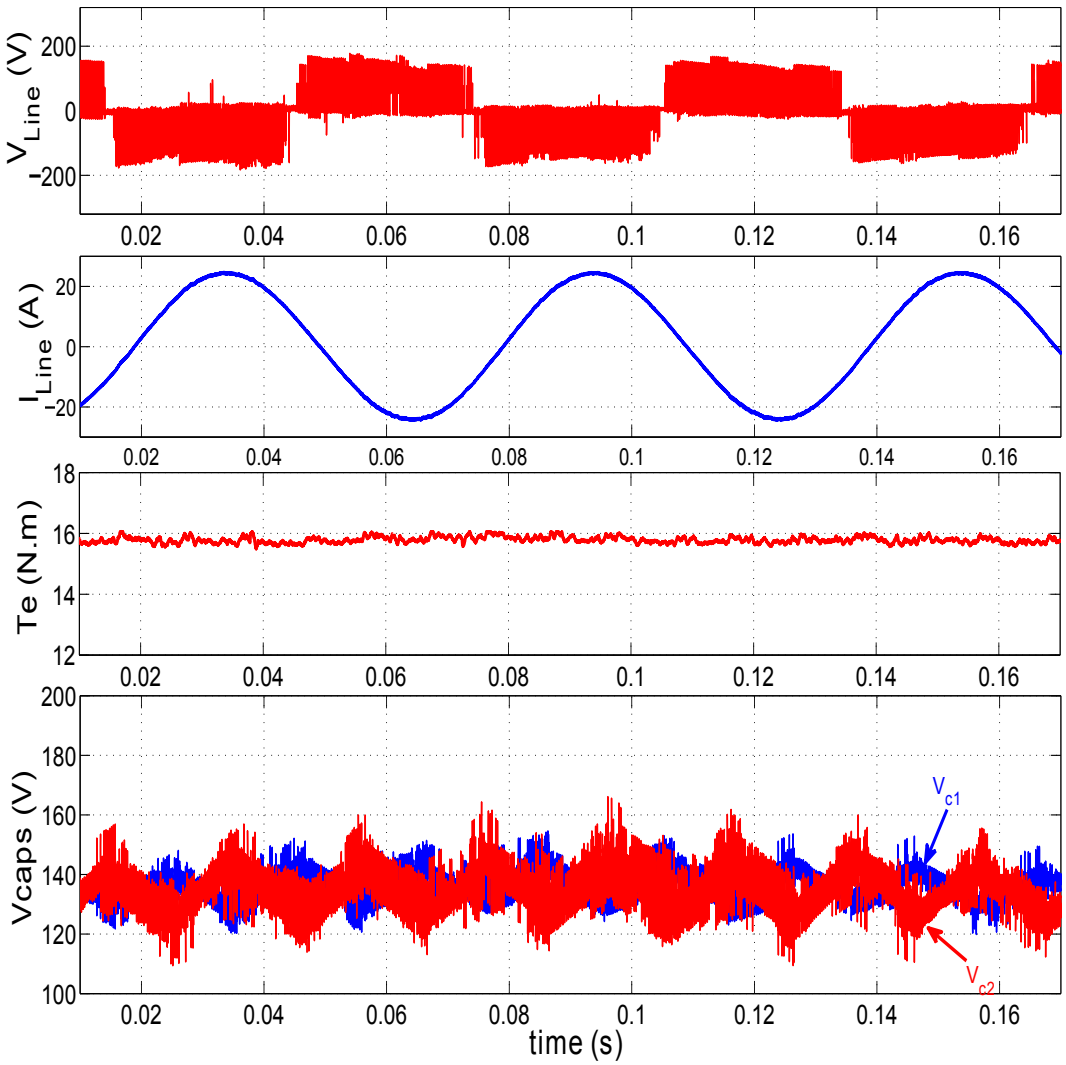

Figure 2.6.2: Mod-2 strategy @ $m_i = 0.4$, @ approximately 500 rpm, from top to bottom, (i) line voltage, (ii) line current, (iii) torque and (iv) capacitor voltages

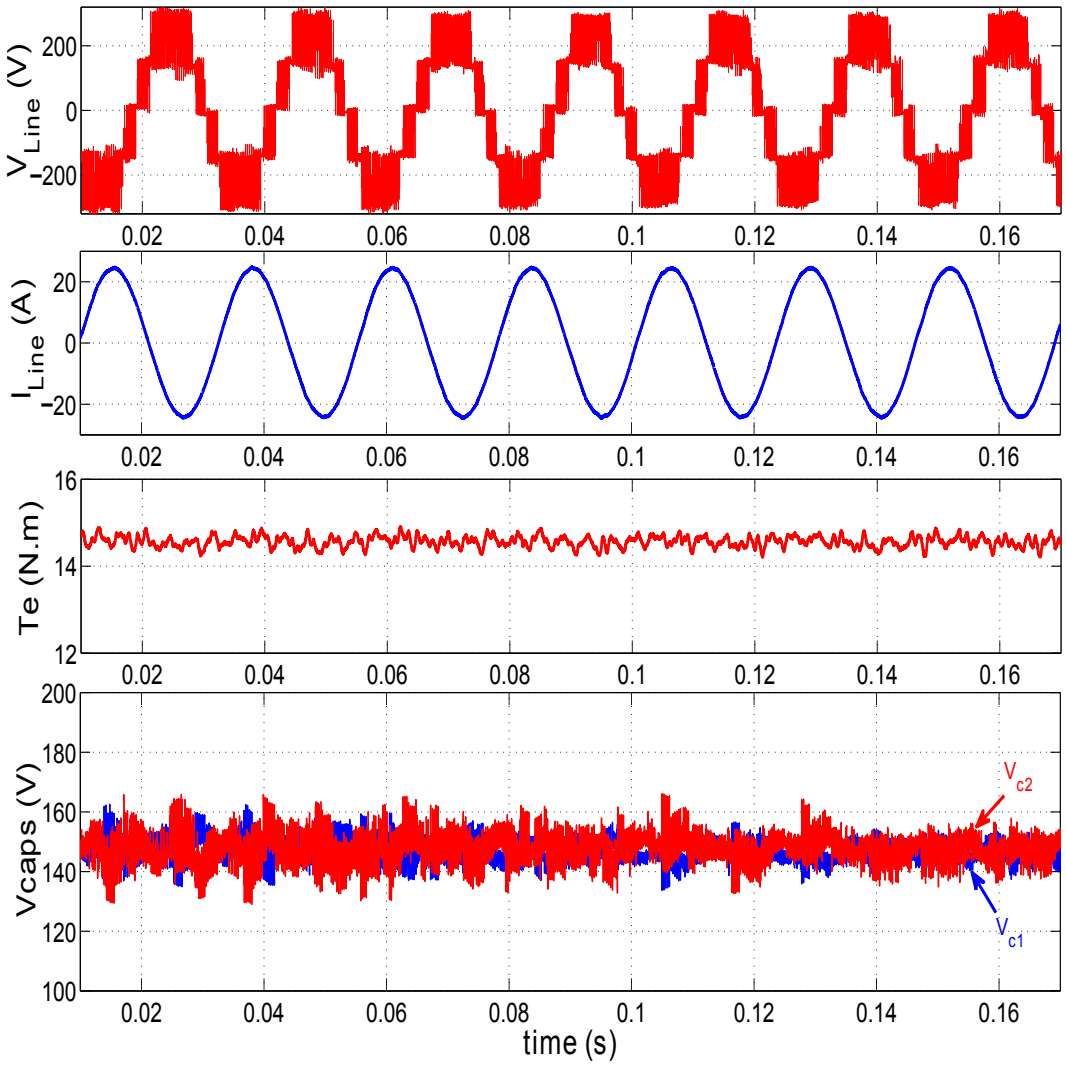

Figure 2.6.3: Mod-1 strategy @ $m_i = 0.95$, @ approximately 1320 rpm, from top to bottom, (i) line voltage, (ii) line current, (iii) torque and (iv) capacitor voltages

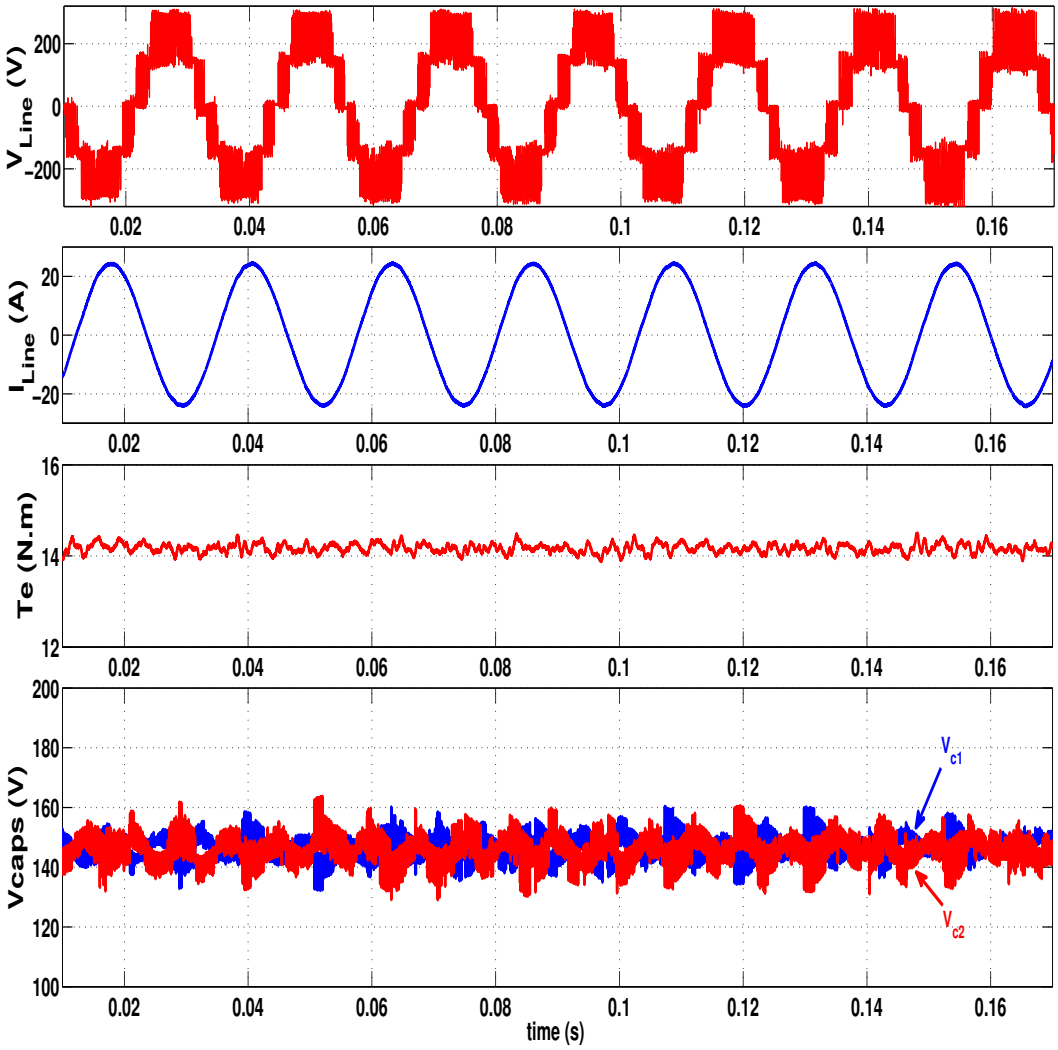

Figure 2.6.4: Mod-2 strategy @ $m_i = 0.95$, @ approximately 1320 rpm, from top to bottom, (i) line voltage, (ii) line current, (iii) torque and (iv) capacitor voltages

modulation index $m_i = 0.95$. Mod-1 registered a higher dc current ripple at lower modulation index. However, at higher modulation index Mod-1 had a relatively lower dc current ripple. At lower modulation index Mod-2 had 11% more NP voltage ripple when compared to Mod-1 strategy. At higher modulation index the NP voltage ripples were approximately the same. Table 2.6.2 also shows that the eff ciency of Mod-1 was 18% higher.

Table 2.6.2: Comparison between Mod-1 and Mod-2 inverter @ an average $m_i = 0.4$

Parameters	Mod-1 Inverter	Mod-2 Inverter
THD_i (%)	1.7	1.35
$Idc_{average}$ (A)	5.12	6.66
Idc_{ripple} (%)	65.42	58.47
VNP_{ripple} (%)	12.83	14.51
$Torque_{ripple}$ (%)	4.54	3.52
Eff ciency($< 50^0C$) (%)	76.33	62.23

For EV/HEV applications Mod-1 would be preferred due to the limited energy source depending on the drive cycle. Whereas at a modulation index of 0.95, the eff ciencies were relatively the same. This is because the Mod-2 strategy has more switching steps at a lower modulation index (mi=0.4). At a modulation index of 0.4 the reference voltage phasor is only in triangle 1, and as is shown in table 2.6.1, Mod-2 strategy has a maximum of 5 switching steps as compared to only 3 switching steps in the Mod-1 strategy as shown in table 2.4.2. Table 2.6.3 shows that the d-axis current ripple at higher modulation index was approximatly the same for Mod-1 and Mod-2 strategies. This implies that the two strategies would produce similar core losses.

One of the disadvantages of the Mod-2 strategy is that it has a higher number of switching steps than Mod-1 strategy, hence higher inverter losses that were observed at a lower

Table 2.6.3: Comparison between Mod-1 and Mod-2 inverter @ an average $m_i = 0.95$

Parameters	Mod-1 Inverter	Mod-2 Inverter
THD_i (%)	1.77	1.13
$Id_{average}$ (A)	6.58	6.36
Id_{ripple} (%)	5.33	5.28
$Idc_{average}$ (A)	8.88	8.74
Idc_{ripple} (%)	36.09	38.30
VNP_{ripple} (%)	10.72	10.60
$Torque_{ripple}$ (%)	5.14	4.39
Eff ciency($< 50^0C$) (%)	93.57	94.98

modulation index. The other observation is that Mod-2 had higher capacitor voltage ripple at a lower modulation index. Mod-1 is well suited in suppressing the NP voltage ripple as compared to Mod-2 even though the Mod-2 strategy produced lower torque ripples and better power quality. Mod-1 strategy was more satisfactory throughout the operation of the SynRM, from the transient stage to the steady state operation in spite of a maximum power factor of 0.45 of the SynRM. However due to the variation in the number of the switching steps Mod-1 and Mod-2 strategies do not have a f xed switching frequency.

2.6.2 Proposed Mod-1 Strategy Dynamic Tests

A speed and load torque change were imposed on the machine to test the robustness of the proposed modulation scheme. Figs. 2.6.5 and 2.6.6 shows the response of the proposed modulation scheme during a speed change (200 rpm to 800 rpm) and a load torque change (3 N.m to 12 N.m) respectively.

The proposed modulation scheme showed satisfactory performance during both the speed and torque commands. There was a slight increase in the capacitor voltage ripple.

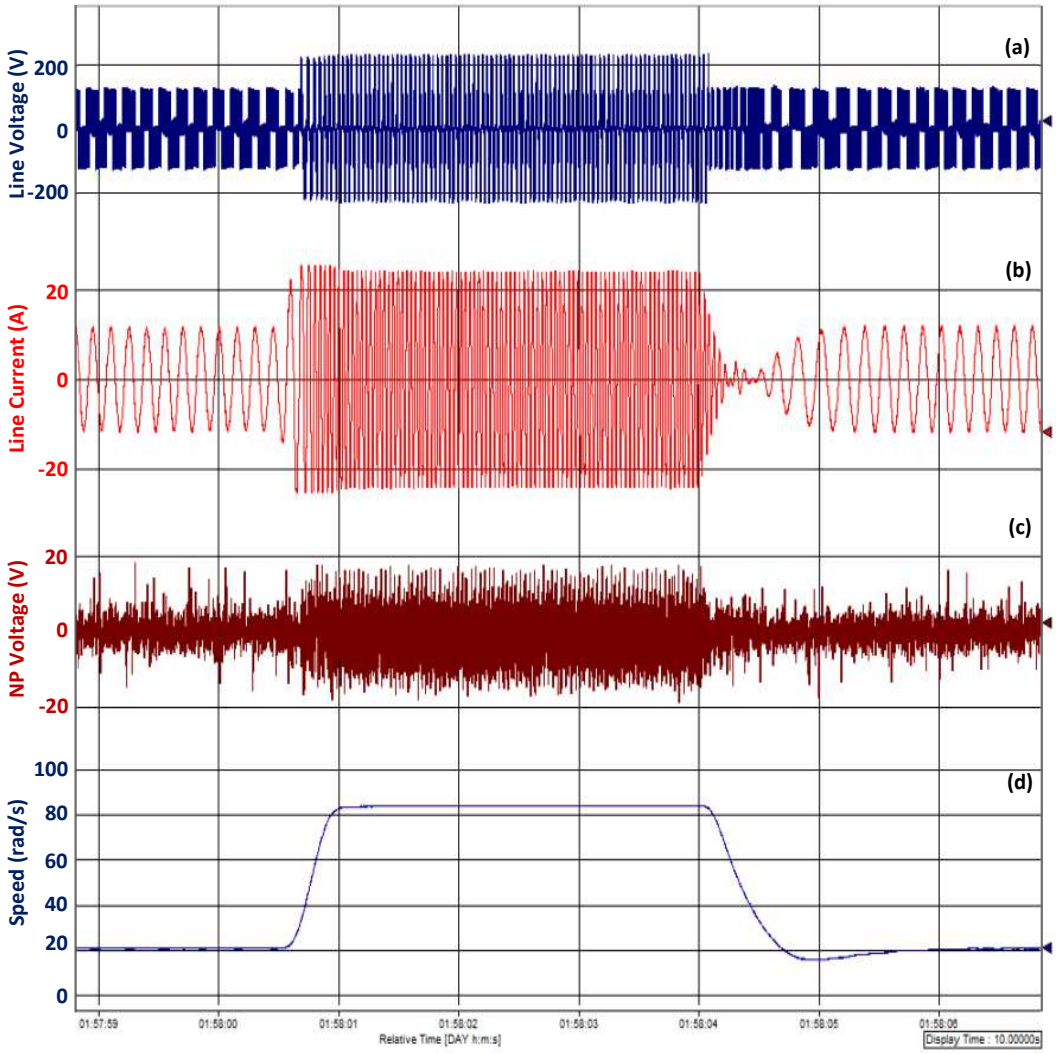

Figure 2.6.5: Performance of the proposed modulation scheme (a) Line voltage, (b) Line current, (c) Neutral point voltage ripple and (d) Speed change from 20.9 rad/s (200 rpm) to 83.7 rad/s (800 rpm)

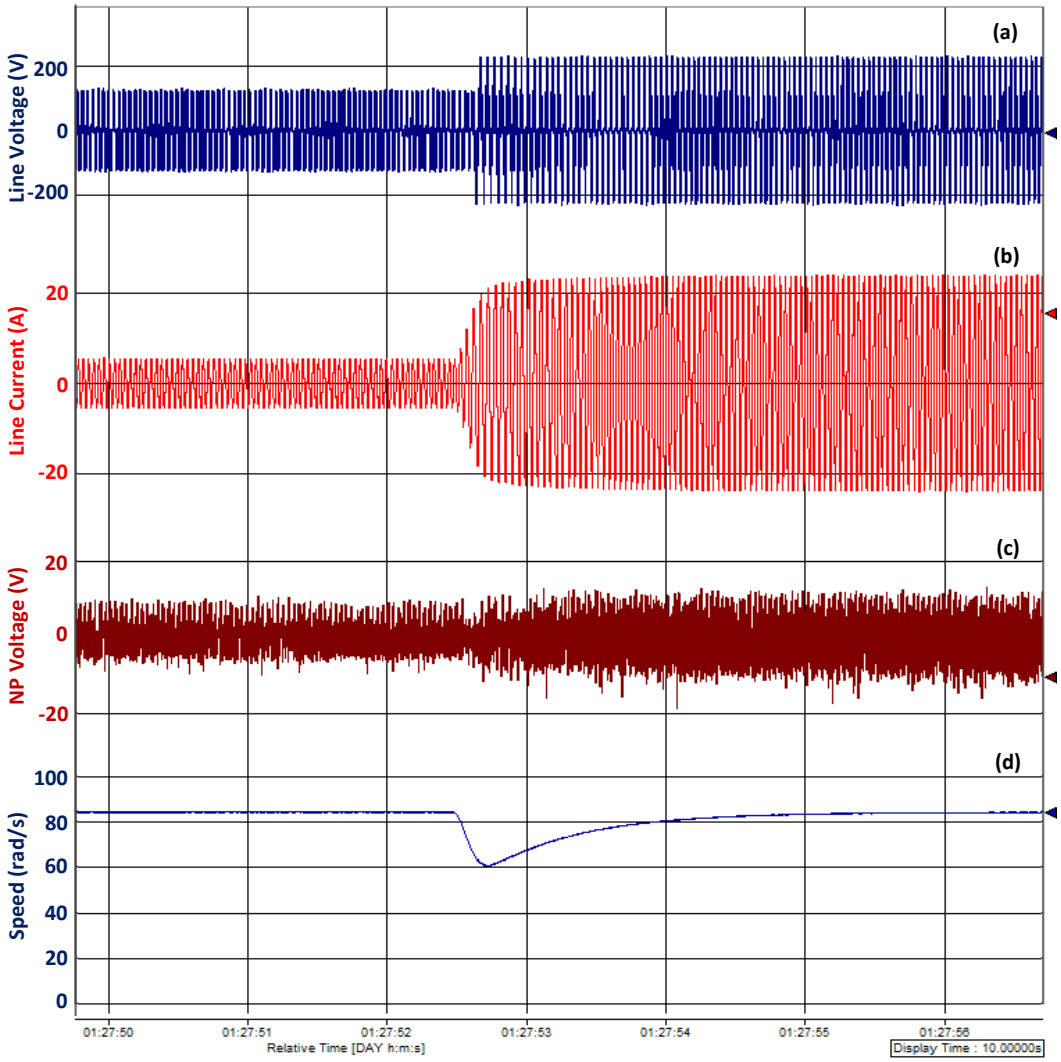

Figure 2.6.6: Performance of the proposed modulation scheme during a load change from 3 N.m to 12 N.m (a) Line voltage, (b) Line current, (c) Neutral point voltage ripple and (d) machine speed

This was expected since at the new speed and torque values the modulation index increased to where small vectors had lower dwell times. The increase in the modulation index can be observed in Fig. 2.6.5 (a) and 2.6.6 (a), there is an additional voltage level after the new speed and torque commands.

2.7 Two and Three Level Inverter SynRM Drive Comparison

A two and three level inverter were compared. The three level inverter used Mod-1 strategy since Mod-1 strategy had better eff ciency for both a lower and higher modulation index. A parameter of interest was the d-axis current ripple. This parameter serves as a good indicator of the iron losses in the machine. This is because the air gap f ux of the machine is mainly dominated by the d-axis f ux component ($\lambda_d = L_d i_d$).

2.7.1 Simulation Studies

Fig. 2.7.1 to 2.7.2 show the simulation results of the performance of the two and three level inverter synchronous reluctance machine drives. Tables 2.7.1 and 2.7.2 show the summary of the simulation study, comparing a two and three level inverter SynRM drives at an approximate modulation index of 0.45 and 0.85 respectively. The three level inverter has lower THD for both current and voltage. The d-axis current for the three level inverter is also lower.

2.7.2 Experimental Results

Fig. 2.7.3 to 2.7.4 shows the experimental results of the performance of the synchronous reluctance machine with a two and a three level inverter.

Tables 2.7.3 and 2.7.4 show agreement with the simulation studies. The three level

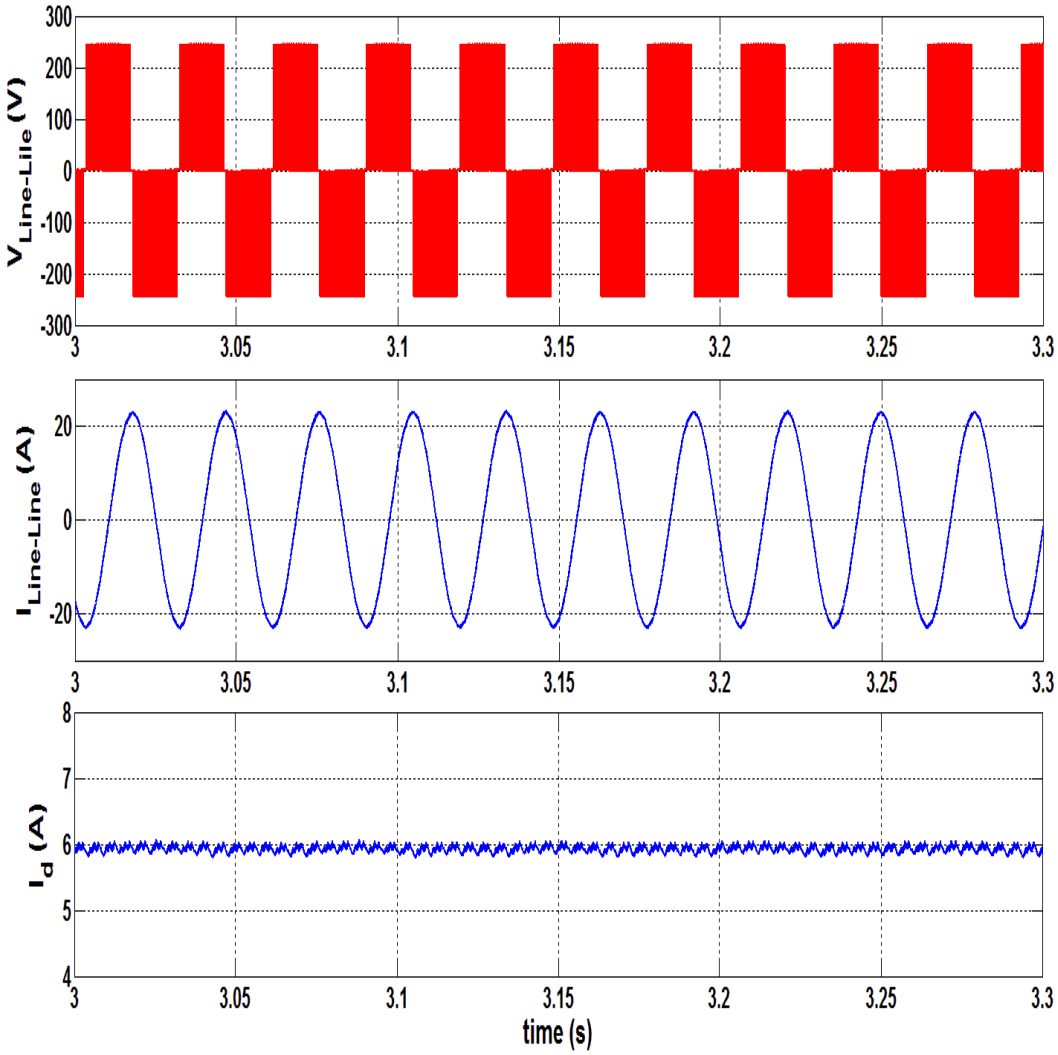

Figure 2.7.1: Simulation study of two level inverter performance at approximately 1032 rpm, (a) Line voltage, (b) Line current, (c) D-axis current and (d) dc bus input current

Table 2.7.1: Simulation studies on the comparison between a 2-level and 3-level inverter @ an average $m_i = 0.45$

Parameters	2-Level Inverter	3-Level Inverter
THD_i (%)	1.82	0.59
THD_v (%)	17.93	8.51
$Id_{average}$ (A)	2.98	3.06
Id_{ripple} (%)	8.73	6.02

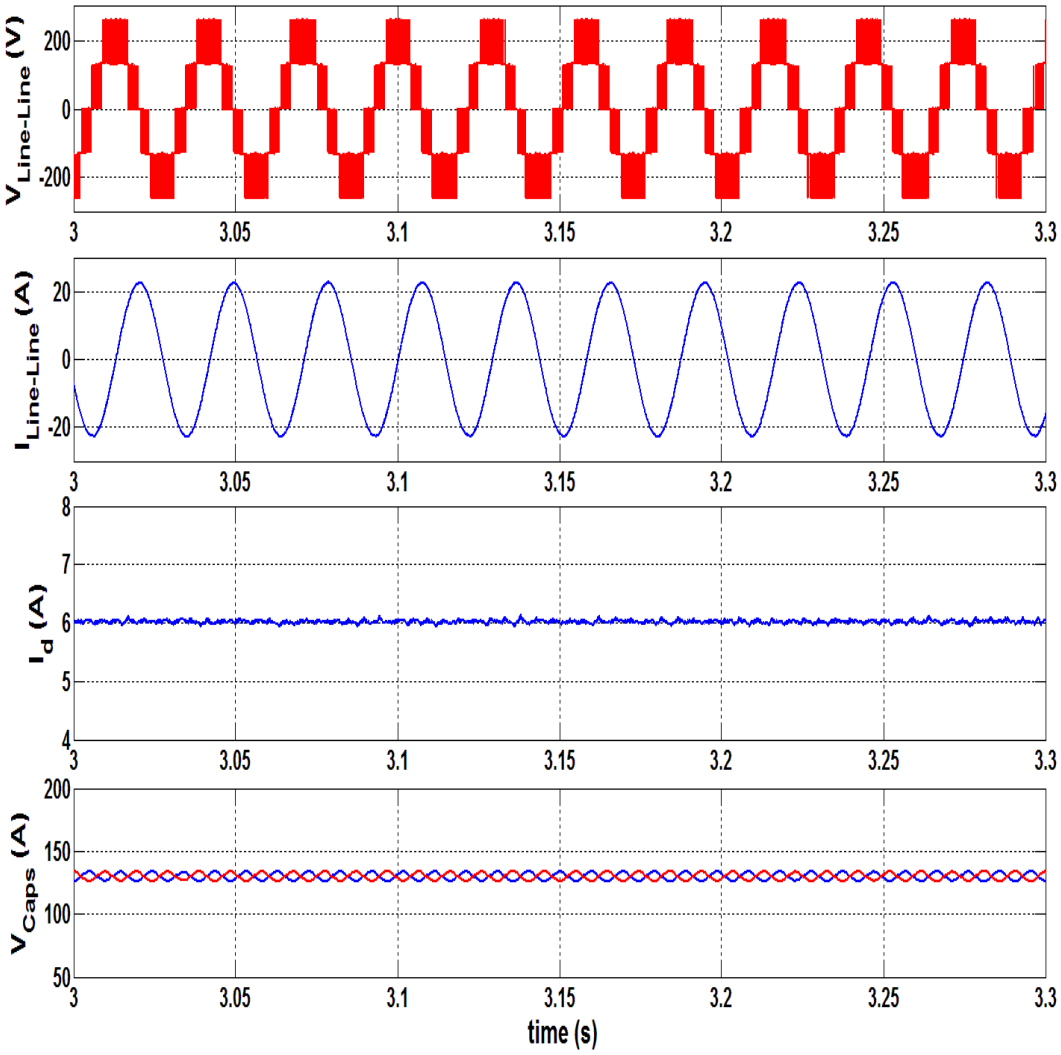

Figure 2.7.2: Simulation study of three level inverter performance at approximately 1032 rpm, (a) Line voltage, (b) Line current and (c) D-axis current and (d) Capacitor voltages

Table 2.7.2: Simulation studies on the comparison between a 2-level and 3-level inverter @ an average $m_i = 0.85$

Parameters	2-Level Inverter	3-Level Inverter
THD_i (%)	0.72	0.59
THD_v (%)	9.75	4.34
$Id_{average}$ (A)	5.92	6.02
Id_{ripple} (%)	4.49	3.50

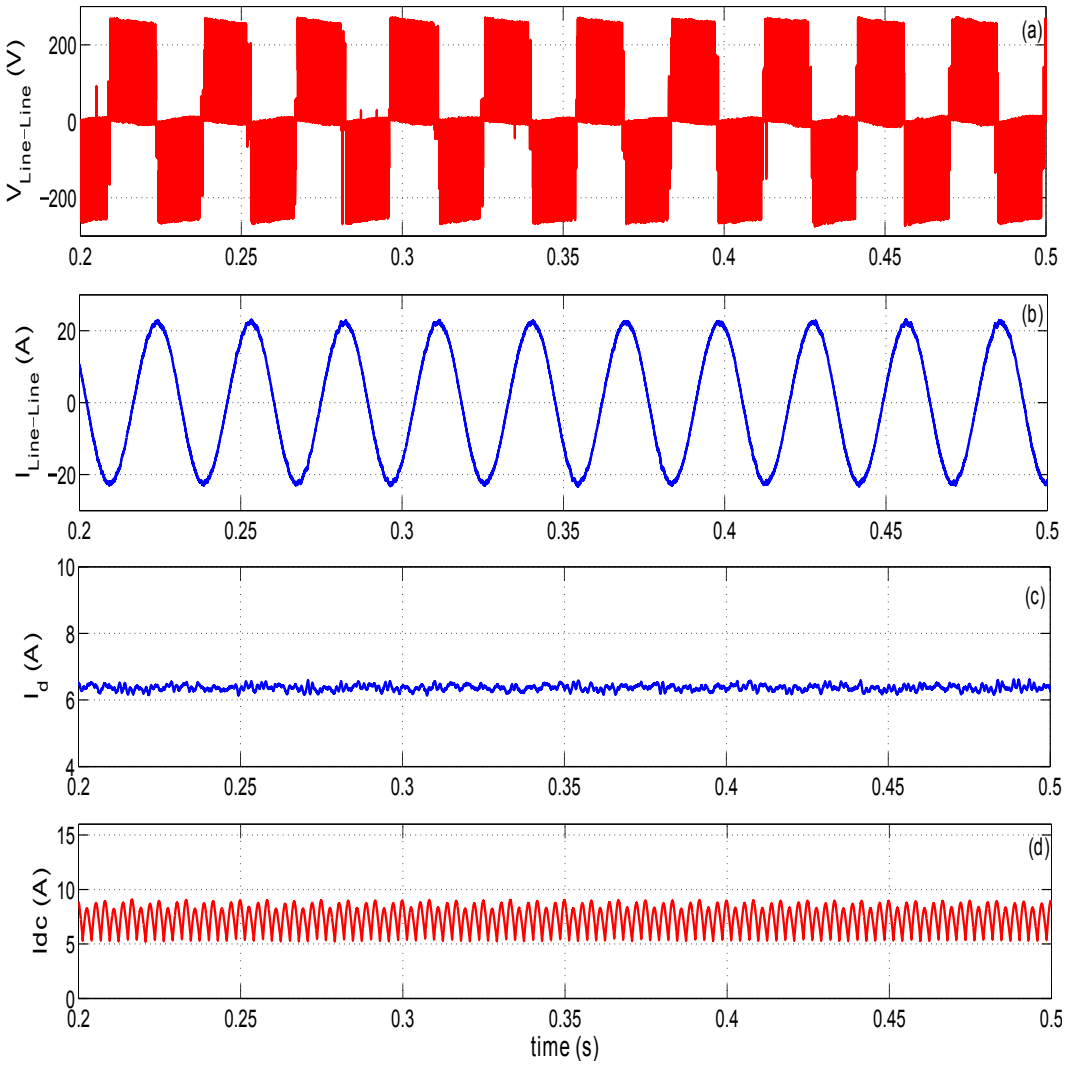

Figure 2.7.3: Two level inverter performance at approximately 1032 rpm, (a) Line voltage, (b) Line current, (c) D-axis current and (d) dc bus input current

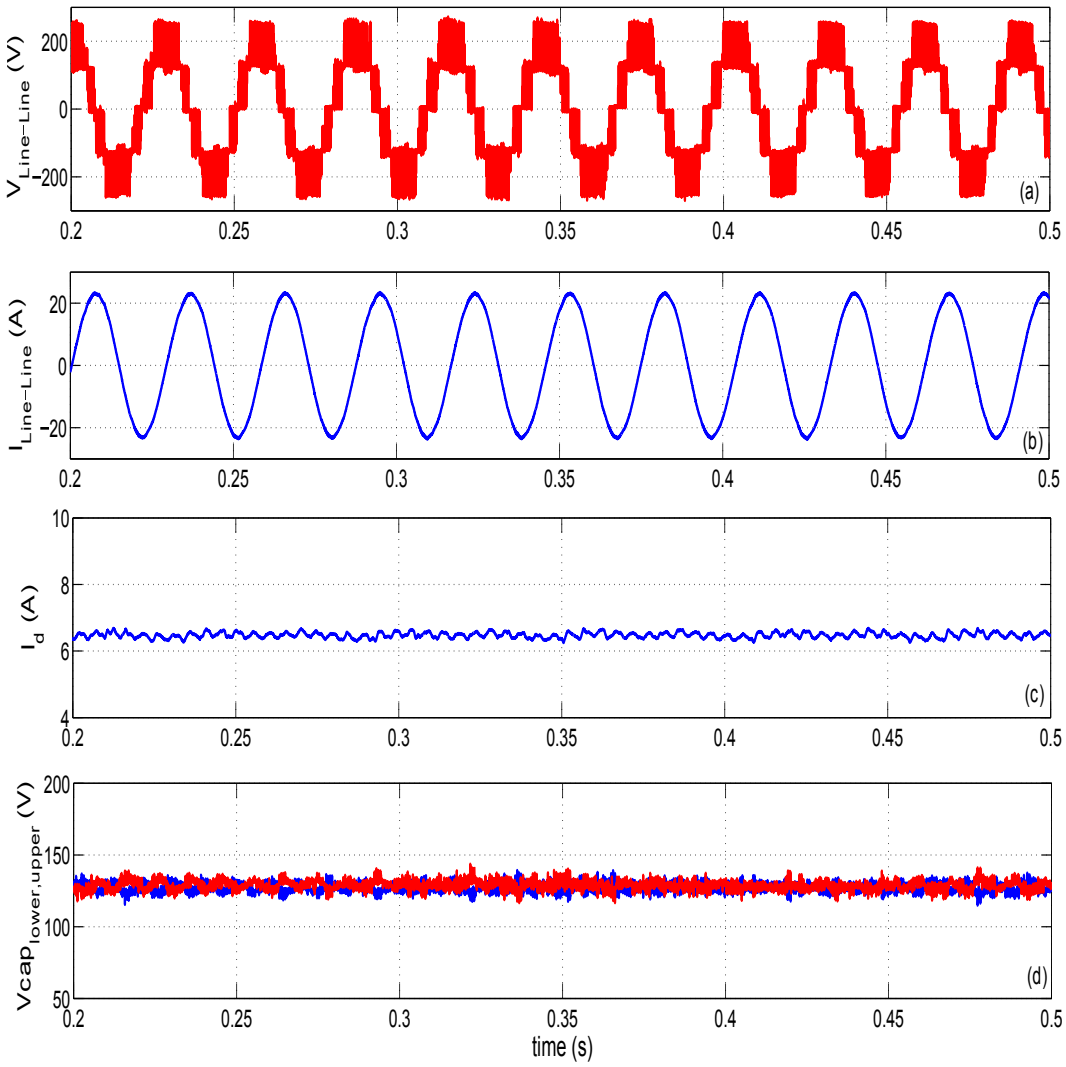

Figure 2.7.4: Three level inverter performance at approximately 1032 rpm, (a) Line voltage, (b) Line current and (c) D-axis current and (d) Capacitor voltages

inverter SynRM drive registered a lower THD_i and THD_v. The experimental results also confirm a lower d-axis current ripple on the three level inverter SynRM drive. This means that the SynRM under the three level inverter supply will experience lower pulsations in the magnetic flux. From this result it can be concluded that, the SynRM powered from a three level inverter will experience lower iron losses. Extensive analysis on the core losses of the SynRM when supplied by a three level inverter is conducted in chapter 4.

Table 2.7.3: Experimental studies on the comparison between a 2-level and 3-level inverter @ an average $m_i = 0.45$

Parameters	2-Level Inverter	3-Level Inverter
THD_i (%)	2.21	1.84
THD_v (%)	17.75	6.31
$Id_{average}$ (A)	2.58	2.62
Id_{ripple} (%)	31.84	6.97
$Idc_{average}$ (A)	1.35	2.17
Idc_{ripple} (%)	203.5	151.54

Table 2.7.4: Experimental studies on the comparison between a 2-level and 3-level inverter @ an average $m_i = 0.85$

Parameters	2-Level Inverter	3-Level Inverter
THD_i (%)	1.67	1.56
THD_v (%)	10.27	6.06
$Id_{average}$ (A)	6.40	6.41
Id_{ripple} (%)	17.10	10.24
$Idc_{average}$ (A)	7.43	8.36
Idc_{ripple} (%)	52.79	43.42

The source dc current ripple is also lower than that of a two level inverter. For electric vehicle applications this is a good advantage for the battery since it is the main source of

dc current. The lifespan of the battery would be improved over cases where a two level inverter would be used [28, 29]. The experimental dc current ripple are relatively high most especially at a modulation index of approximately 0.45. This can be attributed to the fact that the dc source was obtained from a six step diode rectif er and hence the dc ripple voltage also contributed to the dc current ripple.

2.8 Fixed Switching Frequency Modulation

The other challenge with the current NTV balancing algorithms is that they do not retain a constant switching frequency. A new balancing algorithm is proposed in [30], however additional regions are added to each sector of the hexagon. The switching frequency is also not constant since the switching steps are not constant across the space vector regions. In [22] a non-NTV modulation algorithm with additional regions in a sector was developed. This method guaranteed f xed switching frequency with six switching steps. Though balancing was achieved the method generated higher NP voltage ripples. Moreover due to the introduction of additional regions, the complexity of the algorithm was increased. In [31] a carrier based (CB) PWM method is introduced which completely eliminates the oscillations in the neutral point. However the drawback with this method is the increased switching frequency.

In [32] a new NTV algorithm is introduced and a comparison between a hysteresis and a PI controlled balancing algorithm were also conducted. However in this method the switching frequency is not f xed since the switching steps are not constant throughout the space vector. There are regions were two switching states occurs at the same time. The algorithm in this work is similar to the algorithm developed by [32], however in this

work the switching frequency is fixed. There are no additional regions or complexity on the SVM. There are only four switching steps in the voltage sequence and there is only one switching state at the same time. This means that the proposed method also favors lower switching losses. Table 2.8.1 shows a modulation algorithm with a fixed switching frequency. Column five shows the number of the switching steps.

Table 2.8.1: Sector 1 of the switching table on phase A

NP Voltage State	Triangle	Sequences	Steps
$V_{c1} > V_{c2}$	1	000, 100, 110, 100, 000	4
$V_{c1} < V_{c2}$	1	-1-1-1, 0-1-1, 00-1, 0-1-1, -1-1-1	4
$V_{c1} > V_{c2}$	2	100, 10-1, 1-1-1, 10-1, 100	4
$V_{c1} < V_{c2}$	2	10-1, 1-1-1, 0-1-1, 1-1-1, 10-1	4
$V_{c1} > V_{c2}$	3	110, 100, 10-1, 100, 110	4
$V_{c1} < V_{c2}$	3	10-1, 00-1, 0-1-1, 00-1, 10-1	4
$V_{c1} > V_{c2}$	4	110, 11-1, 10-1, 11-1, 110	4
$V_{c1} < V_{c2}$	4	11-1, 10-1, 00-1, 10-1, 11-1	4

Column three shows the control ability of the algorithm and column five shows the switching steps for the chosen voltage sequence. For every switching step from one state to the next only one switch switches at a time. Since there are five voltage states in each voltage sequence there are only four switching steps. Fig. 2.8.1 shows some of the converter different voltage states as described in Table 2.8.1. The capacitor voltage balancing ability of the algorithm is best described in Fig. 2.8.1 (a) and (b). Fig. 2.8.1 (a) and (b) shows a discharge of $C1$ and $C2$ respectively. The information of the voltages across the two capacitors is sent to the algorithm described in Table 2.8.1. The appropriate voltage state is then chosen to balance the two capacitor voltages.

Fig. 2.8.2 shows balanced capacitor voltages with a 3% NP voltage ripple. The SynRM

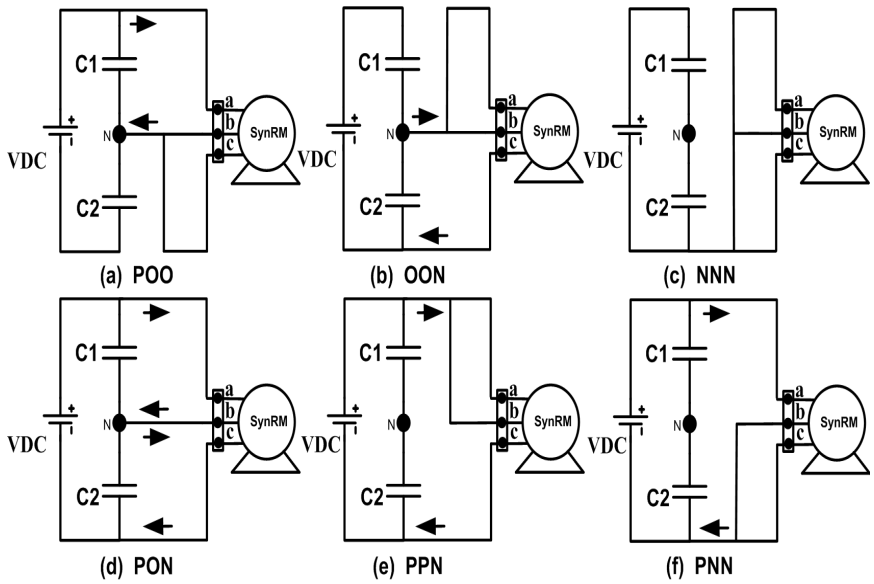

Figure 2.8.1: Different voltage states of a three level inverter

was run at approximately 1000 rpm with a load torque of 15 N.m. operated with the proposed f xed swiching frequency algorithm.

Fig. 2.8.3 shows the response of the proposed algorithm on the speed change of the machine. The speed was changed from 200 rpm to 1000 rpm. The proposed algorithm performed well during the speed change.

Fig. 2.8.4 shows the induced load torque with a speed control. The speed controller continues to maintain the same speed while the torque is changed from 0 N.m to 6.5 N.m. As the motor is loaded the modulation index increases to approximately 0.7. The NP voltage ripple also increases at higher modulation index since there is less dwell time for the small vectors.

As compared to a permanent magnet synchronous machine the input current at no load is higher. This is because of the magnetization current required in the SynRM. The power factor was very low as 0.3, yet the proposed algorithm could achieve voltage balance across

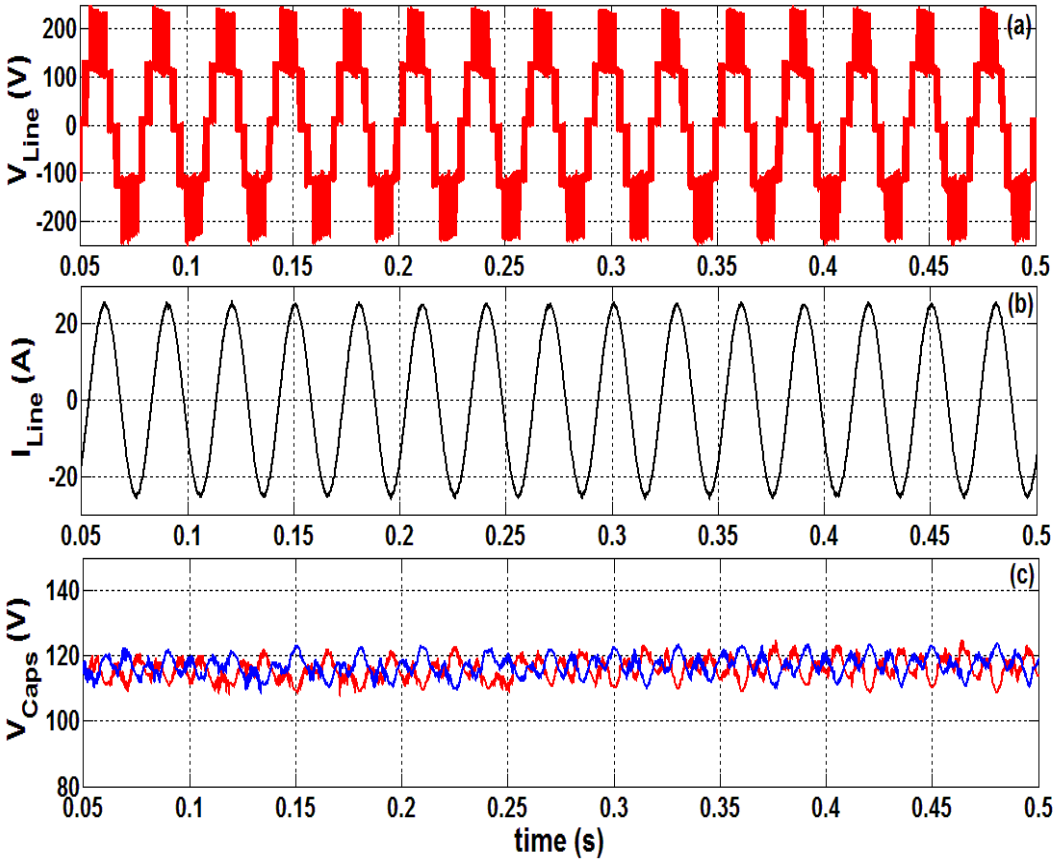

Figure 2.8.2: The machine was running at 1000 rpm with an approximate torque of 15 N.m, (a) line to line voltage, (b) line to line current and (c) dc link capacitor voltages.

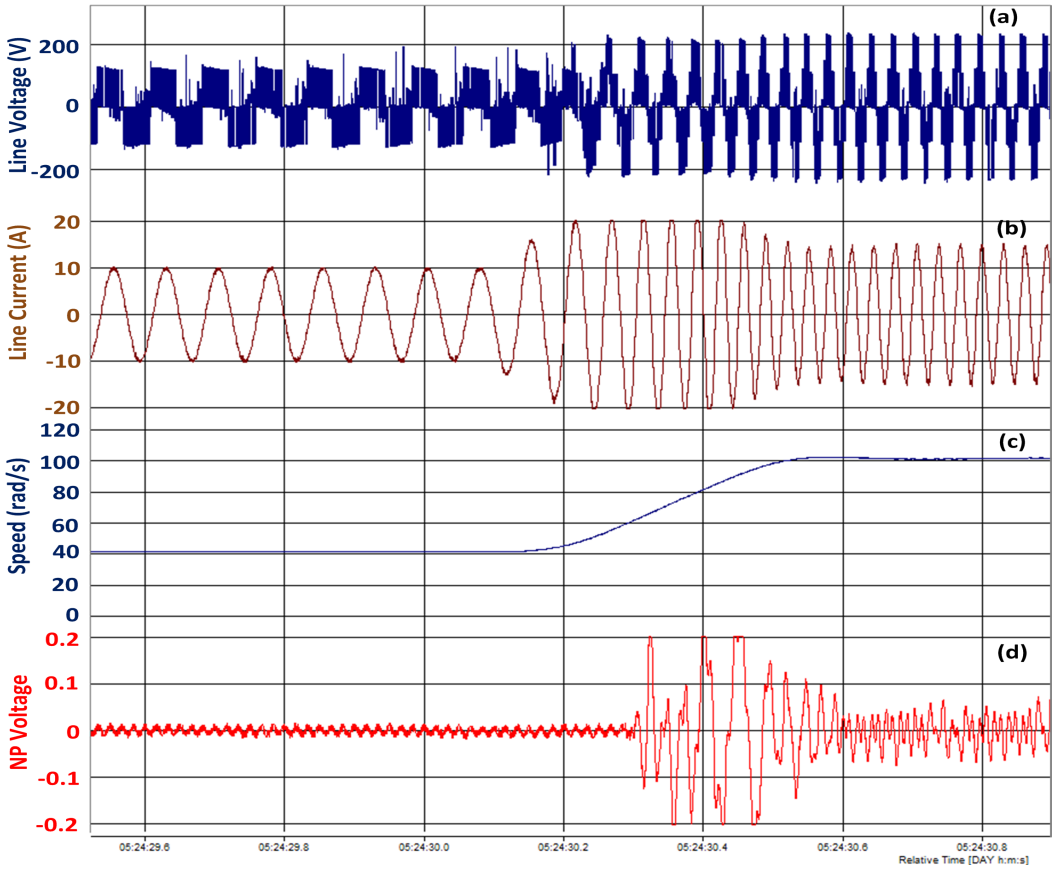

Figure 2.8.3: Speed change from 400 rpm (42 rad/s) to 1000 rpm (105 rad/s), up to a modulation index of 0.7, (a) line to line voltage, (b) line to line current and (c) speed in rad/s and (d) NP voltage ripple ($(V_{c1} - V_{c2})/V_{dc}$)

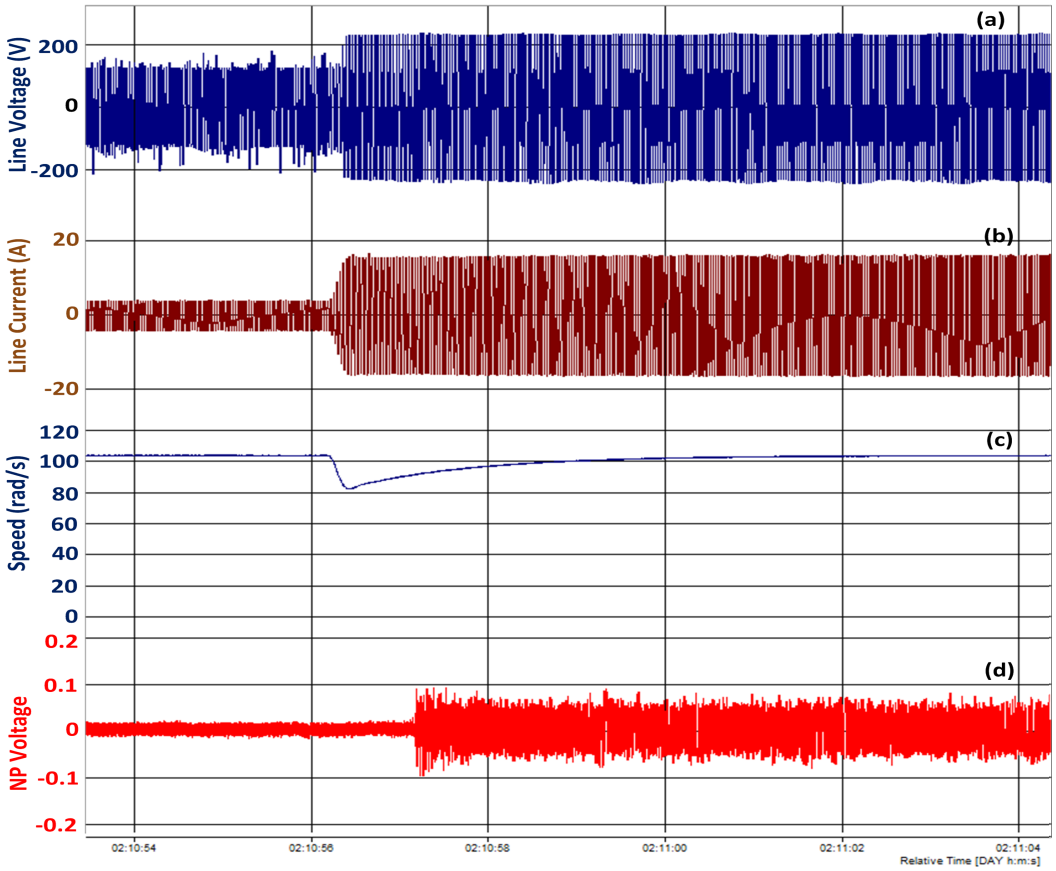

Figure 2.8.4: Torque change from approximately 0 N.m to 6.5 N.m up to a modulation index of 0.7, with speed control, (a) line to line voltage, (b) line to line current, (c) speed response in rad/s and (d) NP voltage ripple ($(V_{c1} - V_{c2})/V_{dc}$)

the two capacitors.

2.9 Summary

A new modulation scheme called Mod-1 was proposed for a three level inverter drive. The proposed modulation scheme achieved capacitor voltage balancing during both speed and torque transients inspite a relatively lower power factor. A comparison between a three level and two level inverter drives was also conducted. The three level inverter drive registered lower current and voltage THD. This means that a three level inverter SynRM will have lower torque ripple which is benef cial for the HEV/EVs. This work also introduced the saliency ratio as one of the parameters for the dc link capacitor sizing. A higher saliency ratio does not only promote better machine performance but also contributes to the reduction of the dc link capacitor size. A method of sizing the dc link capacitors based on the machine size was also proposed.

CHAPTER III

LOW COST HIGH RESOLUTION POSITION SENSOR FOR THE SYNCHRONOUS RELUCTANCE MACHINE

3.1 Introduction

For high performance control applications the SynRM drive system requires absolute rotor position and speed information. The accuracy of the position information is critical for low torque ripple and high performance applications. This information can normally be obtained from the rotor position sensors which are normally mechanically coupled to the rotor shaft.

In recent years there has been extensive research work on the elimination of the position sensor in favor of increased mechanical robustness and reduced cost. Position sensor-less control algorithms and their applications have been studied over the past years [33, 34, 35, 36]. Generally two types of position estimation algorithm are used for traction drive, one is based on back electromotive force (EMF) and the other on magnetic saliency [37].

Magnetic saliency methods can estimate the rotor position at standstill [38, 39, 40], whereas back EMF methods produce good performance at medium to high speed ranges [37, 41]. The performance of the magnetic saliency based methods degrade during high torque operations due to magnetic saturation. This has led to a number of proposed solutions such as concentrated windings and advanced signal injection based methods for sensor-less control [42, 40]. Work on a hybrid method which combined the magnetic saliency method and

the back EMF was conducted in [37]. This allowed for low speed to high speed application which are suitable for EV/HEV application. However these methods depend on the accuracy of the current information to calculate absolute rotor position and pose risks during transients.

Sensorless methods still pose safety concerns and there is no performance guarantee for the entire speed and torque range [43]. The position sensor is still a requirement especially for EV/HEV application were safety is of great concern. Reliable operation is highly essential to the safety of the driver, passengers, other road users and pedestrians. A position sensor should therefore be extremely robust and perform reliably for the lifetime of the vehicle.

Low cost, low resolution Hall sensor based position sensors have also been proposed [44, 45]. However their applications are limited due to low resolution. Two linear Hall sensors which are normally mounted adjacent to the stator winding electrically displaced by 90^0 have also been in use [46]. These sensors are relatively low-cost compared to traditional encoders however the torque producing component of the stator current causes a phase delay. An extended second-order Kalman f lter (EKF) to resolve its associated problems was proposed in [46]. However the phase delay may still exist since the error in the estimation depends on the speed and the load. Another major concern is that placing the Hall sensors within the machine poses practical problems, fault in the sensor means removing the whole machine from the drive train.

This work proposes a low cost high resolution contact-less Hall-effect rotor position sensor for electric drive applications. The algorithm to generate the position from the two

signals is relatively simple with insignif cant computational cost. This chapter also discusses the benef ts of the low cost position sensor over the digital Hall effect position sensor used in the electric power steering (EPS) machines. The EPS machines are predominantly used in vehicles and this work also proposes the low cost position sensor as an alternative for the position sensor used in EPS machines.

3.2 Low Cost Position Sensor Assembly

The position sensor assembly is composed of a linear Hall sensor board and a 2 pole permanent magnet as shown in Fig. 3.2.1. The magnet has a diameter of 6 mm and is mounted

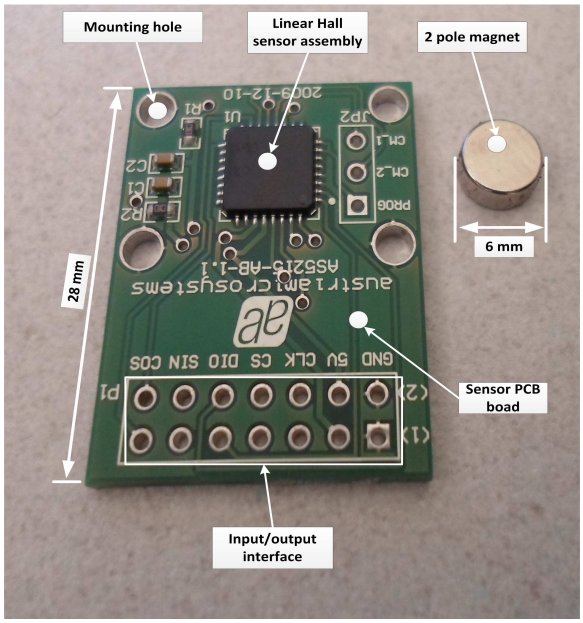

Figure 3.2.1: Low cost position sensor assembly

on the shaft of the rotor as shown in Fig. 3.2.2. When the rotor rotates the Hall sensors experience sinusoidal magnetic f eld which are processed into sine and cosine analogue signals from the internal circuit. Fig. 3.2.3 shows the low cost position sensor mounted on the SynRM. As can be seen from Fig. 3.2.2 there are certain specif cations that needs to be

met, the magnet should be placed at a maximum distance of 1-2 mm from the sensor board. This distance places the Hall senor within the linear range of the magnetic f eld. The computation of the rotor position information from the two analog signals is conducted through equation (3.2.1).

$$\vartheta = arctan\left(\frac{V_{sin}}{V_{cos}}\right) \tag{3.2.1}$$

V_{sin}, V_{cos} and ϑ are the two analog signals from the position sensor board and mechanical rotor position respectively.

A comparison of volume, mass and cost among encoder, resolver and Hall sensor based on same resolution was conducted by [1] and is presented in Table 3.2.1. The linear Hall

Table 3.2.1: Comparison among resolver, encoder and Hall sensor [1]

Sensor types	Volume	weight	Cost
Resolver	Medium	Medium	Medium
Encoder	Small	Medium	expensive
Hall sensor	Small	Light	Cheap

sensor technology does not only reduce cost but it is also lighter and smaller in size.

3.3 Position Sensor Performance

One of the major concerns with the low cost position sensor assembly is the misalignment of the mechanical placement of the sensor board and magnet axis. This results in undesired harmonics, amplitude variation, phase shift and a dc offset. Fig. 3.3.1 shows the sensor and the two pole magnet perfectly mechanically aligned whereas Fig. 3.3.2 shows the misalignments. The harmonics results from magnetic anisotropies, run out and eccentricities, the phase shift error results from the two signals not being in perfect quadrature and lastly the dc offset is caused by the magnetization, vibrations in the dc bias in the sensor signals [47].

The low cost position sensor errors were analyzed and a calibration procedure intended for high performance and low torque ripple applications was developed in [47]. This method is an off-line method which was intended for low speed applications (electric power steering (EPS)), however for high speed applications other mechanical parameters begin to take a major role such as vibrations. Equation (3.3.1)-(3.3.8) describes the mathematical representation of the errors mentioned above:

1. *Amplitude mismatch*

$$\vartheta = arctan\left(\frac{(1+k)sin(\theta)}{cos(\theta)}\right) \tag{3.3.1}$$

and the resulting error is:

$$\epsilon = \vartheta - \theta \approx tan(\epsilon) = \frac{ksin(2\theta)}{2 + k[1 - cos(2\theta)]} \tag{3.3.2}$$

2. *DC offset*

$$\vartheta = arctan\left(\frac{sin(\theta) + r}{cos(\theta)}\right) \tag{3.3.3}$$

and the resulting error is:

$$\epsilon = \vartheta - \theta \approx tan(\epsilon) \approx \frac{rcos(\theta)}{1 + rsin(\theta)} \tag{3.3.4}$$

3. *Phase shift*

$$\vartheta = arctan\left(\frac{sin(\theta + \delta)}{cos(\theta)}\right) \tag{3.3.5}$$

and the resulting error is:

$$\epsilon = \vartheta - \theta \approx tan(\epsilon) \approx \delta cos^2(\theta) = \frac{\delta}{2}(1 + cos(2\theta)) \tag{3.3.6}$$

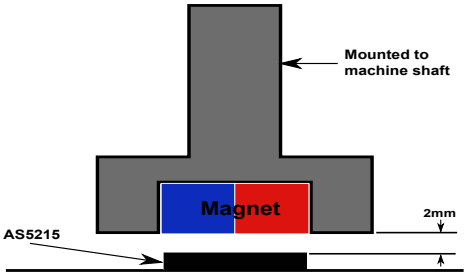

Figure 3.2.2: Mechanical assembly

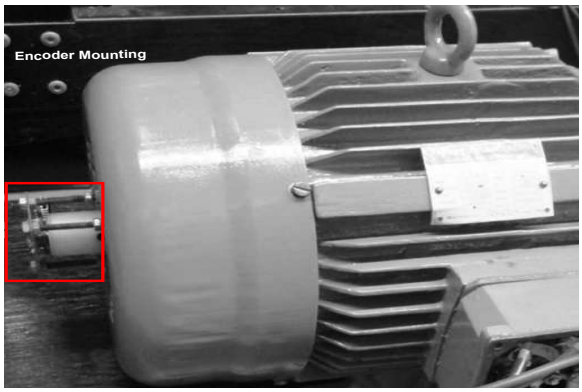

Figure 3.2.3: Mechanical mounting on the SynRM

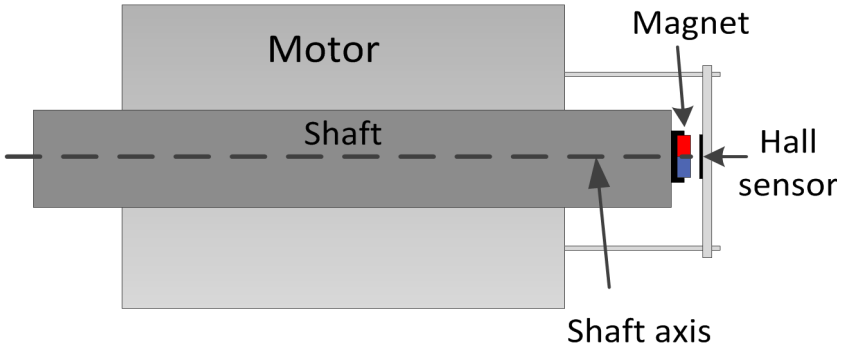

Figure 3.3.1: Position sensor aligned with the two pole magnet

4. *n^{th} order Harmonic*

$$\vartheta = arctan\left(\frac{sin(\theta) + k_n sin(n\theta)}{cos(\theta) + k_n cos(n\theta)}\right) \tag{3.3.7}$$

and the resulting error is:

$$\epsilon = \vartheta - \theta \approx tan(\epsilon) = \frac{k_n sin(n\theta + \theta)}{1 + k_n cos(n\theta - \theta)} \tag{3.3.8}$$

ϑ, θ, k, and r is the decoded rotor angle, actual rotor angle, amplitude constant and dc offset constant. From equation (3.3.6) it can be seen that the error due to the signals not purely orthogonal results in a dc component and an amplitude of cosine function. This makes the orthogonal error a key component to be suppressed for position angle accuracy.

Fig. 3.3.3 shows the harmonic analysis of the quadrature signals. The captured signals had relatively low errors, the alignment of the magnet with the sensor board were almost perfect. The sine signals had a dc component and both the signals had a very small second order harmonic with slight magnitude difference. Fig. 3.3.4 shows the Hall effect sensor position error over a 360 mechanical degrees rotation. The Hall effect position sensor was compared with a 12-bit optical industrial encoder. The proposed position sensor registered an error of less than 1 mechanical degree. The shaft was rotated by hand so as to avoid errors due to the power electronics.

3.3.1 Speed Estimation

A phase lock loop is used to estimate the speed of the rotor as shown in Fig. 3.3.5. Equation (3.3.9) describes the input to the PI controller and by the use of small signal theory the speed of the rotor shaft can be computed. A Matlab sisotool was used to compute the gains of the PLL k_p and k_i gains. However for actual applications on a EV/HEV these gains will

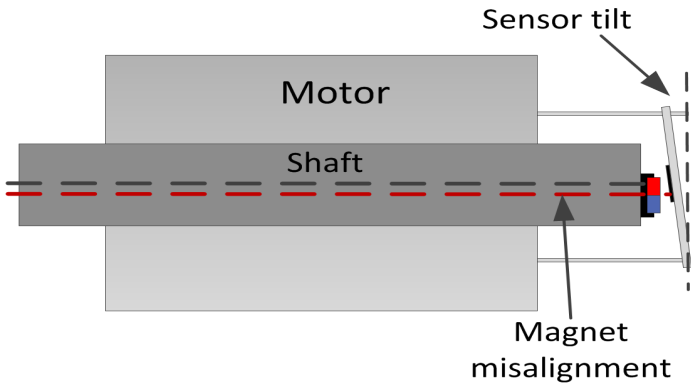

Figure 3.3.2: Misalignment of the position sensor and the two pole magnet

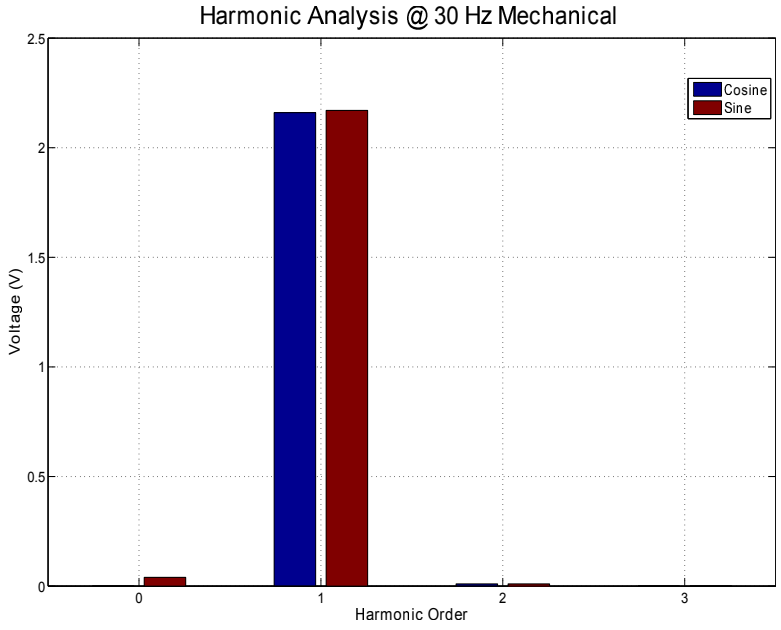

Figure 3.3.3: Harmonic analysis of the generated sine and cosine signals

still need to be tuned based on safety standards.

$$\begin{aligned} sin(\theta)cos(\phi) - cos(\theta)sin(\phi) &= sin(\theta - \phi) \\ &\approx \theta - \phi \end{aligned} \tag{3.3.9}$$

θ, ϕ is the rotor position, estimated rotor position and ω is the rotor speed respectively. The resolution of the rotor position depends on the sampling time of the microprocessor.

3.4 Machine Control

A vector controller was implemented for varying the machine speed. Fig. 3.4.1 shows the vector control (FOC) drive for a SynRM using the current signal as the torque command. Block C in Fig. 3.4.1 decouples the reference ${I_s}^2$ into the reference d-q currents by the use of equation (refd1) and (3.4.2).

$$i_d^* = i_s cos(\theta_s) \tag{3.4.1}$$

$$i_q^* = i_s sin(\theta_s) \tag{3.4.2}$$

The angle θ_s was found through a standstill experimental test as discussed in chapter 2.

3.5 Experimental Set-up and Results

A real time based operating system called Opal-RT was used for the experimental studies. Fig. 3.5.1 shows the experimental set-up used to analyze the performance of the low cost position sensor on a SynRM. Fig. 3.5.2 shows two quadrature signals generated from the sensor board whiles the machine was run at 1800 rpm. Two performance tests were conducted, f rstly the speed was increased from zero to approximately 94 rad/s (900 rpm). Secondly, the test was conducted at low speeds of approximately 10 rpm at a lower torque. The machine was loaded through a generator coupled to a resistive load bank, hence at

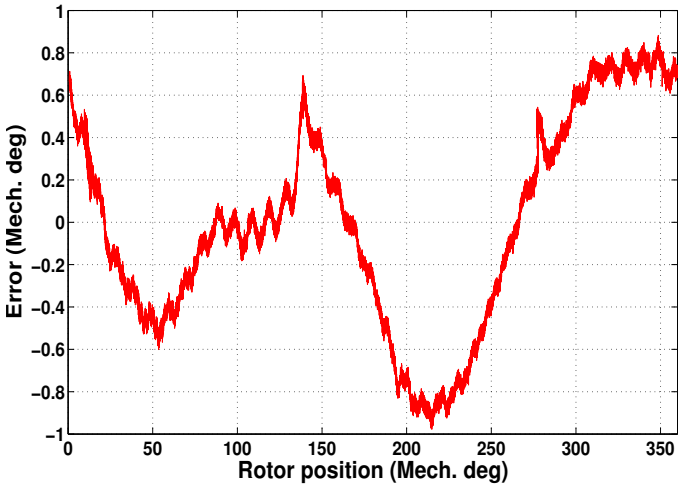

Figure 3.3.4: Proposed position sensor error

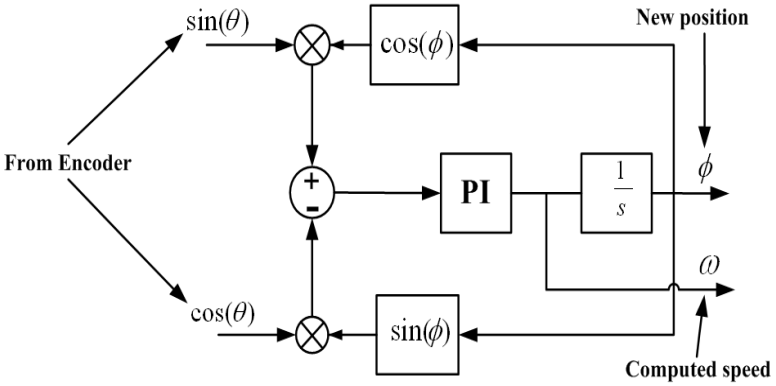

Figure 3.3.5: Phase lock loop for speed estimation

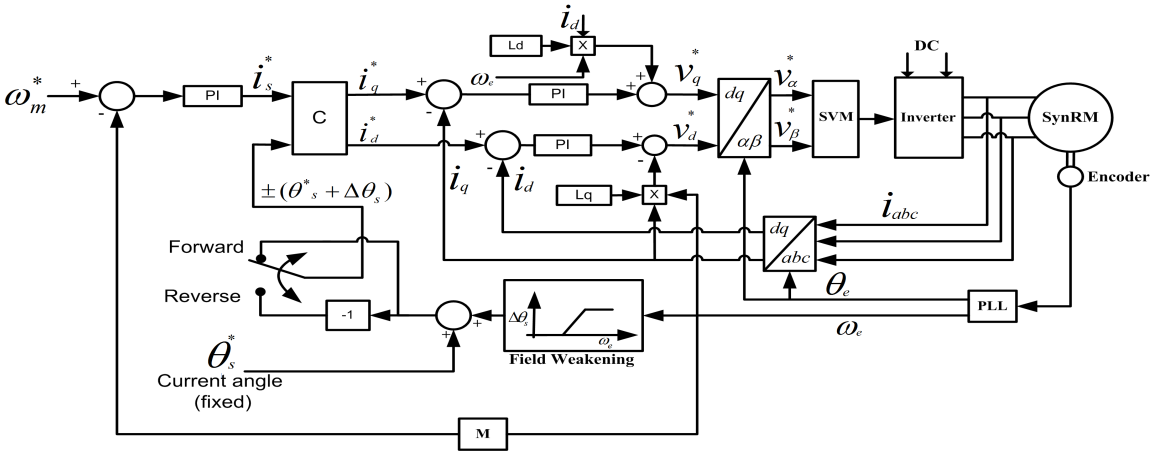

Figure 3.4.1: Vector Control of SynRM using angle control

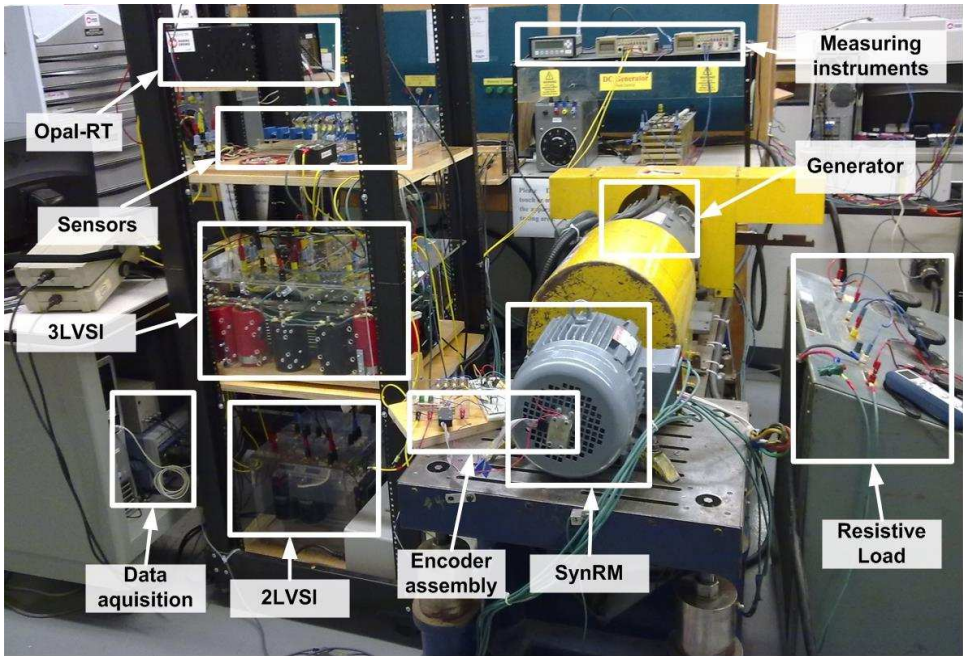

Figure 3.5.1: The SynRM drive using a low cost position sensor

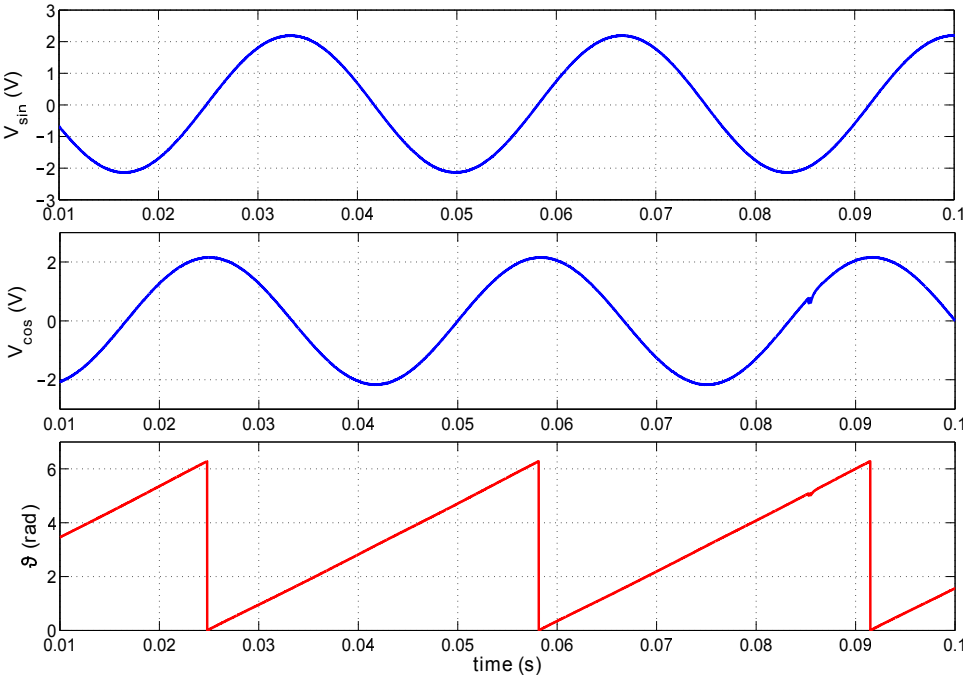

Figure 3.5.2: Rotor position angle extraction at 1800 rpm

low speeds not much load torque was imposed on the machine. Figs. 3.5.3 and 3.5.4 show the first and second performance test results respectively. It can be seen from Fig. 3.5.3

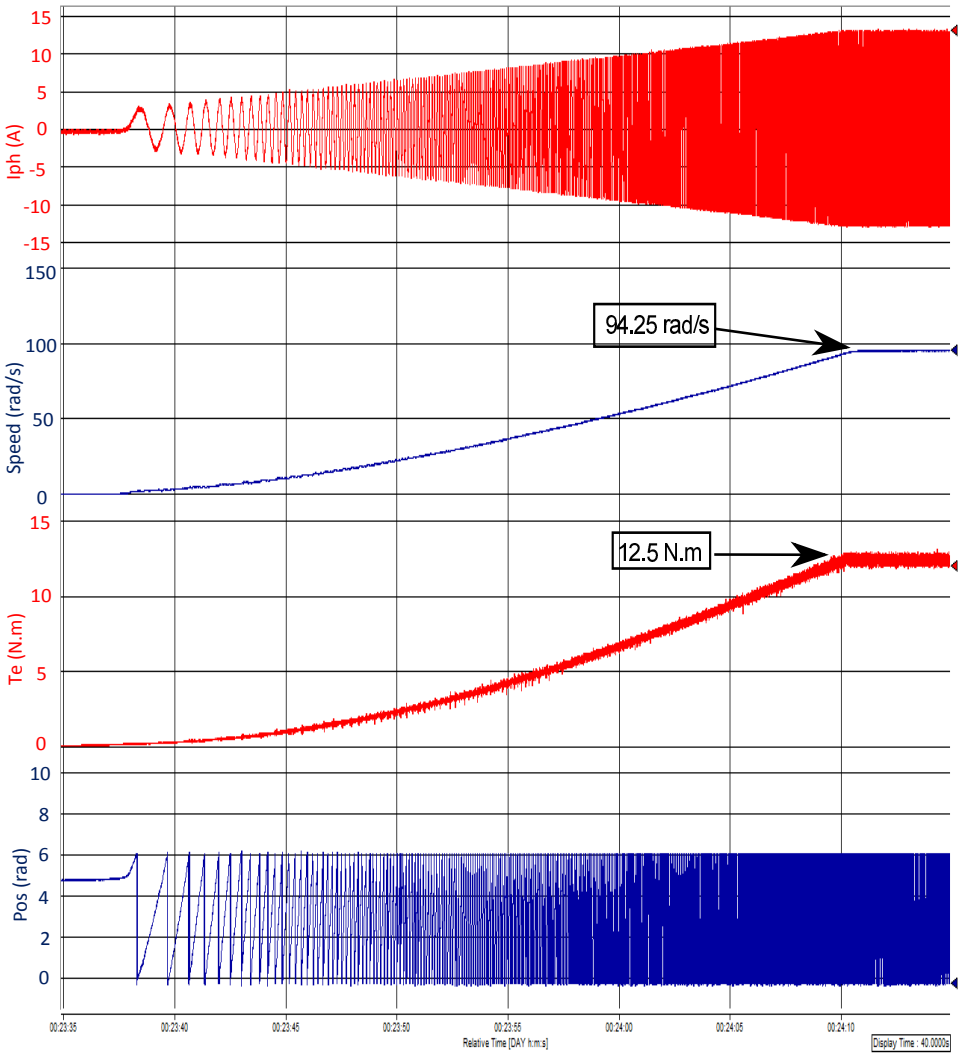

Figure 3.5.3: Zero speed to approximately 900 rpm, from top to bottom: (i) Phase current, (ii) speed response, (iii) estimated toque response and (iv) rotor position (electrical position) at 5 sec/div time scale

that as the speed of the machine was ramped up from zero speed to 900 rpm the load torque also increased. This is indicated by the increasing stator current as the machine load torque increased with speed. Fig. 3.5.5 shows the low speed control using a speed loop, the speed could be controlled down to approximately 6 rpm however with higher torque ripples.

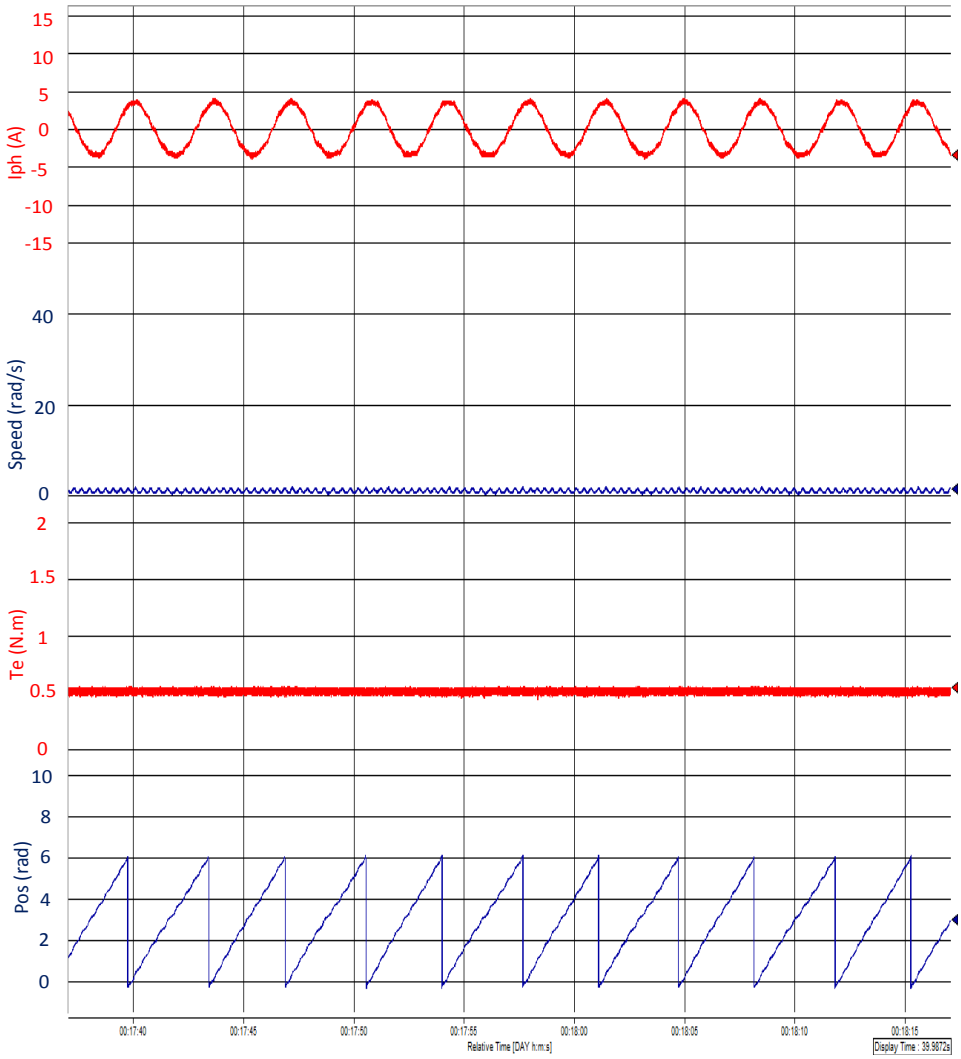

Figure 3.5.4: Almost zero speed performance, from top to bottom: (i) Phase current, (ii) speed response, (iii) estimated toque response and (iv) rotor position (electrical position) at 5 sec/div time scale

Table 3.5.1 shows the torque ripple of the machine both at low speeds and higher speeds.

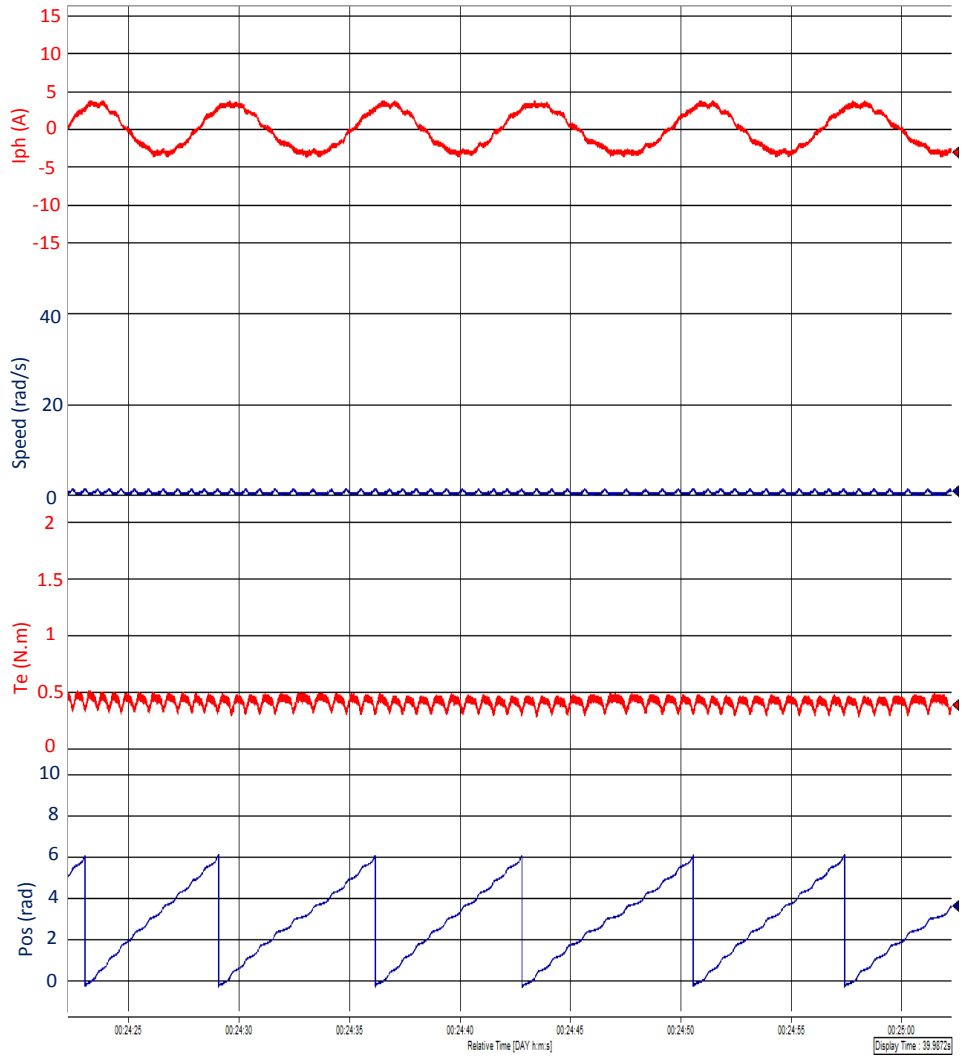

Figure 3.5.5: Almost zero speed performance, from top to bottom: (i) Phase current, (ii) speed response, (iii) estimated toque response and (iv) rotor position (electrical position), at 5 sec/div time scale

To capture one cycle of the current at 12 rpm would require a time window of 2.5 sec. However to conduct an FFT would require several number of cycles and due to limited memory this could not be conducted hence no THD_i for the low speed in Table 3.5.1. The torque ripple and the THD of the current waveform were parameters of interest because the rotor position information ultimately affects the phase currents and hence the torque ripple. This

is because the vector control used depend on the Park transformation which uses the rotor position information. Hence any errors on the low cost position sensor will be ref ected on the current waveforms and the torque. The THD_i at higher speeds was below 2%.

The torque ripple at relatively low and higher speed was at 14.36% (for a torque less than 1 N.m) and 8.47% respectively. The Toyota Prius, one of the hybrid vehicles in the market has a torque ripple of 26.2% at rated torque [48]. In[49] it was shown that the other Prius PM machine had a torque ripple of aproximatetly 12%. A low cost ferrite PM assisted synchronous reluctance machine for EVs which had a torque ripple of 13% was proposed in [48]. At approximate full load a torque ripple of less than 9% was archieved. The torque ripples are also due to the way the machine is designed, however the position sensor used will contriute to the additional torque ripple. It was shown that the linear Hall effect position sensors have strong anti-temperature drift performance when exposed to -20^0C to 100^0C [1].

The response of the position sensor was also evaluated when the machine changes rotational direction. The machine was run at approximately -110 rad/s (-1000 rpm) with a torque of approximately -14 N.m and then within a period of 7.5 sec the machine rotational direction was changed. Fig. 3.5.6 shows the performance of the position sensor during a change in rotational direction. The direction of rotation is changed through injecting a negative reference angle (i.e. $\theta_s = -60^0$). When the reference current was small enough to stop the machine to stand still a negative reference phase angle was injected at the same time incrementing the reference current vector to 13 A.

Table 3.5.1: Summary of Experimental Results

Condition	$Torque_{ripp}$ (%)	THD_i (%)
Low speed ($\approx 12\ rpm$) @ $\approx 0.4\ N.m$	14.36	–
Higher speeds ($\approx 1035\ rpm$) @ $\approx 14\ N.m$	8.47	< 2

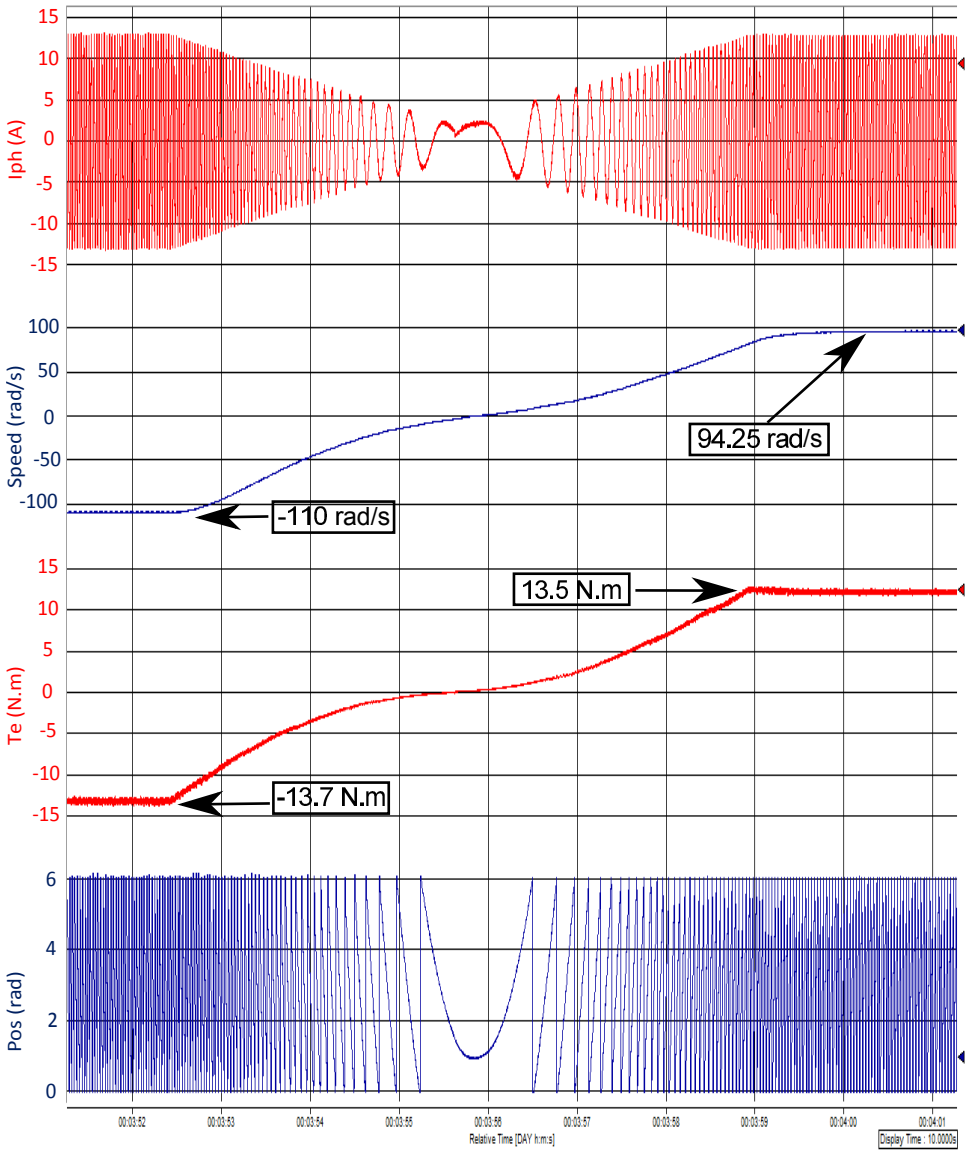

Figure 3.5.6: Change of rotational direction, from top to bottom, (i) phase current, (ii) speed response, (iii) estimated toque response and (iv) rotor position (electrical position), at 1 sec/div time scale

3.6 Electric Power Steering (EPS) Position Sensor

Fig. 3.6.1 shows the EPS machine with a position sensor which uses digital Hall sensors. The sensors are under the inf uence of two set of magnet poles, one 6 pole and the other 72 pole. The 6 pole magnets are for low resolution whereas the high resolution sensors generate 72 pulses per mechanical revolution as shown in Fig. 3.6.2 (ii) and (iii). The

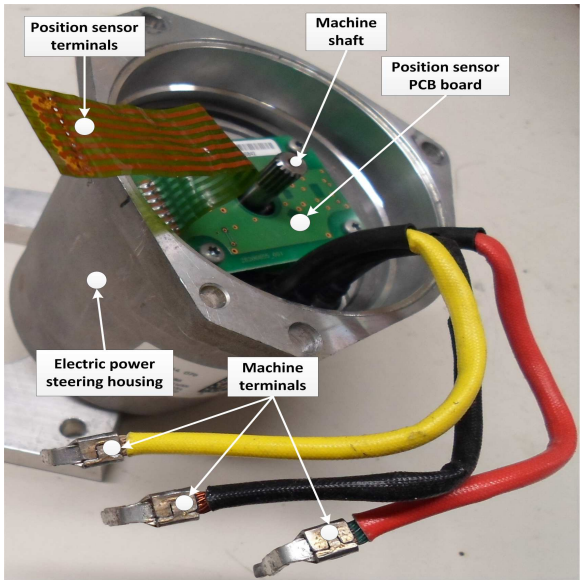

Figure 3.6.1: Electric power steering permanent magnet synchronous machine with digital Hall effect position sensor assembly

high resolution signals are used for speed computation and the low resolution signals for the initial detection of the rotor position and calibration. The low resolution signals behave like a space vector hexagon within the α and β domain as shown in Fig. 3.6.3. If ”A” is high while ”B” and ”C” are low the reference position of the rotor is located at the alpha (α) position. Each sector has a 60 mechanical degrees span. The low resolution signals serve to identify the sector the rotor is in and hence behave as a reference for the high resolution signals. Once the sector is identif ed the high resolution pulses are used to improve the resolution of the rotor position information. The low resolution signals are therefore used

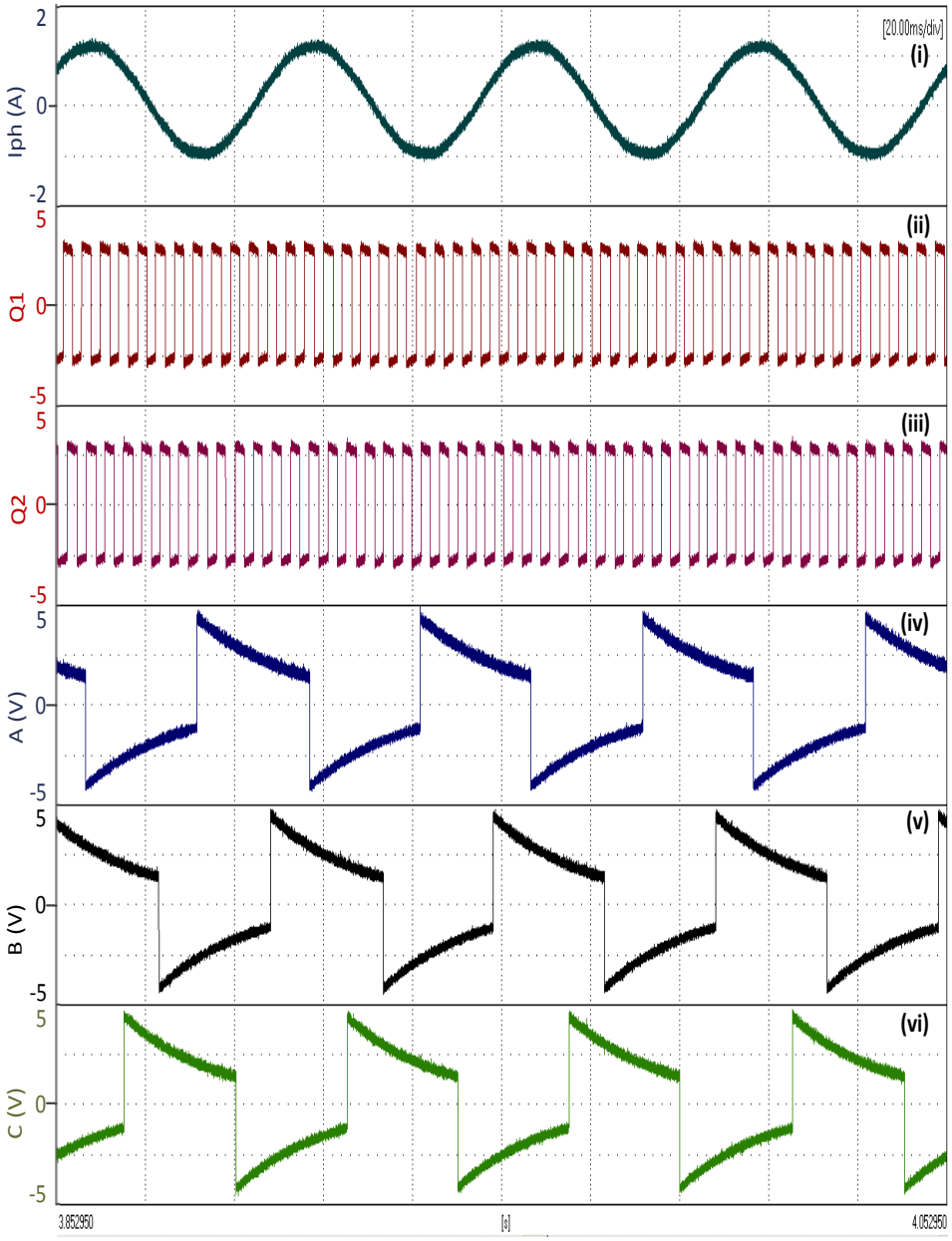

Figure 3.6.2: Analog rotor position for electric power steering machine, (i) phase current, (ii) and (iii) high resolution pulses Q1 and Q2 respectively, (iv), (v) and (vi) low resolution signals, A, B and C respectively

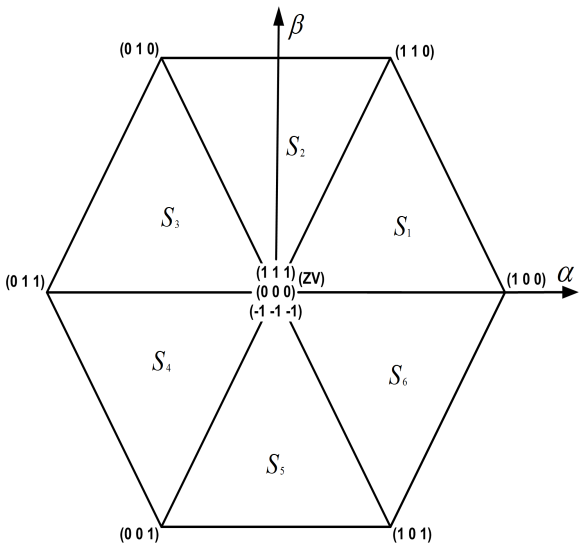

Figure 3.6.3: Hexagon for the low resolution signals of the EPS machine position sensor as a framework of calibrating the position sensor for vector control application.

3.6.1 Discussion on the Two Position Sensors

The position sensor used in the EPS machine uses a relatively complex algorithm to process the signals for position information and hence a higher computational cost for the microprocessor. The resolution is also at 5 mechanical degrees which could be improved to 2.5 mechanical degrees at an added computational cost. Fig. 3.6.4 shows the rotor position of the low cost position sensor and that of the position sensor used in the EPS machine. The low resolution of the position sensor used in the EPS machine can clearly be seen from Fig. 3.6.4 (ii) as compared to the rotor position information from the low cost position sensor in Fig. 3.6.4 (i).

The disadvantage of the low cost position sensor is the position errors that result from mechanical misalignment as discussed in section 3.2. The two feasible solutions are, f rstly, the use of a compensation algorithm for the misalignments which will add to the computational cost and secondly the development of the special housing for the low cost position

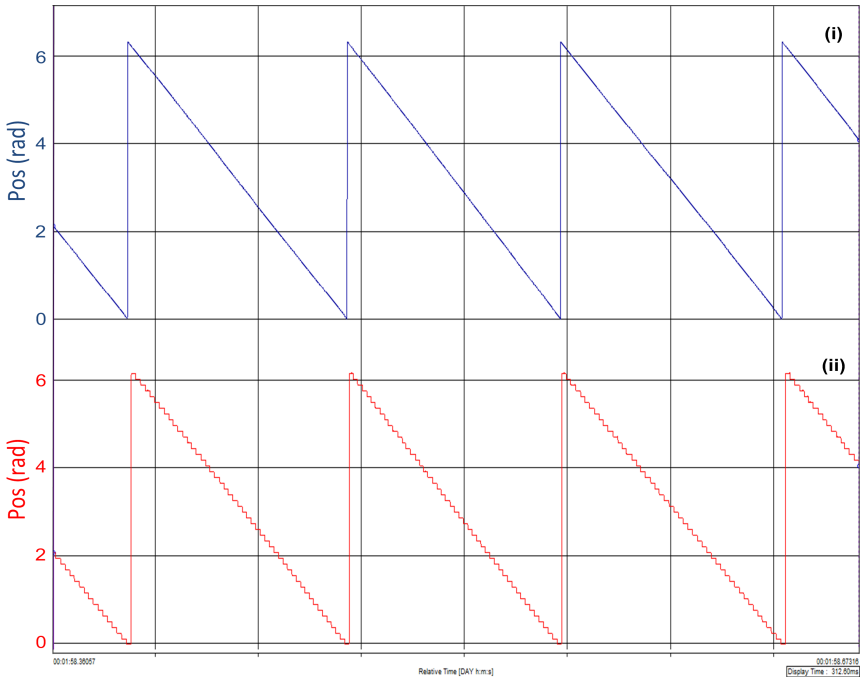

Figure 3.6.4: Rotor position of a, (i) low cost position sensor and (ii) position sensor used in the EPS machine

sensor which will contribute to the additional cost. There is a trade off between computation cost and price of the low cost position sensor. However as compared to the EPS machine position sensor assembly, the development cost of the low cost position sensor housing will still be relatively low since only a two pole magnet is used. The low cost position sensor also has a relatively low PCB board area as compared to the one used for the EPS machine position sensor. Since the EPS machine does not operate at relatively high speeds, the special housing and compensation algorithm might not be a necessity.

The EPS machine is predominantly used in many vehicles, the use of the low cost position sensor can bring about cost savings and smoother operation of the steering wheel. since the low cost position sensor has a relatively higher resolution, the torque ripple will be lower.

3.7 Electric Power Steering Machine Drive

The performance of the low cost position sensor on the EPS machine was also evaluated. Two EPS machines were coupled together, one operated as a motor and the other as a generator. Fig. 3.7.1 shows the experimental set-up of the EPS machine using a low cost position sensor. Figs. 3.7.2 and 3.7.3 shows the experimental and simulation results of the

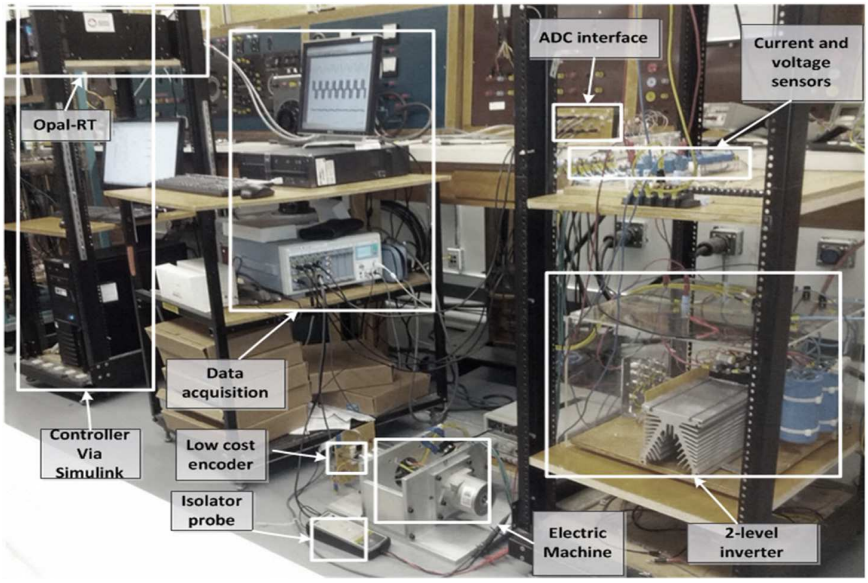

Figure 3.7.1: Experimental set-up of a EPS machine using a low cost position sensor

experiment. The machine was run at a speed of 800 rpm at relatively low torque. The EPS machine has a maximum torque of 4 N.m with peak currents of approximately 50 A,

3.8 Speed Extension Using A Low Cost Position Sensor

The low cost position sensor was also used on a special kind of a SynRM. The SynRM was designed in such a way that the turns ratio could be changed, between either 18 or 25 turns. The SynRM suffers from a small constant power speed range due to poor power factor and saliency ratio. Even though f eld weakening is implemented the constant power speed range is relatively low.

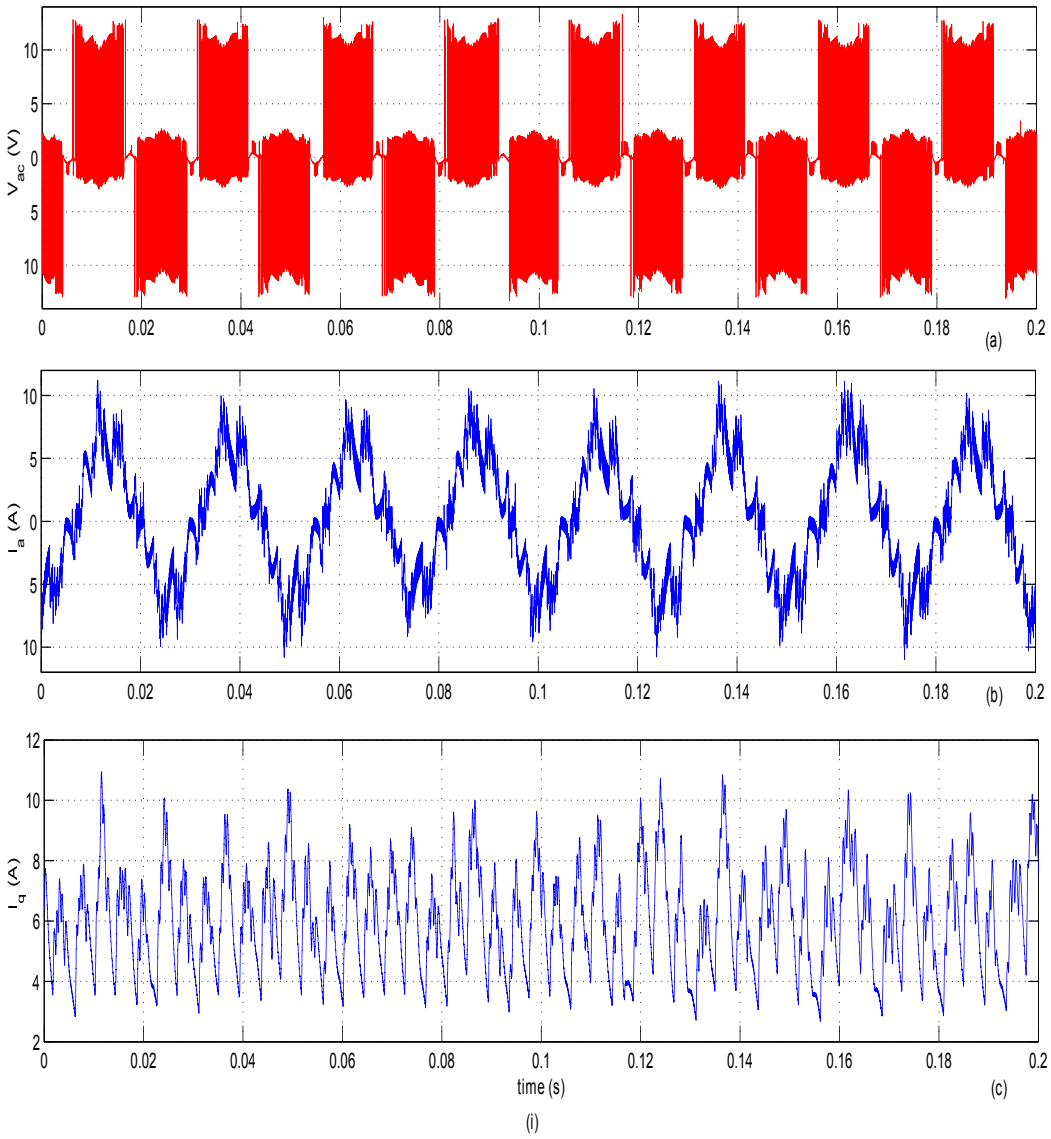

Figure 3.7.2: Experimental results (a) line voltage, (b) line current and (c) q-axis current

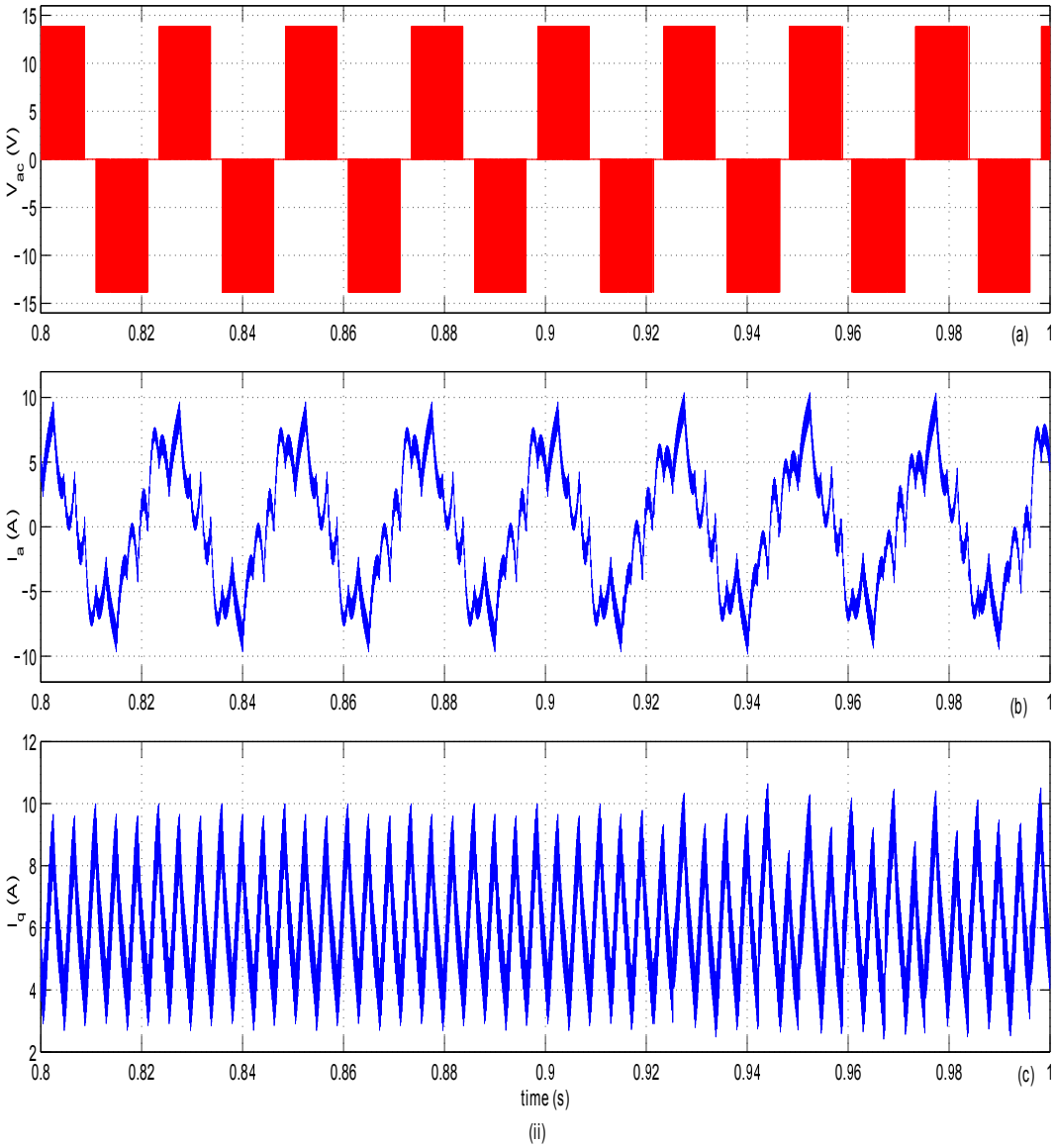

Figure 3.7.3: Simulation results of (a) line voltage, (b) line current and (c) q-axis current

However for this spacial SynRM machine, the machine speed can be extended by reducing the turns ratio whiles maintaining the same power. Fig. 3.8.1 shows the torque and power speed curves. After the base speed at 800 rpm, f eld weakening operation was im-

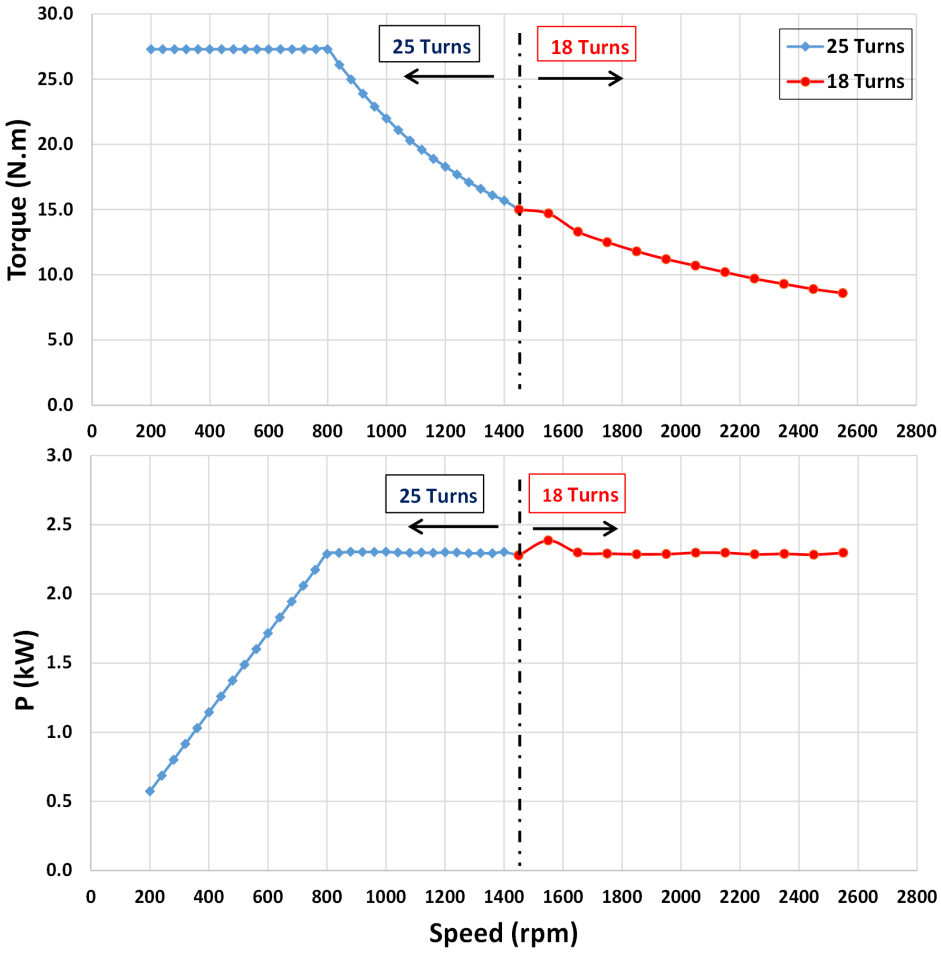

Figure 3.8.1: Torque speed curve at different winding turns

plemented by increasing the current angle (i.e. reducing the d-axis current while q-axis current is increased) until 1450 rpm. The machine was then brought to a stand still and the machines turns ratio changed from 25 to 18 turns. After the change the machine was then run until 1450 rpm with a load torque of 15 N.m (the last condition while the machine was on 25 turns). The current angle was reduced to almost its initial value since the back electro

motive force was lower as a result of the reduction in winding turns. The speed could therefore be further increased to 2250 rpm by increasing the current angle (f eld weakening). All these operations depend on a reliable position sensor and the low cost position sensor was used for the vector control of the special SynRM machine and satisfactory results were achieved.

3.9 Summary

This work has demonstrated the use of a Hall effect low cost high resolution position sensor for traction applications. Torque ripples of less than 9% with current THD of less than 2% were attained. A phase locked loop was used for estimating the rotor speed. Satisfactory results were observed for both shaft rotational directions. When using the current comand for the machine control the low speed was measured at aproximately 12 rpm (1.26 rad/s) with a torque ripple of 14.36% at approximatetly 0.5 N.m. However when using a speed loop the lowest speed could be maintained at approximately 6 rpm (0.63 rad/s) however at much higher torque ripples. The proposed position sensor registered an error less than 1 mechanical degrees when compared with a 12-bit industrial encoder. This work has also shown that the low cost position sensor is a good alternative for the EPS machine due to a relatively simpler algorithm for position information, higher resolution and cost reduction benef ts. Peformance tests of the low cost position sensor on the EPS machine and the special SynRM machine were conducted with satisfactory results.

CHAPTER IV

EFFECT OF THE THREE LEVEL INVERTER SUPPLY ON THE CORE LOSSES OF A SYNCHRONOUS RELUCTANCE MACHINE

4.1 Introduction

The advancement in power electronics have positioned inverters as viable alternative for variable speed ac motor drives. However as compared to sinusoidal power supply, they produce additional harmonics which translates to additional losses in the electrical machine [5]. The introduction of these additional losses is not a new subject, as considerable work has been conducted to investigate the effect that pulse with modulation (PWM) has on core losses on electrical machines [50, 51, 52, 53, 54]. These investigations conf rm the increase in core losses when a non-sinusoidal supply is used.

A two level inverter is the most commonly used power electronic device on which most previous studies have been based. However there has been an increasing demand for a higher dc-bus voltage which has led to a great interest in multi-level converters. A three-level neutral point clamped (3L-NPC) inverter has been identif ed as one of the promising candidates to meet this demand [55, 56]. This is because as compared to the two-level inverter the three level inverter offers lower total harmonic distortion (THD) for both voltage and current. This further implies a reduction in core losses as compared to a two level inverter since the voltage waveform is closer to that of a sine wave.

In [57], it is shown that the two level inverter produced higher d-axis current ripple

which translate to higher core losses as compared to the three level inverter supply. However in that work the core losses were not quantified. Therefore this work for the first time aims to quantify the core loss reduction on the SynRM when supplied from a three and two level inverters. In this work both the two level and three level inverters make use of space vector pulse width modulation (SV-PWM) for the inverter switching pulses.

The behavior of magnetic materials under a sinusoidal supply are complex and their behavior is much more complex from a PWM supply. Their dependence on induction and frequency is non-linear [58, 59, 60, 61]. There are standards for core loss measurements on materials excited from a sinusoidal supply however no standards for non-sinusoidal supply exist. There is academic work on the possibility for standardization of core loss measurements under non-sinusoidal supply [62].

It was shown that the iron losses decrease with increasing switching frequency and that beyond and above 4-5 kHz the iron losses were not affected by the switching frequency [5]. Hence for this study the 2 and 3-level inverters were operated at 10 kHz. The work in this paper will therefore base the core loss measurements on the theory and procedures established by [62].

4.2 Test Bench Description

A Matlab/Simulink software was used to inject the flux density waveform obtained from the SynRM FE model into the stator core. This was conducted by taking a derivative of the flux density waveform which resulted in a voltage waveform. The voltage waveform was then injected into the stator core by the use of real time simulation tool called dSPACE. The excitation voltage waveforms were sent through a DAC to a high bandwidth amplifier

for the test fixture primary winding excitation.

Fig. 4.2.1 shows the stator core used in the SynRM. A current and voltage probe are used to measure the excitation current and the induced voltage on the secondary terminals. The measured parameters are then used in Matlab/Simulink to calculate the instantaneous magnetic field intensity, magnetic flux density and the average power loss. The peak flux density is calculated in real time and used as the reference magnetic quantity in the PWM core loss measurements [62]. Fig. 4.2.2 shows the core loss measurement set-up. The

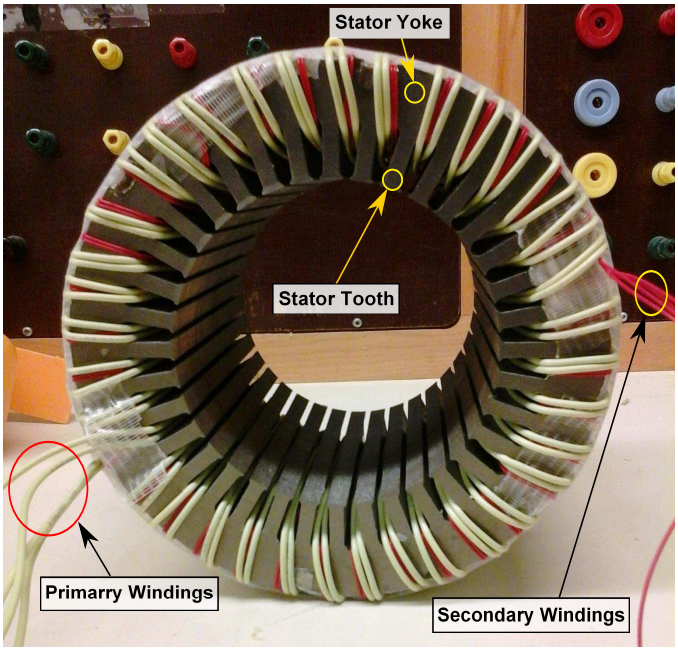

Figure 4.2.1: SynRM stator toroid

stator core is made up of 36 slots and hence the winding is configured for 36 and 72 turns for both the primary and secondary. The 36 turns were used for higher frequency (180 Hz) whereas the 72 turns for low frequencies (30 Hz and 60 Hz). The current was measured on the excited winding (primary) whereas the voltage was measured on the secondary side. A digital power analyzer with current and voltage bandwidth suitable for a PWM supply was used for core loss measurements.

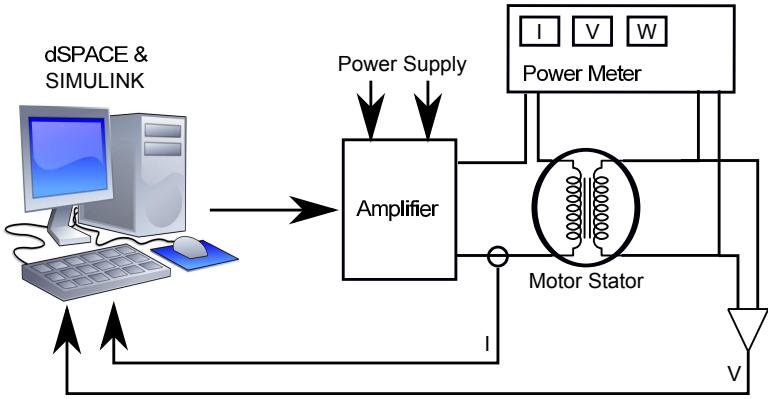

Figure 4.2.2: Core-loss measurement setup

4.3 Core Loss Measurement Methodology and Description

Since this study is concerned with the use on non-sinusoidal supply, there needs to be a correct choice of the magnetic quantities for the core loss measurement. There are two magnetic quantities that can be used, either the peak f ux density of the f rst harmonic or the peak of the f ux density waveform. The f ux density waveforms can be computed through equations (4.3.1)-(4.3.2) [60].

$$B_x = \frac{1}{4NS}\int_0^T |v(t)|\,dt \tag{4.3.1}$$

$$B_{fund} = \frac{V_{fund}}{4.44fNS} = \frac{V_{fund}T}{4.44NS} \tag{4.3.2}$$

V_{ave}, V_{fund}, N, S and T, is the average value of the voltage source, fundamental harmonic RMS voltage source, number of turns, magnetic circuit cross section area and the period of the source voltage waveform respectively. B_x and B_{fund} are the peak f ux density waveform and the peak value of the f rst harmonic of the f ux density waveform respectively.

Based on the work done in [60] and [5] it was observed that the use of the peak of the f rst harmonic f ux density waveform minimizes the measurement errors which occur with the actual PWM waveform. However for this work the peak of the fundamental f ux

density waveform was used since it did not impact the measurements. The peak f ux density is calculated in real time and used as the reference magnetic quantity in the PWM core loss measurements [62].

4.3.1 Two and Three Level Inverter Comparison

The three level inverter generates a voltage waveform closer to that a sinusoidal waveform as compared to the two level inverter. This fact already indicates that a machine under a three level inverter supply will have lower core losses as compared to the two level inverter supply. Fig. 4.3.1 shows the two and three level inverter voltage waveforms.

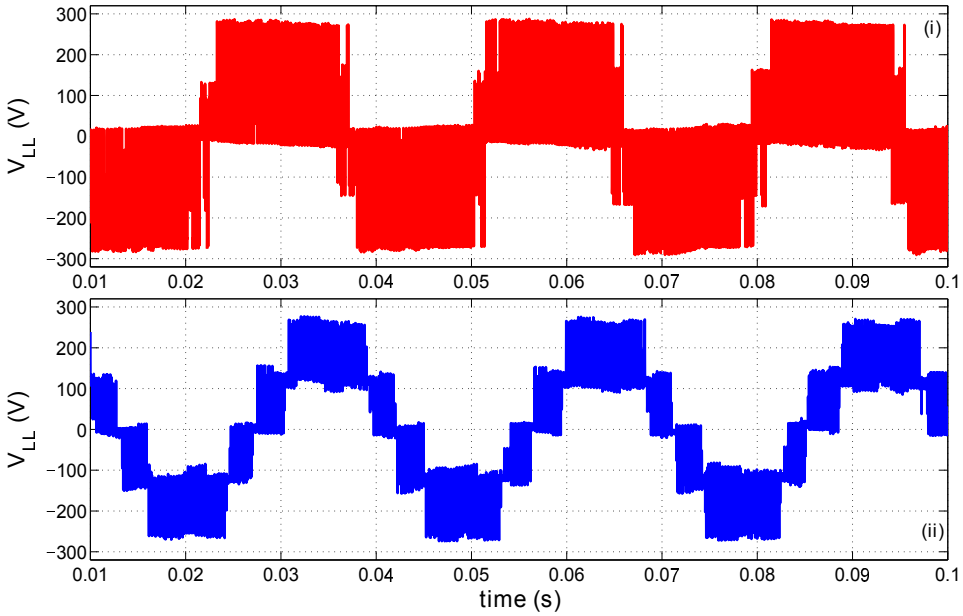

Figure 4.3.1: Inverter line to line voltages, (i) two and (ii) three level inverter waveforms

4.3.2 SynRM Electric Drive

A vector control was used to control the machine via the use of SV-PWM for both the two and three level inverters. Constant angle control strategy was used to meet the load demand. Fig. 4.3.2 shows the control methodology implemented. The fundamental RMS voltages

and currents into the machine were approximately 147 V and 9 A respectively, for both the inverters. The machine was operated at approximately 14 N.m which was used as one of

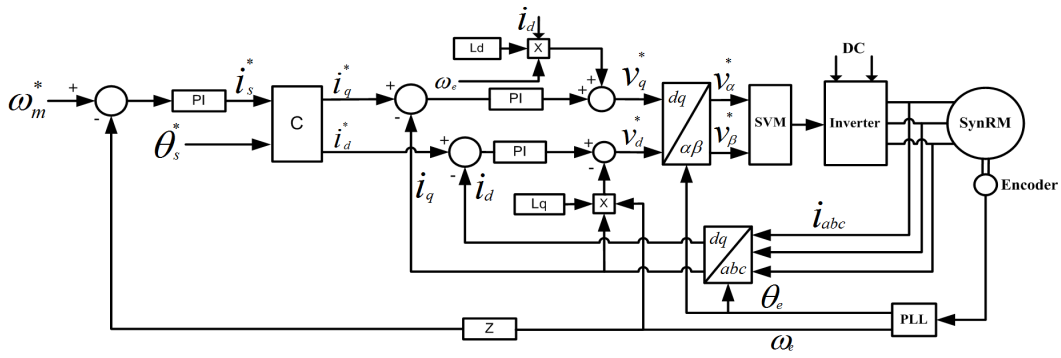

Figure 4.3.2: Control methodology for the SynRM

the parameter indicator for validating the SynRM FE model for the acquisition of the f ux density waveforms (one for the stator yoke and the other for the stator tooth). The switching frequency of the inverters was kept at 10 kHz for the capturing of the current waveforms and Fig. 4.3.3 shows the measured current waveforms. Fig. 4.3.3 shows the measured current

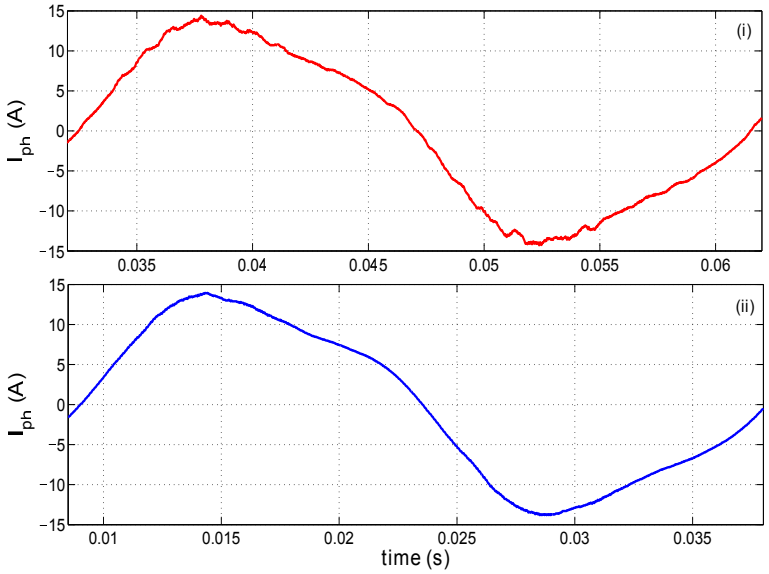

Figure 4.3.3: Current waveforms for, (i) two level and (ii) three level

waveforms for two and three level inverter electric drives. The next section deal with the

acquisition of the flux density waveform as the result of exciting the SynRM finite element (FE) model of the machine with the measured current waveforms from the SynRM electric drive experiment.

4.3.3 SynRM Finite Element Model

A SynRM FE model shown in Fig. 4.3.4 was used to capture the flux density waveforms. This was conducted through feeding the SynRM FE model with the current waveforms obtained from the SynRM electric drive experiments. This flux density waveforms were then injected into the stator core for core loss measurements. Two flux density waveforms were captured, at the stator yoke (Point I) and at the stator tooth (Point II). Fig. 4.3.5 shows the full methodology. Figs. 4.3.6 and 4.3.7 show the flux density waveforms for the stator

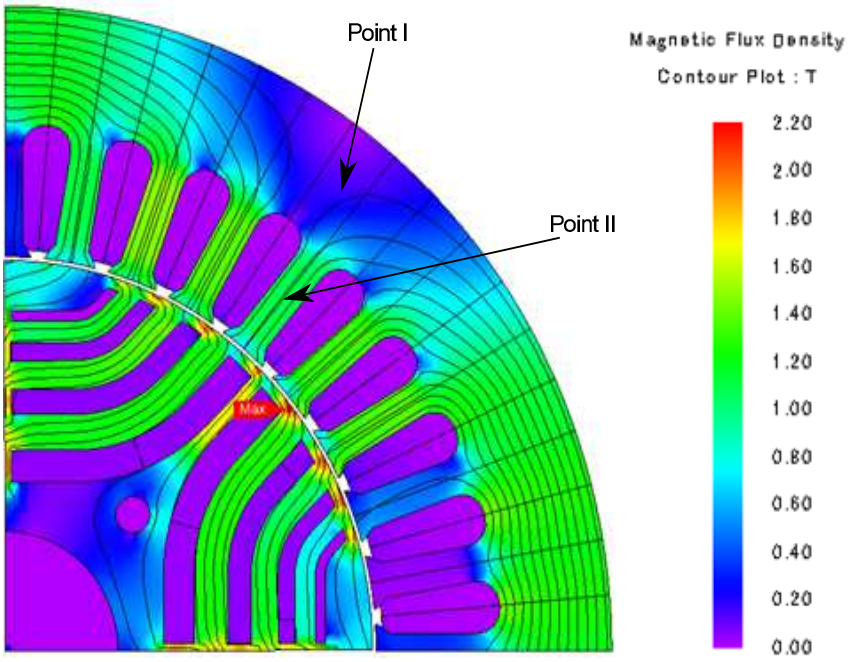

Figure 4.3.4: FE Flux density distribution at full load

tooth and yoke respectively. They are a result of the excitation of the measured current on the FE model. A unique difference on the stator tooth flux density waveforms as a result of

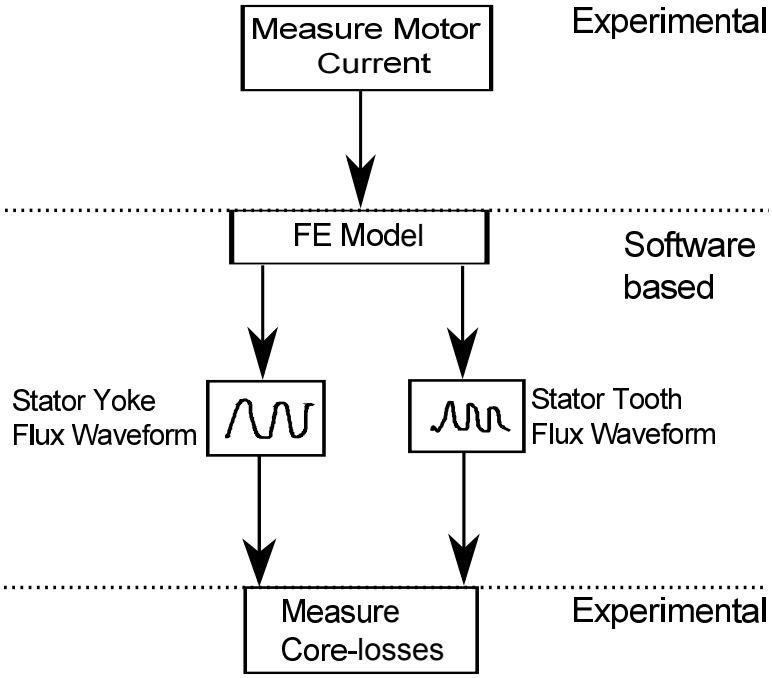

Figure 4.3.5: The core loss measurement procedure

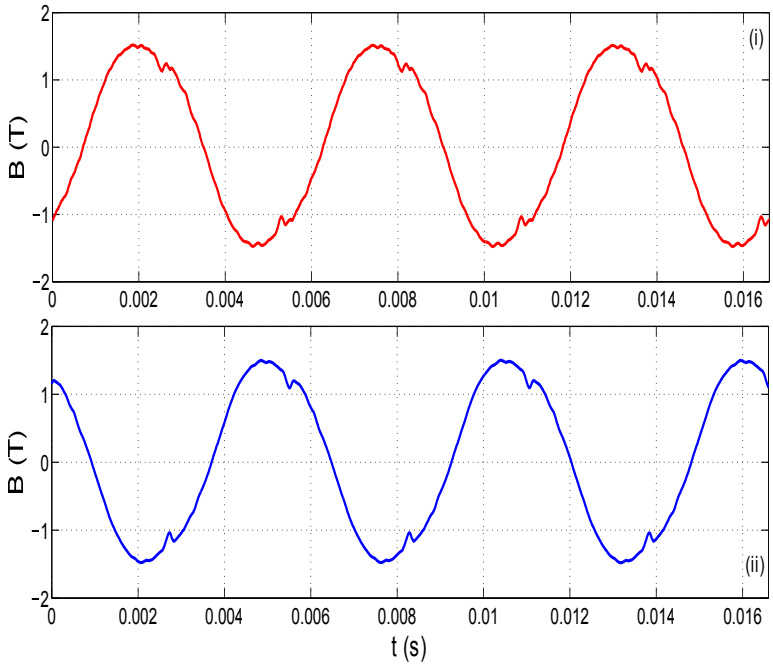

Figure 4.3.6: Stator tooth f ux density waveform, (i) two and (ii) three level inverter supply

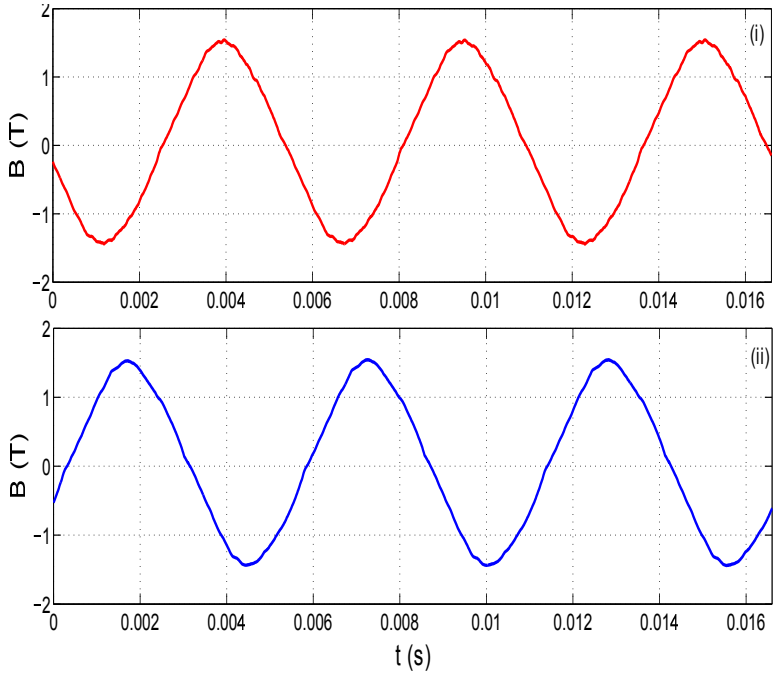

Figure 4.3.7: Stator yoke flux density waveform, (i) two and (ii) three level inverter supply

the two and three level inverter supply was visible. The two level inverter supply generated more ripples on the flux density waveform. However the stator yoke flux density waveform as shown in Fig. 4.3.7(i) and 4.3.7(ii) had a minor difference.

4.4 Core Loss Measurements and Experimental Results

The stator core was excited with a 30 Hz, 60 Hz and 180 Hz flux density waveform. The 30 Hz frequency is the approximate base speed of the machine at full load. The 60 Hz and 180 Hz are within the field weakening region. Frequencies higher than 180 Hz could not be attained due to hardware limitations. Figs. 4.4.1, 4.4.2 and 4.4.3 show the core losses for the stator tooth at 30 Hz, 60 Hz and 180 Hz frequencies respectively. It is clear that in all the three fundamental flux waveform operating frequencies the three level inverter produced lower core-losses. Table 4.4.1 shows the summary of the core-loss difference

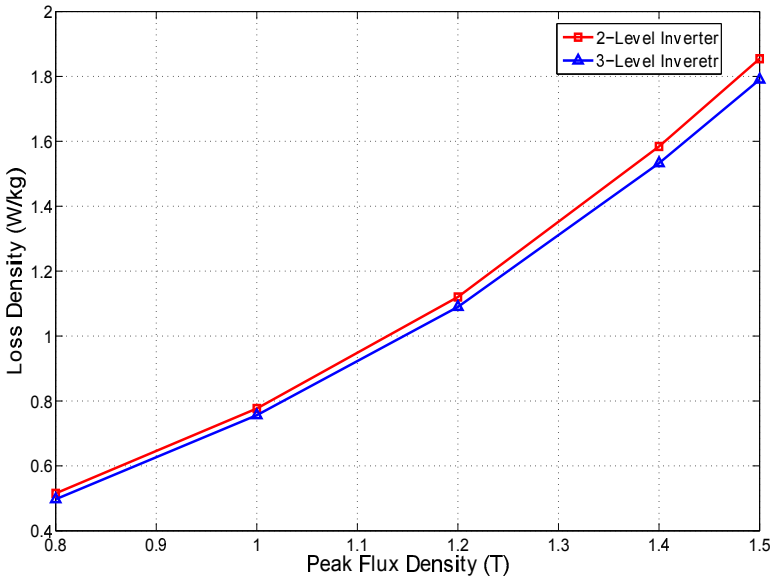

Figure 4.4.1: Stator tooth f ux core loss @ 30 Hz fundamental f ux density frequency

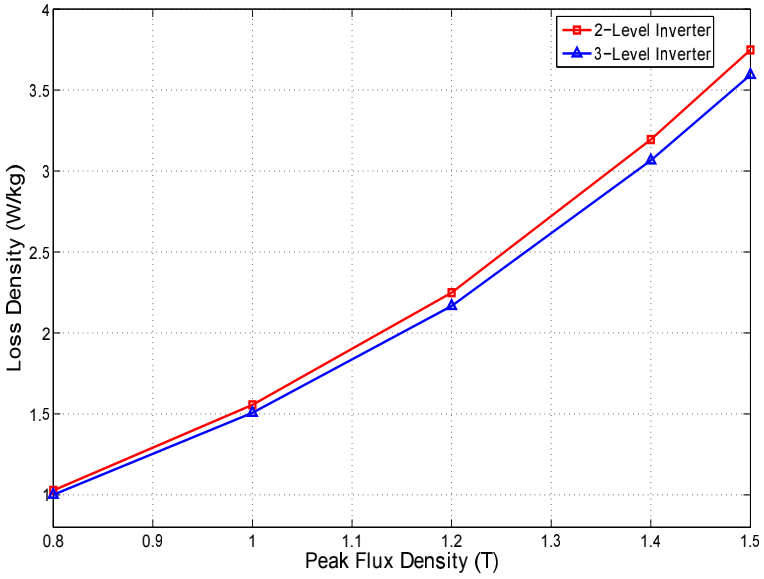

Figure 4.4.2: Stator tooth core loss @ 60 Hz fundamental f ux density frequency

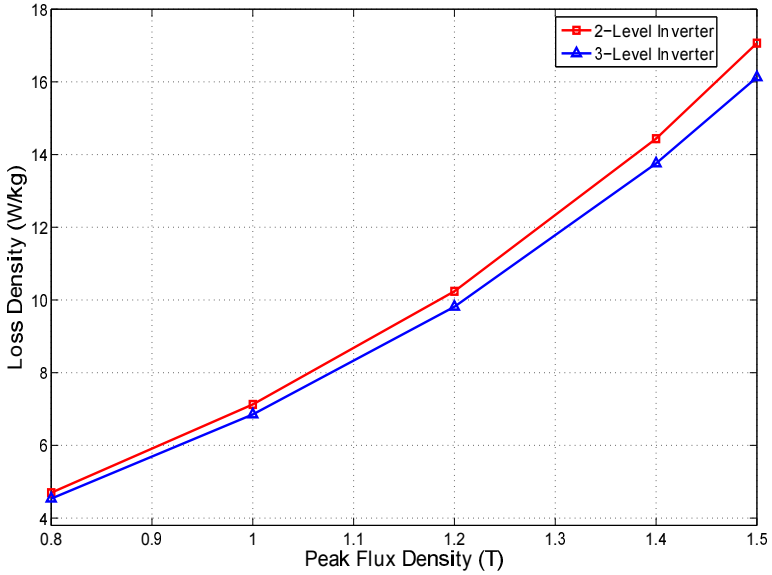

Figure 4.4.3: Stator tooth core loss @ 180 Hz fundamental f ux density frequency

between a two and three level inverter for the respective f ux density waveform at different fundamental frequencies. At 180 Hz the SynRM experienced approximately 5.8% lower core-losses than the two level inverter drive at a f ux density of 1.5 T. Fig. 4.4.4 shows the

Table 4.4.1: Measured stator tooth core-losses at peak f ux density of 1.5 T

Frequency	Core-loss difference (%)
30 Hz	3.6
60 Hz	4.3
180 Hz	5.8

hysteresis loops of the converters at 180 Hz f ux density waveform. The SynRM drive under a two level inverter supply generated higher ripples on the hysteresis loops as compared to the thre level inverter SynRM drive. Figs. 4.4.5, 4.4.6 and 4.4.7 show the core-losses for the stator yoke at 30 Hz, 60 Hz and 180 Hz frequencies respectively. Table 4.4.2 shows the summary of the core-loss difference. The core loss difference at the yoke was less than 2.5% at the f ux density of 1.5 T. The difference in core losses in the stator yoke were

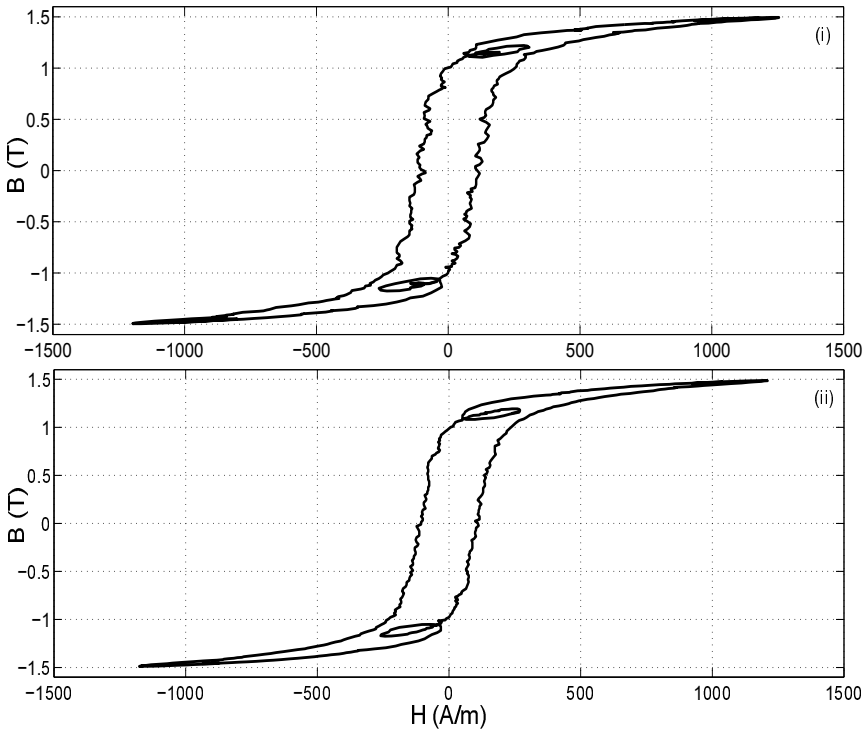

Figure 4.4.4: Stator tooth B-H loops @ 180 Hz fundamental f ux frequency, (i) two level inverter and (ii) three level inverter

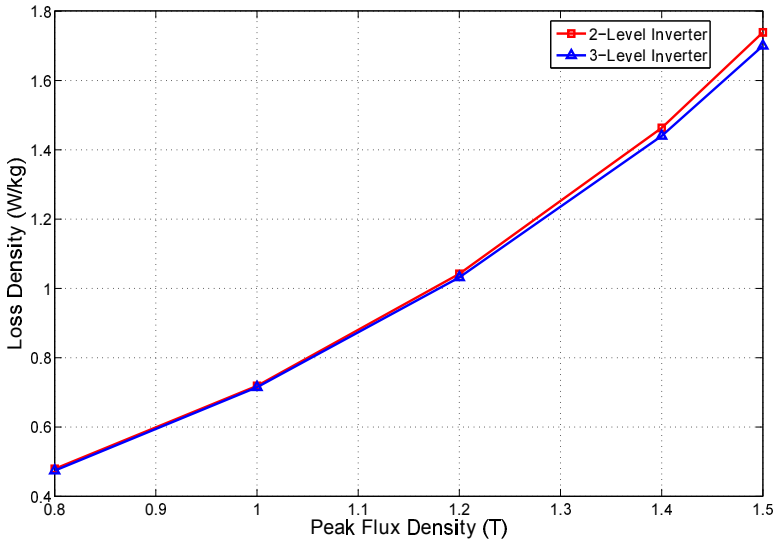

Figure 4.4.5: Stator yoke core loss @ 30 Hz fundamental f ux density frequency

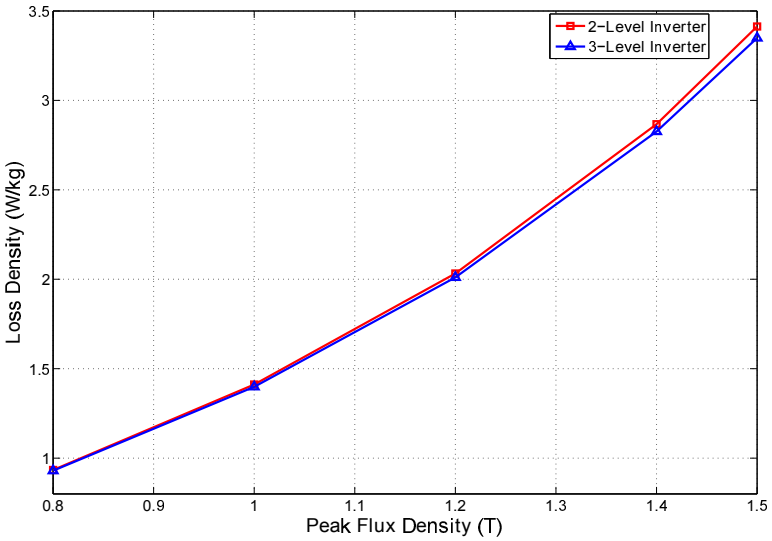

Figure 4.4.6: Stator yoke core loss @ 60 Hz fundamental f ux density frequency

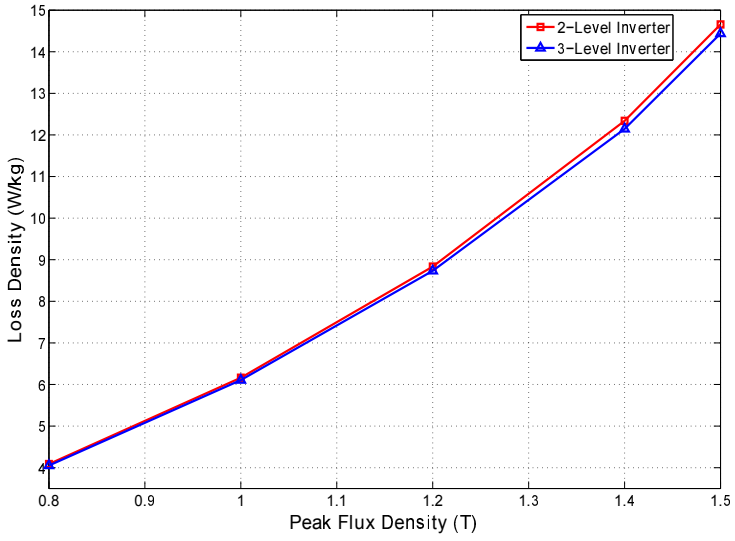

Figure 4.4.7: Stator yoke core loss @ 180 Hz fundamental f ux density frequency

not as signif cant as in the stator tooth. Fig. 4.4.8 shows the yoke B-H loops with a f ux

Table 4.4.2: Measured stator yoke core-losses at peak f ux density of 1.5 T

Frequency	Core-loss difference (%)
30 Hz	2.27
60 Hz	1.92
180 Hz	1.52

density waveform at 180 Hz. There was no signif cant different on the B-H loops in the

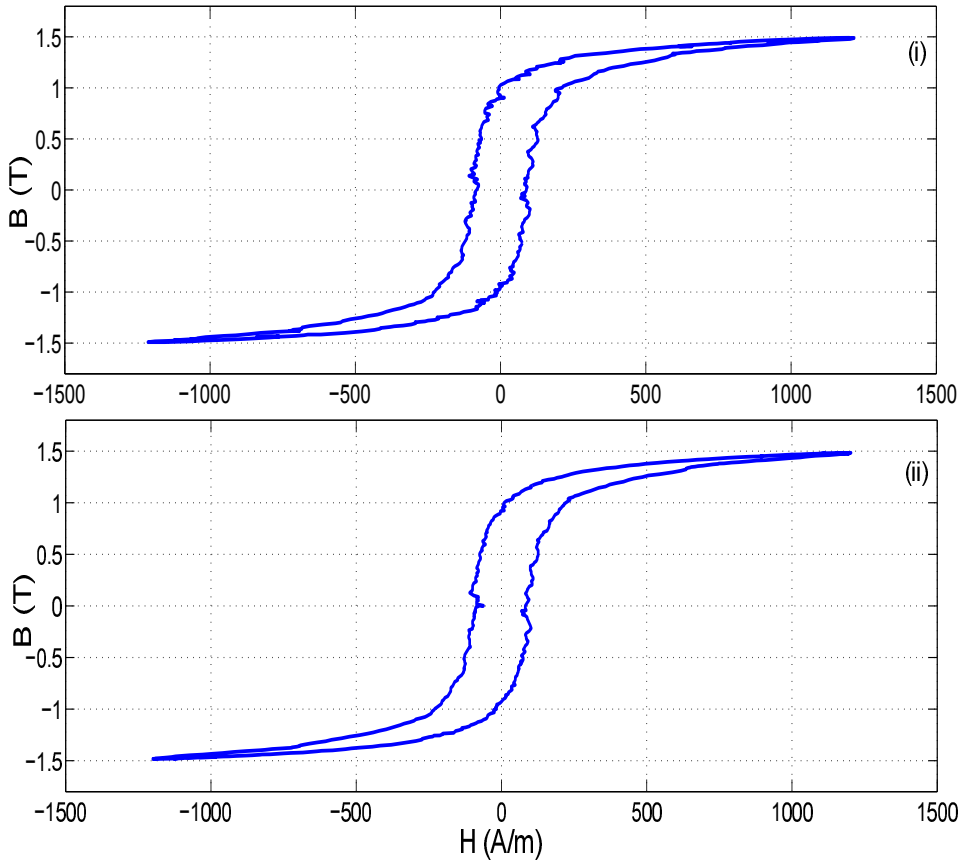

Figure 4.4.8: Stator yoke B-H loops @ 180 Hz fundamental f ux frequency, (i) two level inverter and (ii) three level inverter

stator yoke of the machine. Previous research work indicated that under non-sinusoidal supply the major contributor in core losses is the eddy current losses [63, 64]. This means that a machine run under a three level inverter will generate less heat in the stator tooth

as compared to a two level inverter driven SynRM. This work confirmed the work done in [57], with regards to machine core losses under a three level inverter supplies.

4.5 Direct Supply by Inverters

The SynRM stator core was excited directly from the two and three level inverters. That means the amplifier in Fig.4.2.2 is replaced by either a two or a three level inverter as shown in Fig. 4.5.1. This would allow the effects of the switching frequency on the core losses to be directly analyzed. The two level inverter is generally operated at a relatively higher

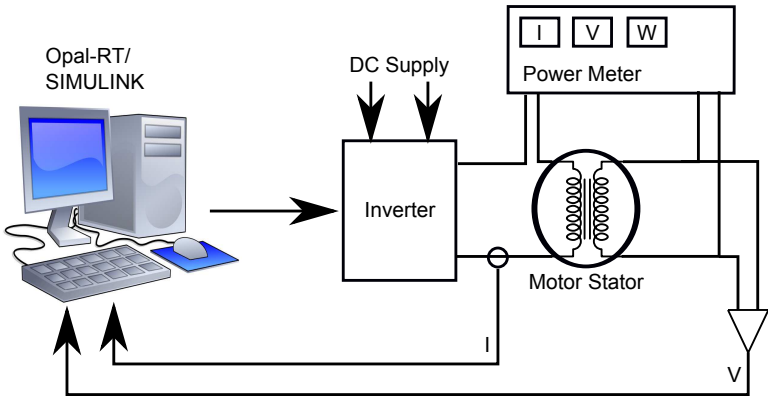

Figure 4.5.1: Core-loss measurement setup

switching frequency to reduce the total harmonic distortion of the current. However this is not the case for a three level inverter. The three level inverter can be operated at lower switching frequencies and yet attain low THD. Hence for this work, the two level inverter was operated at 10 kHz and the three level inverter at 5 kHz. From Table 4.5.1, it can be seen that the stator core under a three level inverter excitation had relatively lower core losses. Table 4.5.2 shows the core loss difference at a fundamental frequency of 180 Hz. The core loss difference on the stator toroid under the two and three level inverter supply was more significant at higher fundamental operating frequencies. Fig. 4.5.3 is the current

Table 4.5.1: 2L-INV and 3L-INV operated at 10 kHz and 5 kHz respectively at 60 Hz fundamental frequency

B (V.s)	2L-INV (Watt/kg)	3L-INV (Watt/kg)	Difference (%)
0.8	0.95	0.92	2.94
1	1.43	1.38	4.11
1.2	2.08	2	4.25
1.4	2.81	2.69	4.11

Table 4.5.2: 2L-INV and 3L-INV operated at 10 kHz and 5 kHz respectively at 180 Hz fundamental frequency

B (V.s)	2L-INV (Watt/kg)	3L-INV (Watt/kg)	Difference (%)
0.8	4.47	4.13	8.30
1	6.83	6.26	9.10
1.2	9.78	8.91	9.68
1.4	13.59	12.31	10.36

waveform of the two and three level inverter. It can seen that the two level inverter produced relatively higher current ripples than the three level inverter. This is because the two level inverter has higher rate of change of voltage (dv/dt) as compared to the three level inverter. The three level inverter does not switch from zero to the dc link voltage due to the intermediate zero state voltages. Fig. 4.5.2 shows the B-H loops of the two and three level inverter operated at 10 kHz and 5 kHz respectively. The higher ripples in the current also means that the f eld intensity will have the same ripples and hence the B-H loop for the two level inverter had higher ripples. This is the cause of the difference in the core loss between a two and three level inverter supply. This work goes to show that, by operating the three level inverter at a lower switching frequency, there would still be core loss reduction benef ts while also reducing the switching losses of the converter.

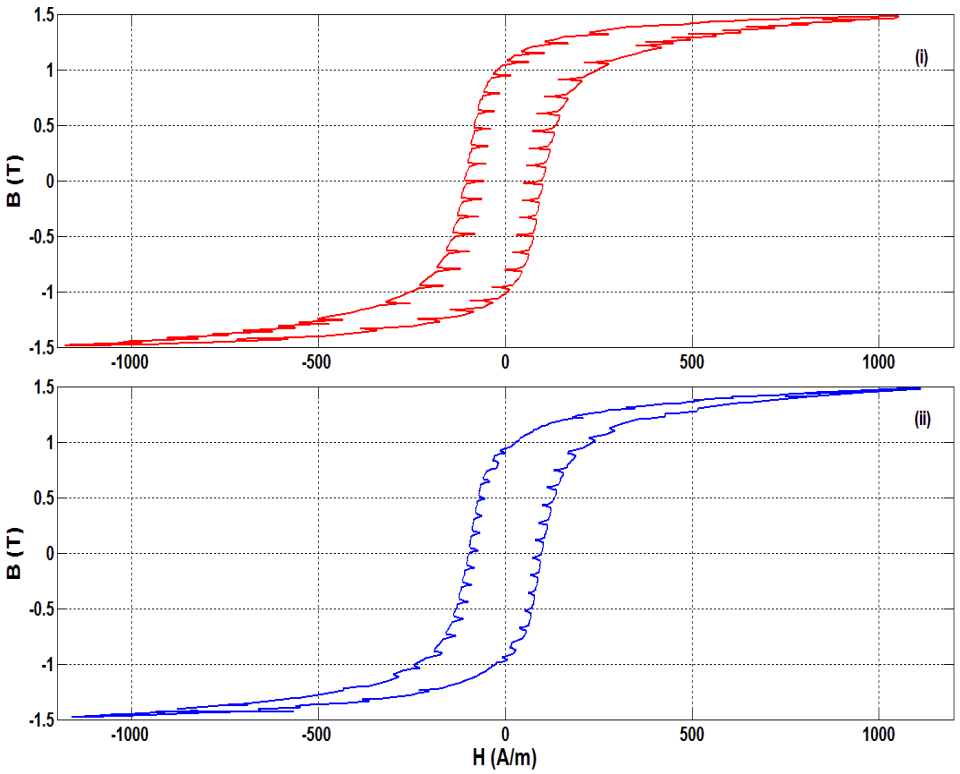

Figure 4.5.2: B-H loops @ 180 Hz fundamental f ux frequency, (i) two level inverter and (ii) three level inverter

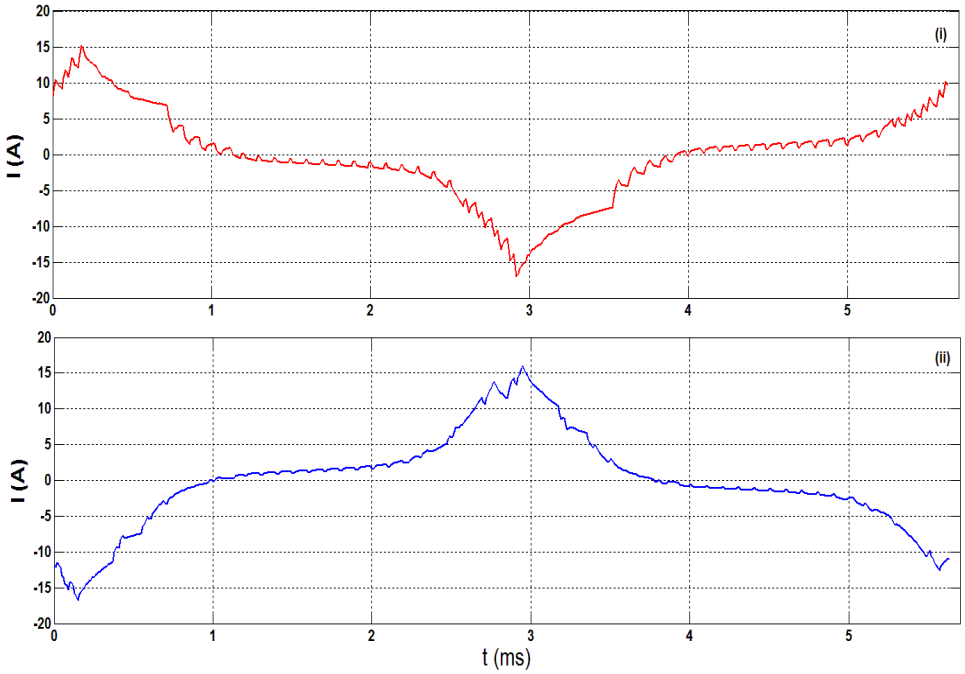

Figure 4.5.3: Current waveforms from a, (i) two and (ii) three level inverter supply

4.6 Summary

In this chapter the core losses on a SynRM while operated from a two or a three level inverter supply were compared. Finite element software was used to capture the flux density waveform in the stator tooth and yoke. The stator core was excited with a maximum peak flux density of 1.5 T at 30 Hz, 60 Hz and 180 Hz respectively. The experiments show that the SynRM under a three level inverter supply does not only benefit from good quality power (lower THD) but also a reduction in core losses. The core losses on the stator tooth were lower as compared to the stator yoke. The stator tooth had approximately 6% lower core losses whereas the stator yoke below 3% at 180 Hz. This is beneficial since the stator yoke is easier to cool than the stator tooth. Additionaly the use of a three level inverter will contribute towards reducing the burden of the cooling system on the electric drive. When the converters were directly connected to the stator toroid core, the three level inverter supplied toroid registered lower core losses with a core loss difference of approximately 10%.

CHAPTER V

CONTROL STRATEGY OF A VARIABLE FLUX MACHINE USING ALNICO MAGNETS

5.1 Introduction

Permanent magnet synchronous machines have become more popular due to their high efficiency and high power density. The high efficiency of the PMSM is due to no excitation winding since the air gap magnetic flux is provided by the permanent magnets (PM). Hence these machines have attracted a variety of applications, such as actuators, servo drives and washing machines. The electric vehicle is another potential application for the PMSM mainly due to its high efficiency. For the electric vehicle efficiency is one of the top priorities due to the limited energy supply.

Wide speed operation is required for electrical vehicles (EVs). However due to restrictions on the dc link voltage and inverter power rating, the maximum speed is limited. For a permanent magnet synchronous machine (PMSM) where rare earth magnets are used, a flux weakening control is commonly used to extend the speed range. However this results in additional energy loss due to the additional armature current required for the flux weakening operation. Hence for a traditional PMSM to extend the speed beyond the base speed, flux weakening current is required. For a variable flux machine the flux linkage of the PMs can be varied by the use of a demagnetization current pulse. Hence for vehicle applications were at low speeds high torque is required, high flux linkage will be necessary to guarantee

the high torque demand. However at high speeds and low torque demand the PMs flux linkage can be reduced.

The variable flux machine (FVM) (so-called memory motor) employs low coercive-force magnets to obtain variable PMs flux characteristics. This will result in the reduction of the flux weakening current and hence reduced machine losses [65]. The concept of memory is due to the nature of the aluminum-nickel-cobalt (AlNiCo) permanent magnets (PMs) used in this machine. They can be magnetized on-line to various magnetization levels and hence be memorized automatically [66]. These machines have been investigated in several works [67, 68, 46, 66, 69]. The magnetization of PMs can be varied by a short current pulse in the d-axis, this will result in a change in the magnetization state and vary the air gap flux density associated with the magnets. There are different kinds of excitation methods, they can be categorized into either alternating current by the use of the stator winding [67] or direct current by the use of a separate dc coil [66].

There is a number of disadvantages on the use of the dc excitation method: 1) there is a need for an extra winding for excitation, 2) the machine structure becomes complicated due to two stator layers, one for the armature and the other for the excitation winding as well as the PMs [66], 3) an extra converter is required for the PMs excitation. However the advantage is that the PMs excitation is decoupled from the armature currents hence immunity from armature reaction [66].

The major challenges are: 1) the overrating of the converter to allow for the PMs magnetization current, 2) the demagnetization of the AlNiCo PMs due to armature current reaction as a result of their very low coercive force and 3) the torque ripple that results due to the PMs excitation process [70]. Hence to resolve problem (2), other PMs have been

used such as Sm-Co, which have a high coercive force but still less than that of the rare earth PMs. Due to their high coercive force a higher magnetization current is required, this adds to the problem related in problem number (1). Another proposed solution when using the AlNiCo PMs for a VFM is the use of the separate dc coil for magnetization [66]. However this contributes to additional costs of the electric drive. This work proposes a control strategy for the VF-IPMSM that uses AlNiCo magnets witch are magnetized from the stator winding. Included in the work is also the performance of the core losses of the VFM with AlNiCo magnets.

5.2 Characteristics of the AlNiCo Magnets

The operating point of the magnet occurs at the intersection between the air gap line with the demagnetization curve of the magnet which is at point A in Fig. 5.2.1. As compared to the rare earth magnets the AlNiCo magnets can retain a limited intrinsic f eld when exposed to an external demagnetization f eld. In Fig. 5.2.1, the AlNiCo magnet is f rstly operated at point A. If a an external demagnetization f eld is applied the operating point will shift to point B beyond the knee point. Once the magnet shifts beyond the knee point the intrinsic magnetic f ux density will be reduced by ΔB_i. Once the external demagnetization f eld is removed the magnet will move along the line parallel to the original demagnetization curve to point C at a new remnant f ux density of $B_r - \Delta B_i$. Fig. 5.2.2 shows an illustration of the simplif ed B-H loop of the AlNiCo magnet. If the external demagnetization f eld reached H_d, the magnet would be completely demagnetized. This is the magnetic f eld intensity that is just a little above the coercive force of the AlNiCo magnets. The AlNiCo magnets have a relatively low coercive for as compared to other magnet materials. A magnetizing

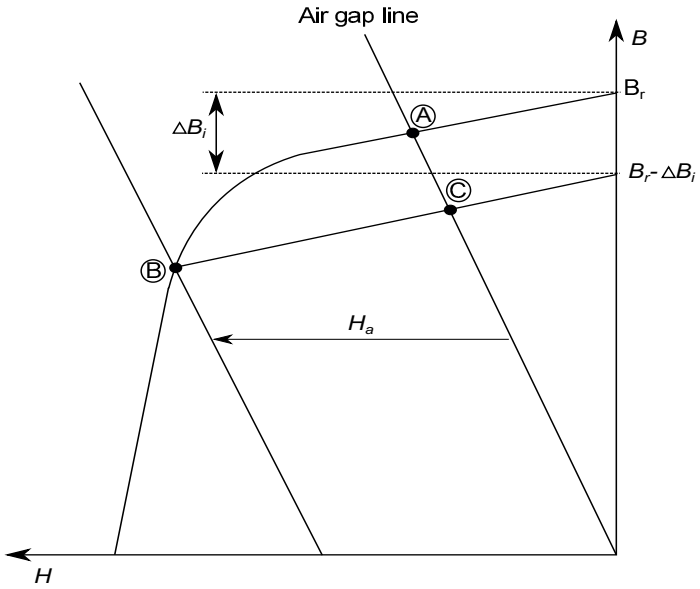

Figure 5.2.1: AlNiCo magnets under demagnetization f led

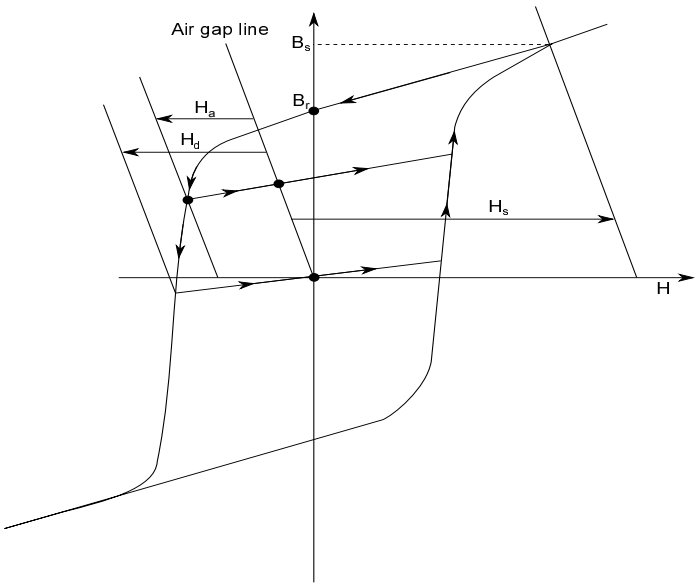

Figure 5.2.2: Linearized B-H loop of of a AlNiCo magnets

f eld H_s is applied in order to re-magnetize the magnet. The H_s f eld intensity is applied in such a way that the magnet operating point has to shift beyond the hysteresis loop knee in the f rst or third quadrant until a saturation f ux density of B_s. When the magnet f eld is released the magnet will recoil to the air gap line along the demagnetization curve.

5.3 Properties of The Variable Flux Machine (VFM)

There are other low coercive force PMs such as a samarium-cobalt (Sm-Co) which were used for the VFM [71]. However they have a higher coercive force as compared to the AlNiCo PMs and they cost more than AlNiCo PMs. By using AlNiCo PMs the converter size will be smaller as compared to a machine that uses Sm-Co PMs since the current requirements for magnetization are lower [72]. The AlNiCo PMs also have high resistance to heat and have good mechanical features. Fig. 5.3.1 shows the rotor geometry design and the prototyped rotor of the variable f ux machine with AlNiCo magnets.

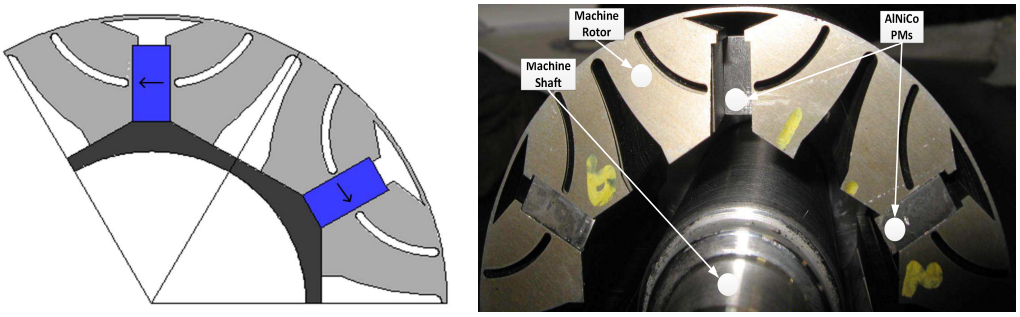

(a) (b)

Figure 5.3.1: Rotor geometry of the variable f ux machine, (a) and the prototyped rotor, (b)

5.3.1 Off-line Tests

By injecting a current pulse in the d-axis the magnets can be demagnetized or magnetized. For off-line de or re-magnetization the VFM was aligned with the d-axis while phase B and

C were shorted as shown in Fig. 5.3.2. The machine was then exposed to several positive d-axis current pulses at peak increments of approximately 5 A. The magnet was regarded

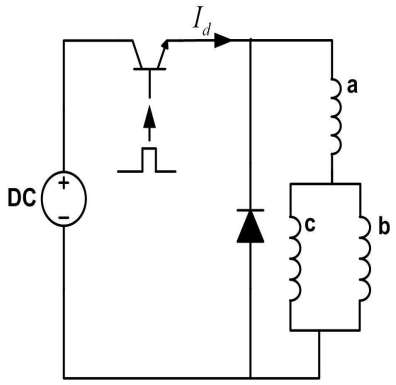

Figure 5.3.2: Off-line magnetization using the d-axis current pulse

as fully magnetized at a peak pulse current of 42 A. Fig. 5.3.3 shows the back EMF and the magnet flux as the peak d-axis current pulse is increased. The maximum magnet flux was measured to be 0.52 V.s. However there was a difference of 3.8% in the magnet flux between a magnetization pulse current of 42 A and 30 A. Hence in favour of reducing the convereter size 30 A was the best option. For the de-magnetization of the PMs a negative d-axis current was applied by connecting Phase A of the machine to the negative voltage supply and phase B and C to the positive terminal as illustrated in Fig. 5.3.4. Fig. 5.3.5 shows the demagnetization of the magnets. Finite element analysis (FEA) of the VFM was based on the AlNiCo flux linkage of 0.56 V.s based on a 35 A d-axis current pulse. However only 0.52 V.s could be reached, this can be attributed to the reduction of the windings on the prototyped machine and the imperfections of the dimensions on the actual AlNiCo permanent magnets used in the prototyped machine. The experimental analysis shows that the magnets were at near zero magnetic flux when exposed to a negative peak pulse current of -10.8 A.

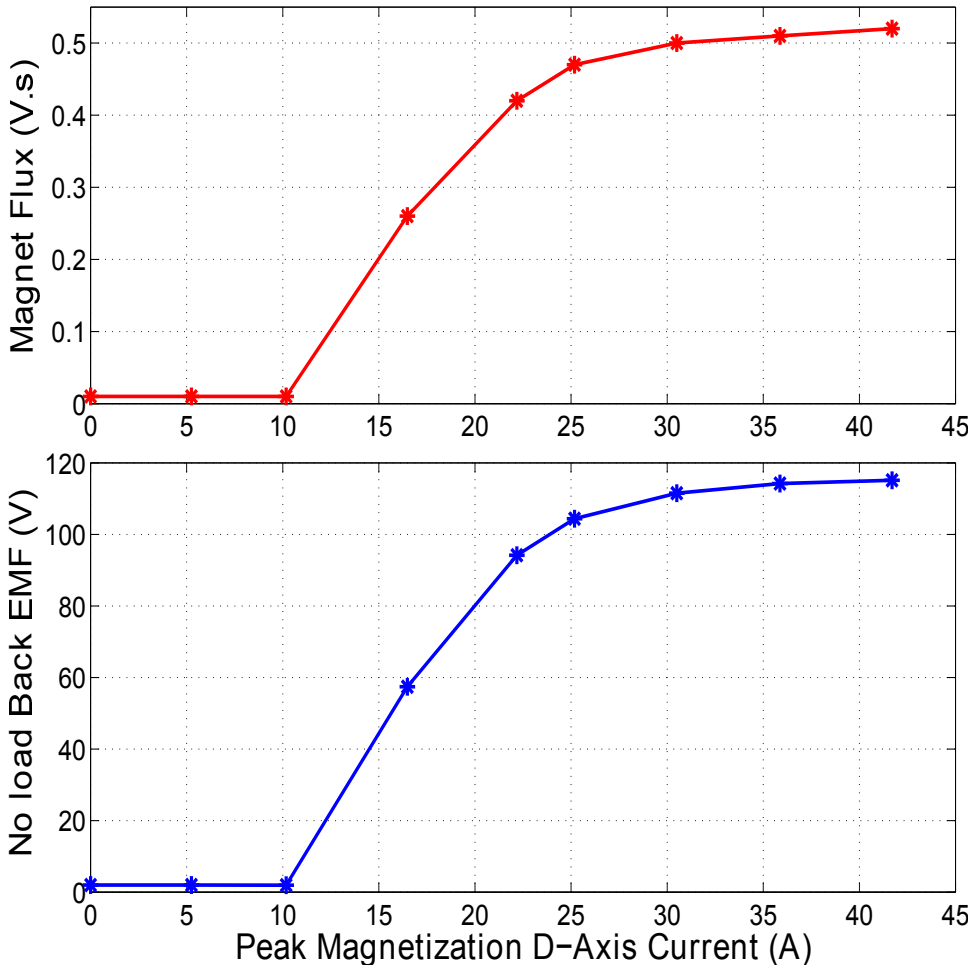

Figure 5.3.3: Magnetization using the d-axis current pulse, shows the the magnet f ux (top) and the back EMF (bottom)

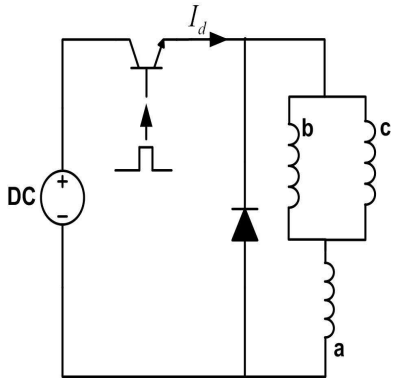

Figure 5.3.4: Off-line demagnetization using the d-axis current pulse

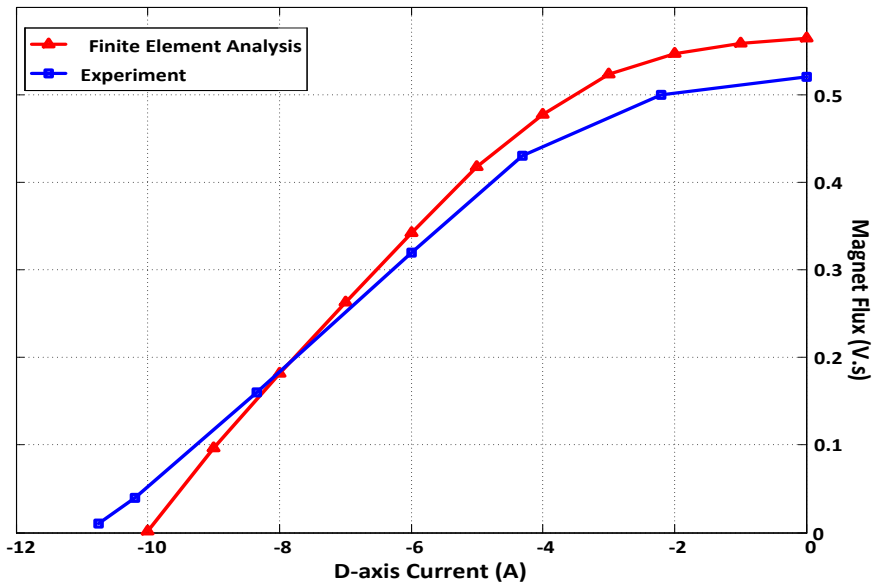

Figure 5.3.5: Demagnetization using the d-axis current pulse

5.3.2 On-line Test

The machine was initially operated with a magnet f ux near zero while the d-axis current was kept at zero at no load. At no load conditions an electric torque is required to overcome the f ction and windage of the machine and that of the coupled dc generator. A higher q-axis current develops due to low magnet f ux of the machine. Fig. 5.3.6 shows that after magnetization the q-axis current drops. Fig. 5.3.7 shows that q-axis current drops even further at higher magnetization current. This is in agreement with equation (5.3.1), for the electric torque depends on both q-axis current and the magnet f ux. The q-axis current is in direct proportion with the input armature current when the d-axis current is zero.The magnetization current was commanded at a speed of 300 rpm. The machine speed was ramped from 290 rpm to 340 rpm and the magnetization pulse was set to occur at 300 rpm. Figs. 5.3.6 and 5.3.7 shows the magnetization process while the machine was exposed to a

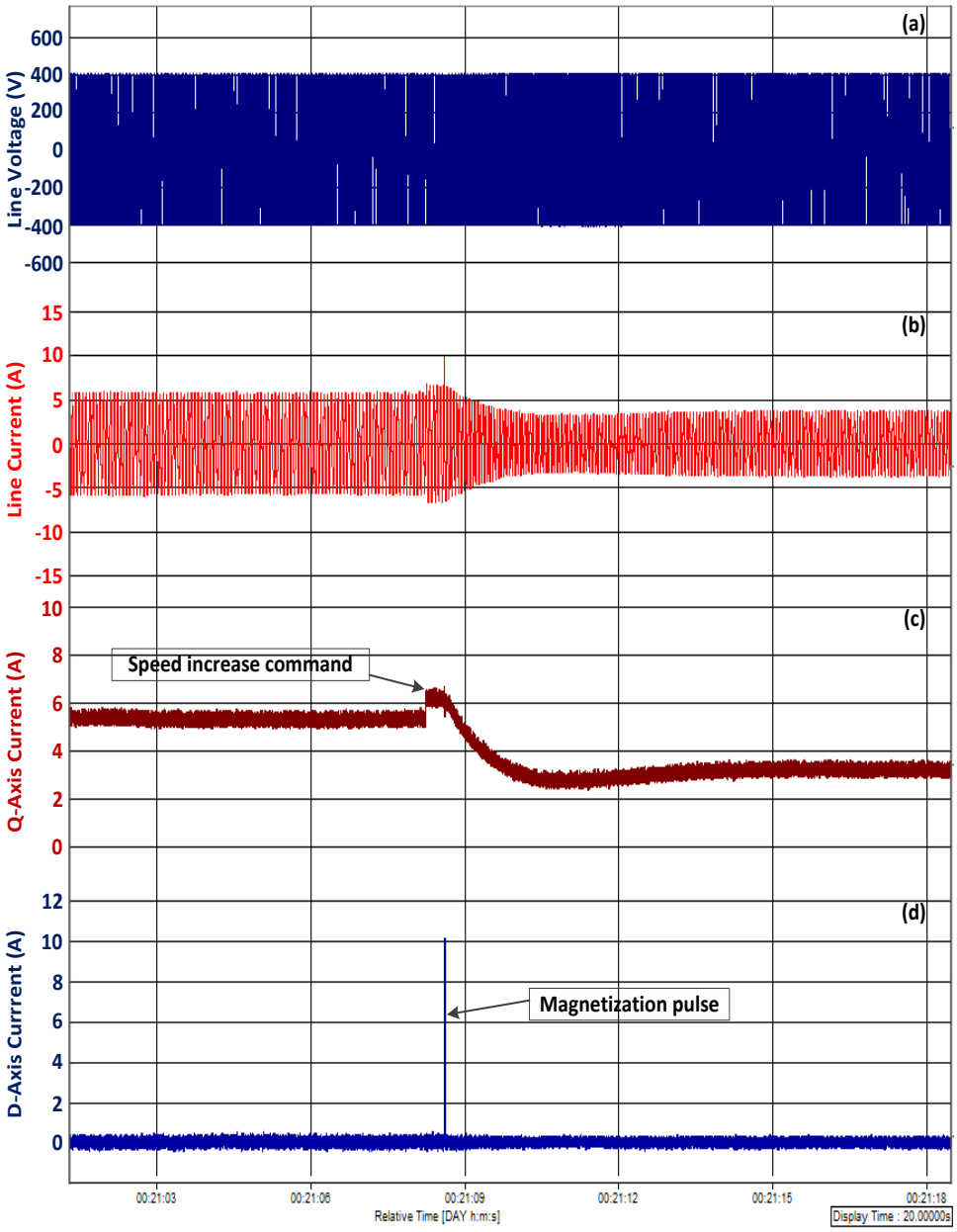

Figure 5.3.6: Injecting a magnetization d-axis current of approximately of 10 A

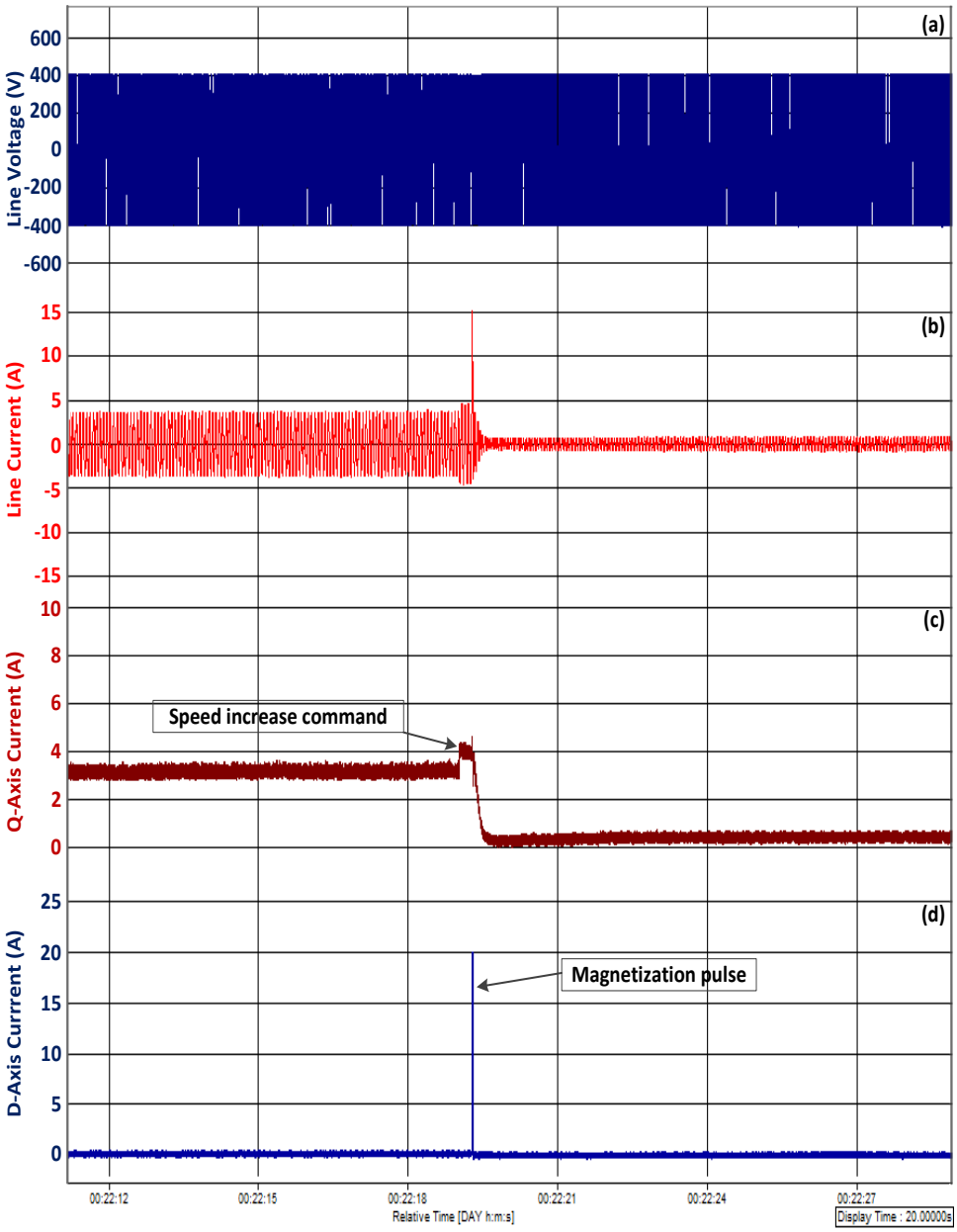

Figure 5.3.7: Injecting a magnetization d-axis current of approximately 20 A

d-axis current pulse of 10 A and 20 A respectively.

$$T_e = \frac{3P}{2}(\lambda_{af} i_q) \tag{5.3.1}$$

P, i_q and λ_{af} is the number of pole pairs, q-axis current and PMs flux linkage. Since the machine had a torque ripple of approximately 20%, at no load, it was difficult to capture the torque reading. For a d-axis current pulse of 10 A and by the use of Fig. 5.3.3 the flux increased to approximatetly 0.03 V.s and the measured q-axis curret dropped to 3.2 A. By the use of equation (5.3.1) the torque was approximatetly 0.43 N.m at 340 rpm. After a d-axis current pulse of 20 A the flux jumped to 0.38 V.s. Since the load torque remained the same at 0.43 Nm, at the speed of 340 rpm the q-axis current was clculated to be 0.25 A based on equation 5.3.1. Fig. 5.3.7 shows that the calculated current and the measured current are in agreement.

In Figs. 5.3.6 and 5.3.7 it is also demonstrated that the copper losses can be reduced by operating the machine at higher magnet flux at low speeds and high torque regions. This means that the efficiency of the machine can be improved depending on the operating region.

The other experiment that was conducted was the reaction of magnet flux as the q-axis current was increased while the d-axis current was kept at approximately zero current. Fig. 5.3.8 shows the plot of the magnet flux (Fig. 5.3.8 (a)) and torque (Fig. 5.3.8 (b)) as the q-axis current is increased. Fig. 5.3.8 (a) and (b) shows that the magnet flux is enhanced by the q-axis current.

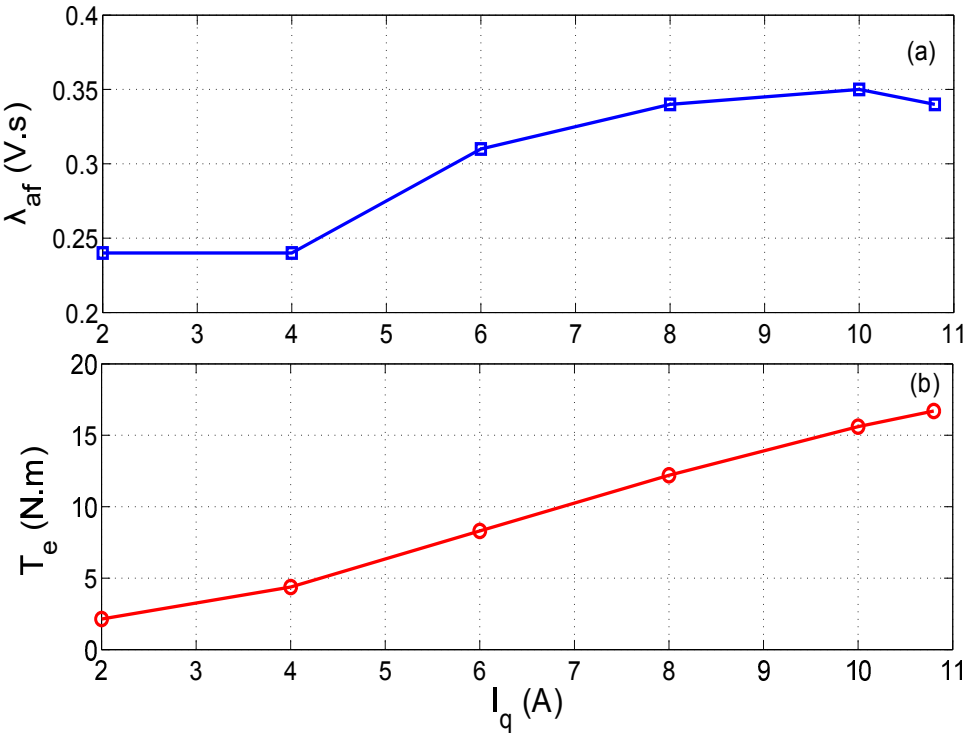

Figure 5.3.8: Magnet f ux with increasing q-axis current

5.3.3 Core Loss Performance

Core losses in electrical machines account for a large portion of the total loss and the losses are even higher for PM and switched reluctance (SR) machines. During the machine design stage, the design optimization requires accurate quantization of the core to improve the machine eff ciency. In traction application where the machine eff ciency contributes to the vehicle maximum travel range due to the limited energy source, improving the machine eff ciency is desirable. This work therefore can be used for the development of a core losses model for the estimation of the core loss in the variable f ux machine with AlNiCo magnets.

Test Set-Up and Experimental Procedure

The VFM was run as a motor only for the magnet f ux manipulation through the injection of the temporary d-axis current pulse. Five case studies were conducted based on the state

of the magnet flux which was varied from approximately 0% to 100% in 25% intervals. The magnet flux was initially reduced to approximately 0.009 V.s (1.7%). The VFM was run as a unloaded generator from 200 rpm to 2000 rpm in 200 rpm speed intervals. In each speed interval the input power of the dc machine was measured and was used for the core loss measurements.

When the magnet flux state is approximately zero the measured input power from 200 rpm to 2000 rpm is approximately the windage and friction of the combined machines and the copper losses of the dc machine. These losses were then removed from the measured input power when the magnet flux state was varied from 25% to 100%. Since the dc machine was run without loading the VFM and the input current was relatively small with little variation in the armature resistance of the dc machine. To account for the losses due to the armature resistance variation the initial and final values of the armature resistance were measured in each case study and there was a maximum variation of approximately 0.15 Ω and the maximum current reached was 3.4 A. Therefore the maximum deviation error due to copper losses are approximately 1.7 W. The followsing section describes the test results.

Test Results

Fig. 5.3.9 shows the measured core loss of the variable flux machine at different magnet flux states. The core losses increased with increasing magnet flux state and the motor speed.

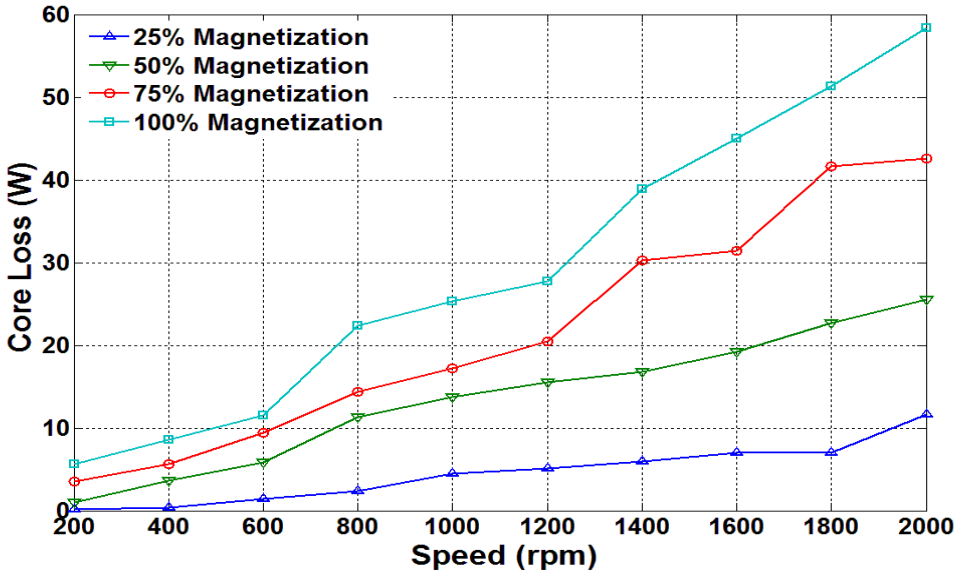

Figure 5.3.9: Measured core loss of a variable f ux machine with AlNiCo magnets

5.4 Electrical and Control Limits

There are two electrical limits in the PMSM, the current and voltage limits imposed by the limited DC bus voltage (V_{smax}) and the motor rated current (I_{smax}). Equation (5.4.1) and (5.4.2) describes the voltage and current limits.

$$I_s = \sqrt{{I_d}^2 + {I_q}^2} \leq I_{smax} \tag{5.4.1}$$

$$V_s = \sqrt{{V_d}^2 + {V_q}^2} \leq V_{smax} \tag{5.4.2}$$

Equations (5.4.3) to (5.4.4) are the equations of the PMSM model in steady state while the ohmic drops are neglected.

$$v_q = \omega_e \left[L_d I_d + \lambda_{af} \right] \tag{5.4.3}$$

$$v_d = -\omega_e L_q I_q \tag{5.4.4}$$

where, ω_e is the angular electrical speed and λ_{af} is the PM flux linkage. Equation (5.4.5) describes the electromagnetic torque while P is the number of pole pairs.

$$T_e = \frac{3}{2} P \left[\lambda_{af} I_q + (L_d - L_q) I_d I_q\right] \tag{5.4.5}$$

By substituting equation (5.4.3) and (5.4.4) into equation (5.4.1) and (5.4.2) will result in voltage limit as speed-dependent ellipses with I_d and I_q as variables. The ellipses depend on the motor speed which affects the magnitude of the ellipses whiles their center (λ_{af}/L_d,0) is not affected. In the same reference frame the current limit is a circle and the electrical torque curves are hyperbolas [73, 74]. Figure 5.4.1 shows the above mentioned curves. Fig. 5.4.1 will be used to demonstrate the effect of changing the PMs state while in the

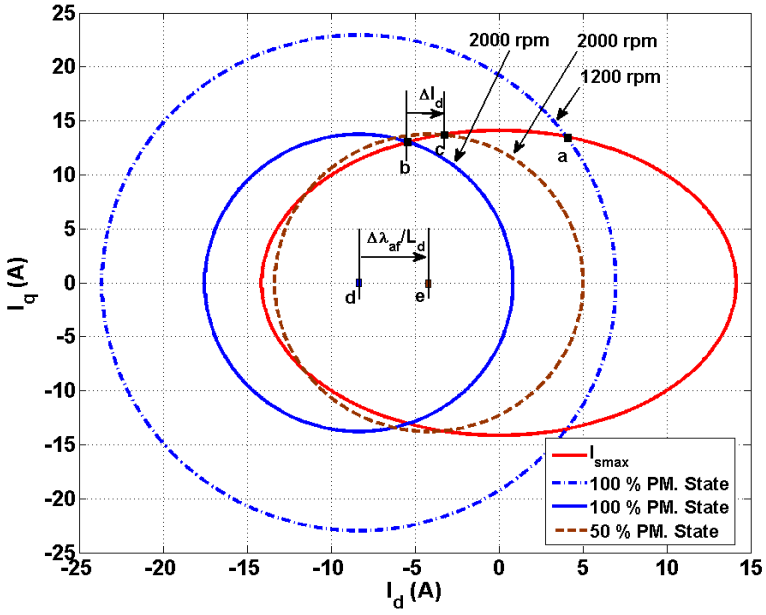

Figure 5.4.1: Voltage limits as speed dependent ellipses with d-q axis currents as variables

field weakening region. The base speed of the machine is 1200 rpm and as the speed is increased from 1200 to 2000 rpm, from the operating point 'a' along the current limit to point 'b'. When the PMs state is reduced to 50% (from point 'd' to 'e'), the operating point

moves from point 'b' to point 'c'. The d-axis current drops to point 'c' along the maximum current limit curve. Since the d-axis current drops there will be an increase in the q-axis current due to the load demand. This however does not mean that the torque will increase since there was a drop in the PMs flux linkage.

5.5 Variable Flux Machine Control

Wide speed operation is one of the key demands for PM machines. For a variable flux machine, at low speeds the machine can be operated with high magnet flux and low magnet flux at high speed region. Fig. 5.5.1 shows the proposed operation scenario during acceleration. At the initial state the machine is fully magnetized, then to achieve higher speeds as the induced load decreases, field weakening operation is initiated within a limited range. In typical operations of a non-variable flux machine, the field weakening operation would be maintained beyond the base speed point until maximum speed is reached. However that operation increases the stator current and hence the copper losses since the negative d-axis current is increased. However for the VFM as the load gets lighter the magnets are demagnetized to a certain percentage. This would effectively reduce the field weakening current and hence bring improvements to the efficiency of the machine.

5.5.1 Vector Control of the VFM

The vector control operation is constrained by the current limit and the voltage that could be supplied by the inverter. This voltage depends on the dc bus voltage supply. When the inverter runs out of voltage two things can be implemented. Firstly, the magnet flux can be reduced by injecting a negative d-axis current. Secondly, a constrained field weakening can be initiated. However when field weakening is implemented the negative d-axis current

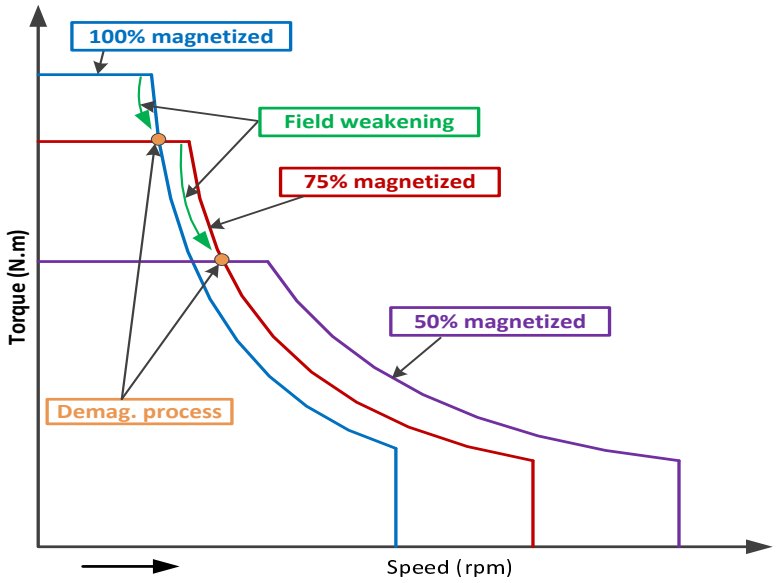

Figure 5.5.1: VFM during acceleration operation

will inherently de-magnetize the magnet. The constraint on the d-axis current will therefore limit the extent of de-magnetization on the magnets. Fig. 5.5.2 shows the proposed vector

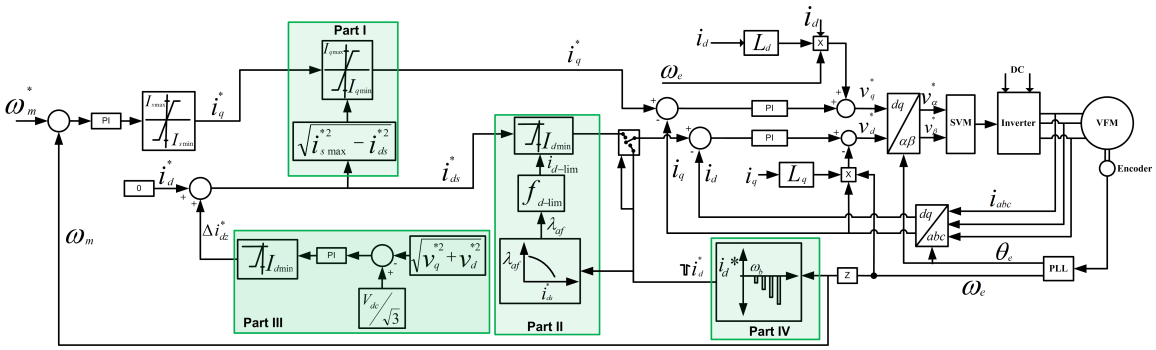

Figure 5.5.2: Variable f ux machine vector control drive

control strategy for the VFM. Part I, is concerned with the machine's current limit. At zero d-axis current, the maximum armature current will be completely determined by the q-axis current. However as the machine enters into f eld weakening, the d-axis current will gain magnitude and hence reduce the maximum q-axis current based on the current limit of the machine (i_{smax}).

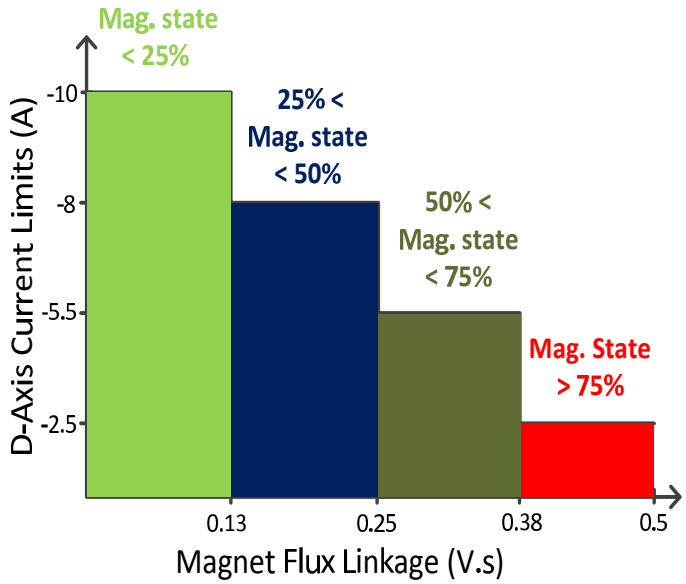

Figure 5.5.3: D-axis current limits depending on the magnetization states

The field weakening d-axis current is limited by the use of part II. The amount of d-axis current limit is based on the magnetization state. Fig. 5.5.3 shows the current limits depending on the PMs state. f_{d-limt} represents a table relating the PMs state and the d-axis current limits, that means each PMs state determines the d-axis current limit for the machine.

Part III, is concerned with the field weakening block and uses a PI controller to inject the negative d-axis current. The field weakening strategy does not therefore depend on the parameters of the machine but is based on the voltage limit from the inverter. That means even if the dc bus voltage dropped unintentionally the field weakening strategy will be initiated.

A current limiter is also placed at the output of the field weakening (FW) PI controller. This limit is based on the maximum negative d-axis current that can be allowed in the machine. When the maximum supply from the inverter is reached the out of the PI will

become negative. In part IV, the speed is used to determine the magnetization and de-magnetization points of the machine, hence the magnitudes of the d-axis current pulses.

5.6 Proposed Vector Controller Experimental Results

The VFM was driven from a two level inverter at a switching frequency of 5 kHz. The VFM was initially coupled to a resistive loaded dc generator. Fig. 5.6.1 shows the experimental test set-up. The PMs of the machine were initially magnetized with a d-axis curent pulse

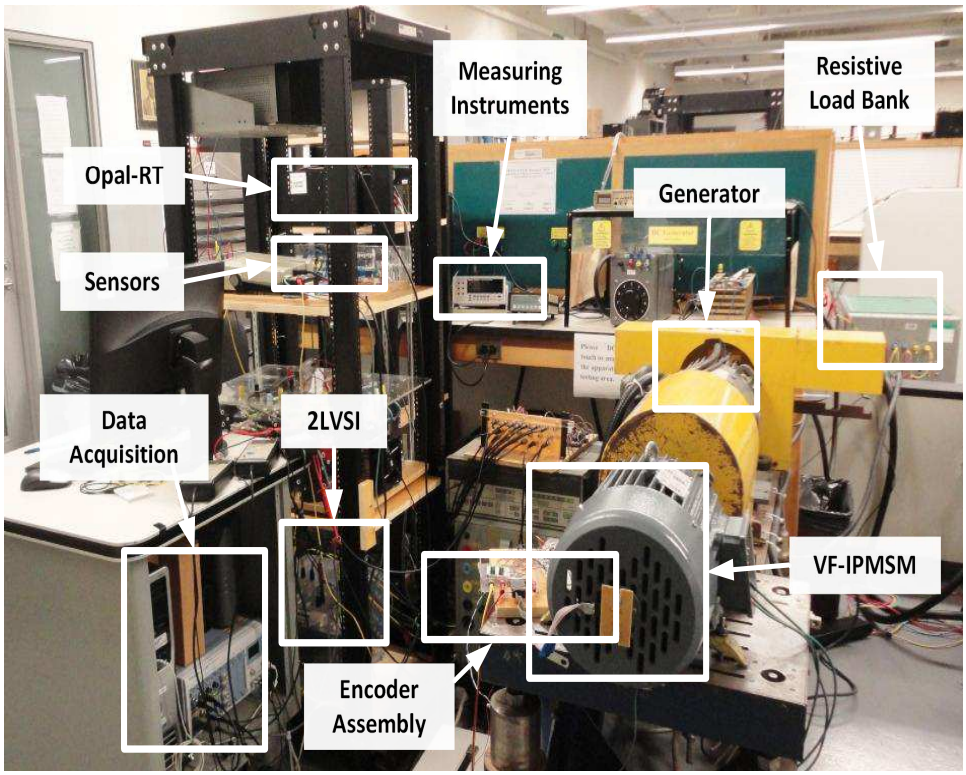

Figure 5.6.1: Experimental set-up

of 30 A. Fig. 5.6.2 shows the VFM operating under loaded condition. The machine was drawing approximately 9.5 A at approximately 1000 rpm. Fig. 5.6.3 shows the operation of machine under f eld weakening operation. For this operation the machine was not loaded. This was because the aim was to demonstrate the demagnetization operation in the FW

region.

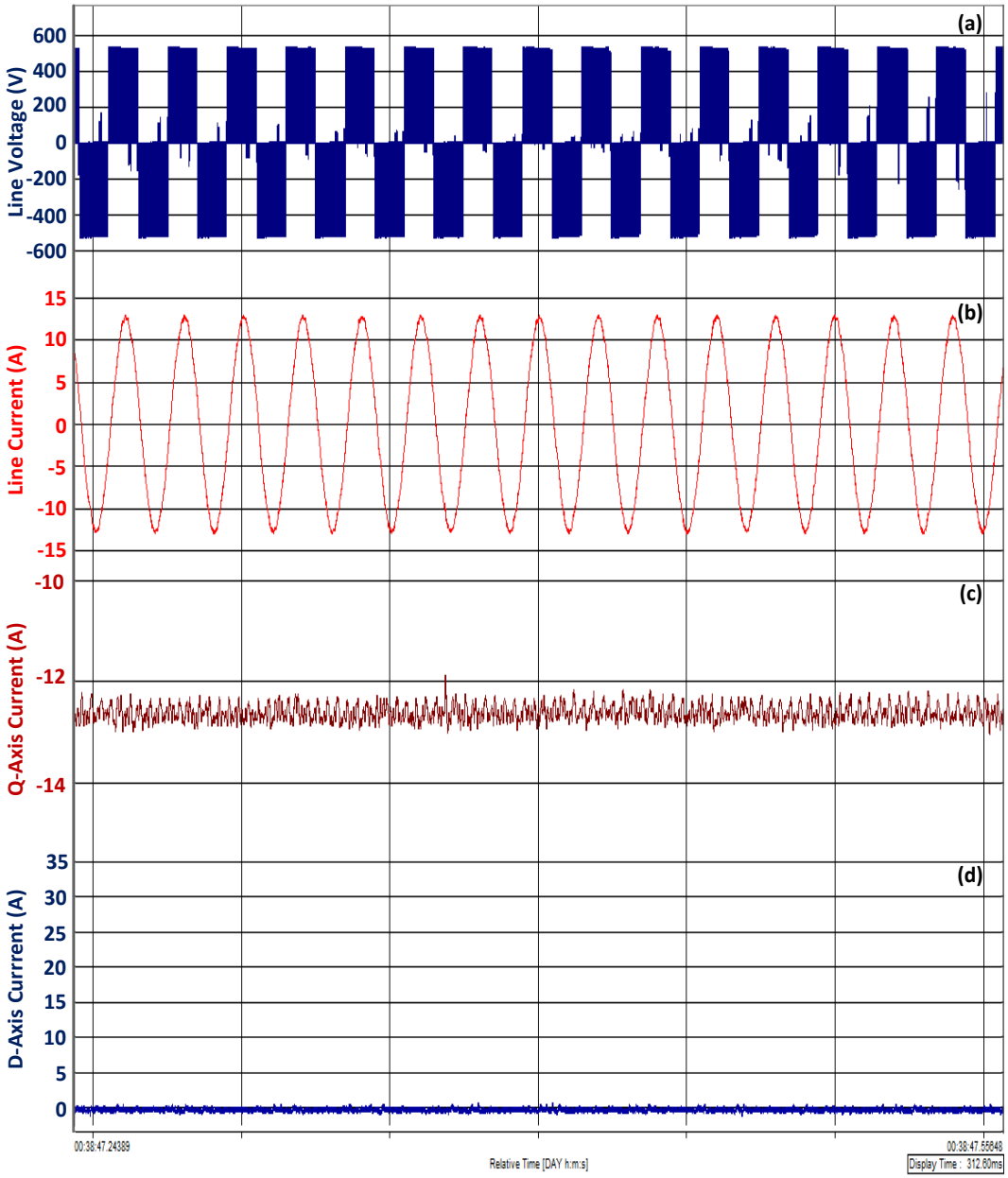

Figure 5.6.2: VFM under loaded condition

5.6.1 Demagnetization and FW Operation Under No Load Condition

To test the f eld weakening and the demagnetization operation the machine was run at no load with a reduced dc voltage. The dc voltage was reduced such that at (105 rad/s)

1000 rpm the modulation index was approximately 1. This would allow the field weakening operation to start at relatively 1000 rpm. Fig. 5.6.3 shows the results. The d-axis

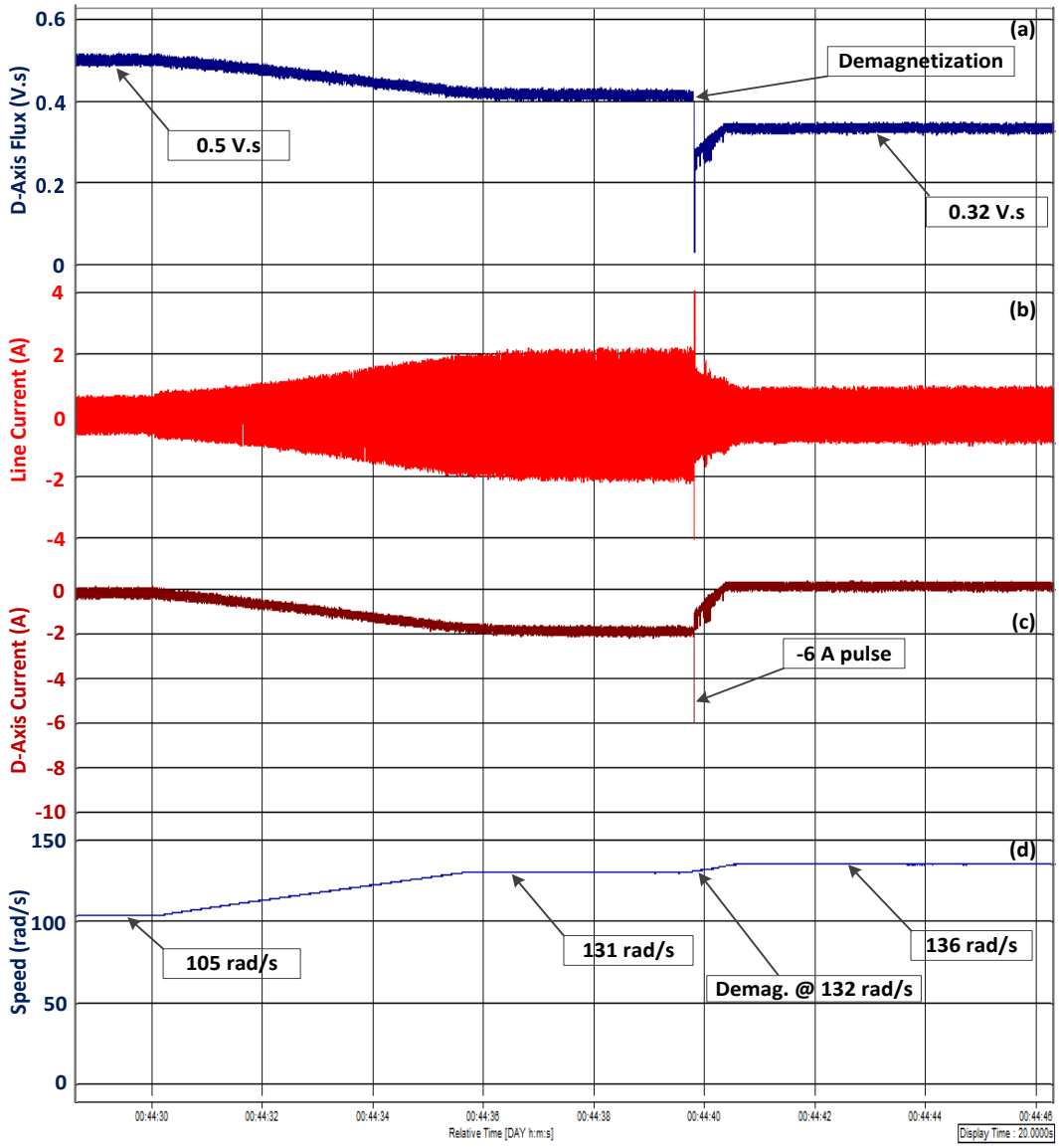

Figure 5.6.3: Demagnetization process in the FW region, (a) D-axis flux linkage, (b) Line current, (c) D-axis current and (d) Speed in rad/s

current was also initially set to zero and the reference speed was increased from 105 rad/s (1000 rpm) to 131 rad/s (1250 rpm). When the speed increased from 105 rad/s (1000 rpm) to 131 rad/s (1250 rpm) the input to the field weakening PI controller became negative

since the V_s was greater than what the inverter could supply ($V_{dc}/sqrt(3)$). The stator current increased due to the additional negative d-axis current.

The speed was further increased from 131 rad/s to 136 rad/s (1300 rpm) and at 132 rad/s the demagnetization pulse command of -6 A was initiated. Due to the demagnetization the d-axis magnet f ux was reduced from approximately 0.5 V.s to 0.32 V.s. The d-axis current returns to zero and the stator current is reduced.

However it can be seen that the initial magnitude of the stator current before f eld weakening is relatively smaller than the stator current after demagnetization. This is because the magnet f ux linkage dropped and the increase in stator current after demagnetization is due to the increase in the q-axis current to compensate for the reduced magnet f ux linkage. This compensation occurs naturally since the load torque remained relatively the same before and after demagnetization.

5.6.2 Demagnetization and FW Operation Under Loaded Condition

The VFM machine was coupled to a dc generator connected to the ABB drive. Fig. 5.6.4 shows the torque speed prof le of the VFM operated at 98% and 75% magnetization states. The f eld weakening (FW) region was generated such that the machine was operated at constant output power of approximatetly 4.4 hp and 3.5 hp for 98% (0.5 V.s) and 75% (0.38 V.s) magnetizations states respectively. The base speed of the VFM at 98% and 75% mgnetization states was at approximatetly 113.1 rad/s (1080 rpm) and 129.9 rad/s (1240 rpm) respectively. Fig. 5.6.5 shows the demagnetization operation of the VFM from 98% to 75% magnetization state under loaded condition. The VFM was run with a speed

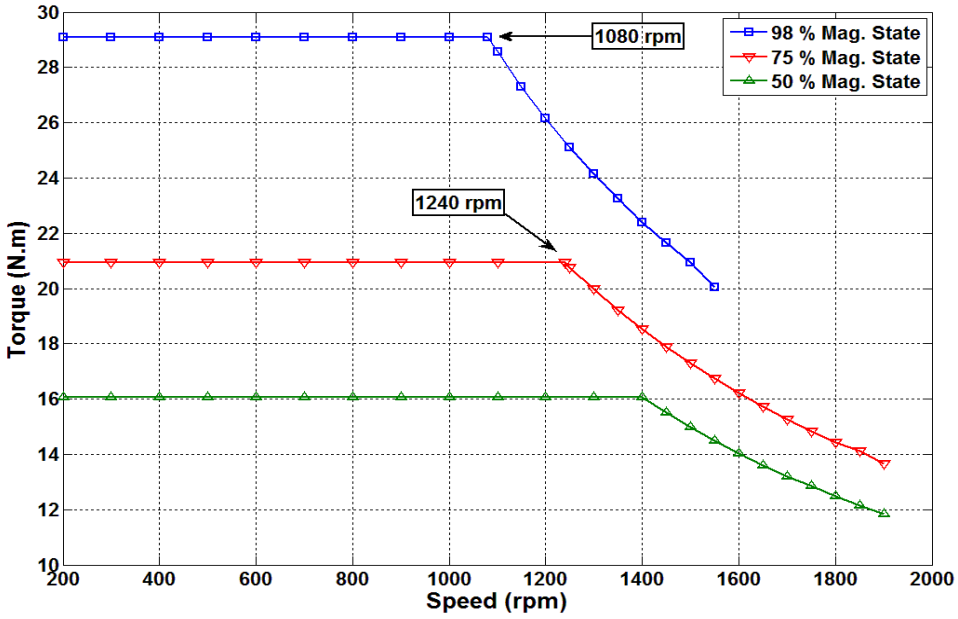

Figure 5.6.4: Torque speed curves for 98%, 75% and 50% magnet f ux state

ramp from 1080 rpm to 1240 rpm in 2.5 sec and at 125.7rad/s (1200 rpm) a demagnetization d-axis current of -5 A was initiated. This moved the machine to a new torque-speed prof le with the base speed at 1240 rpm. Fig. 5.6.5 shows that as the machine entered f eld weakening the d-xis f ux linkage dropped. This was due to the injection of the negative d-axis current in the machine. After the d-axis current demagnetization pulse the d-axis f ux linkage dropped to a new f ux linkage value of approximately 0.38 V.s.

5.6.3 Current Pulse Evaluation

The inverter was supplied from a step up transformer through a variac connected to the grid. The inverter has a rectif er for the supplied ac voltage from the grid. The remagnetization current pulse of 30 A has an effect on the dc supply voltage. Fig. 5.6.6 shows that as the VFM is re-magnetized the dc supply voltage dips from an initial voltage of 600 V to approximately 580 V. The dip in voltage is because of the high current demand from the supply. The time period of the pulse width was 50 ms. That means that during remagnetiza-

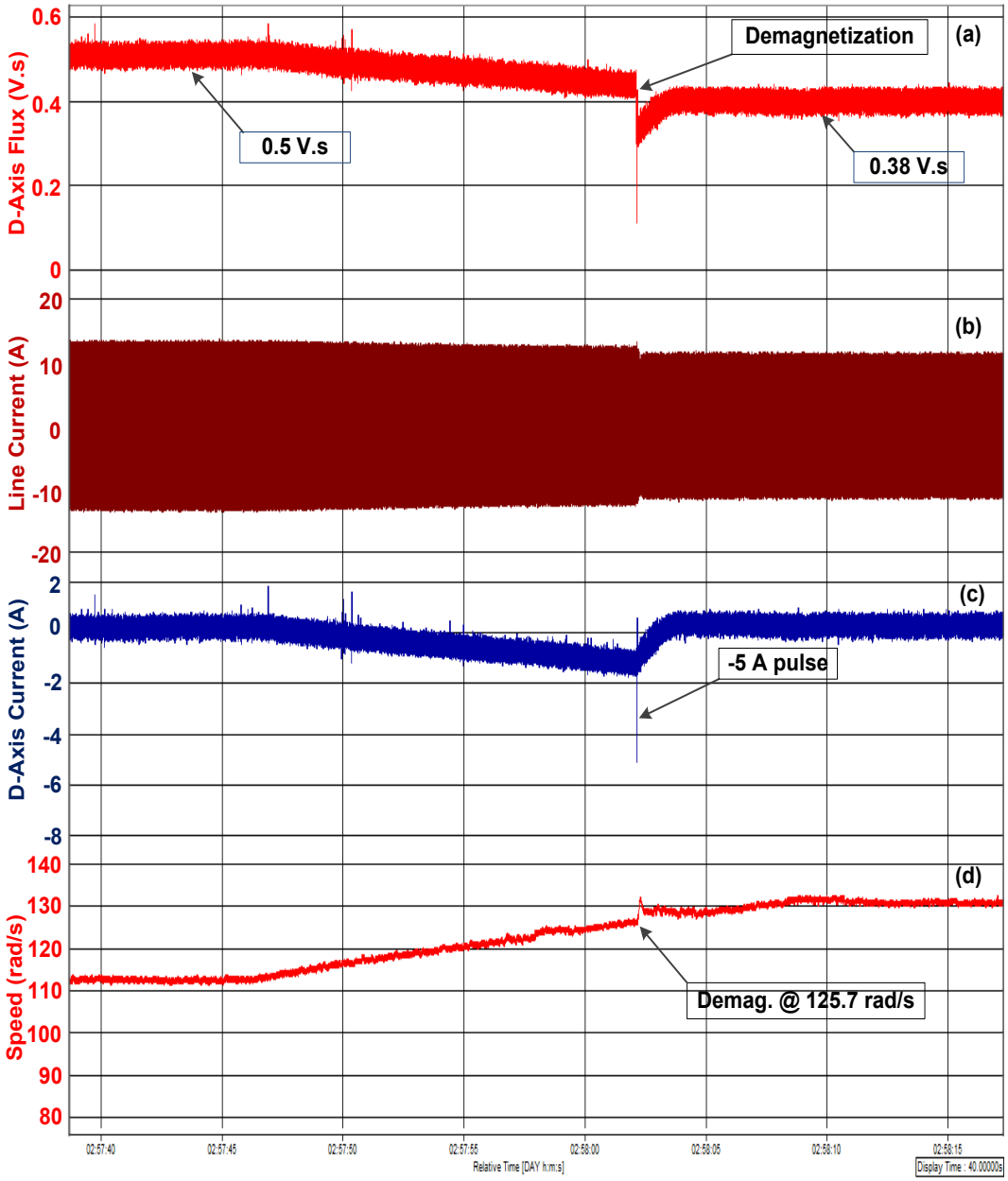

Figure 5.6.5: Demagnetization and FW operation under loaded condition, (a) D-axis f ux linkage, (b) Line current, (c) D-axis current and (d) Speed in rad/s

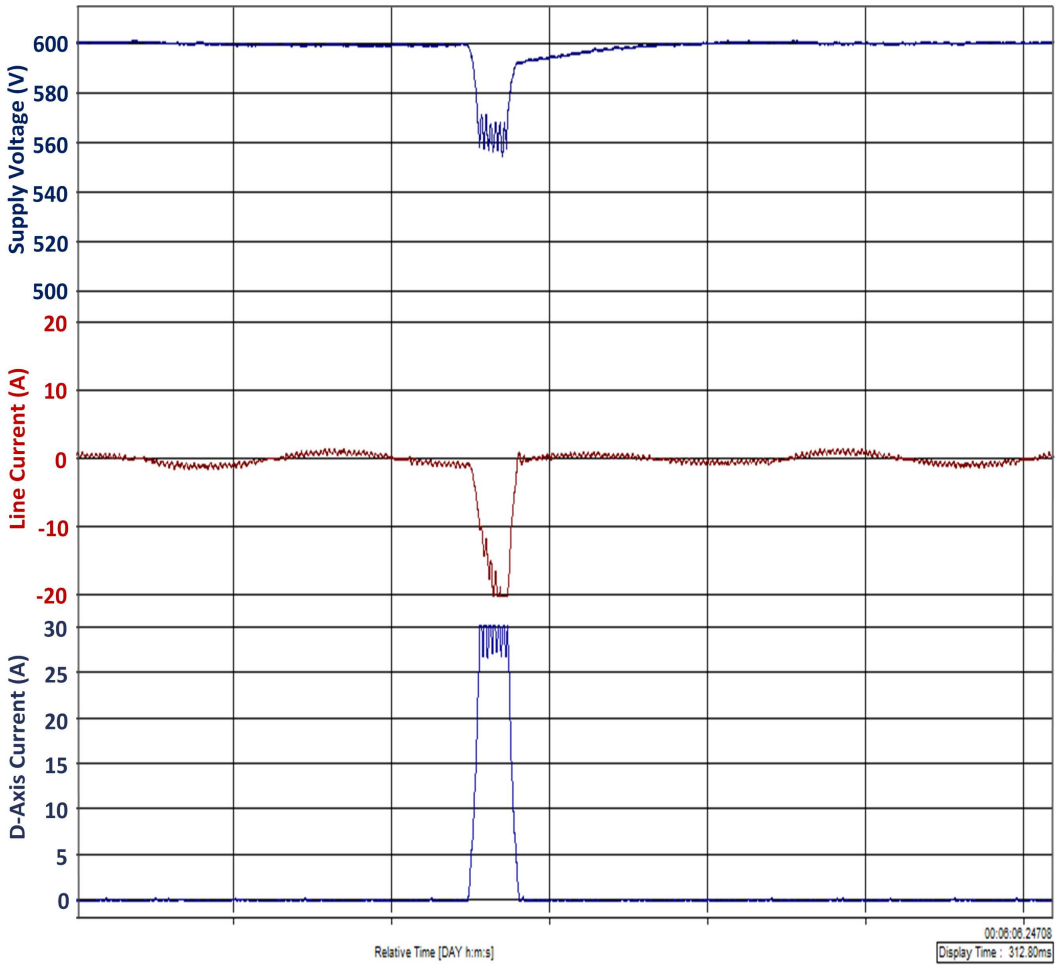

Figure 5.6.6: Magnetization current pulse effects on the dc supply voltage

tion the maximum inverter output voltage is reduced. This means that the VFM maximum speed is compromised during the period of remagnetization. However this effect can be reduced by reducing the time period of the re-magnetizing current. The re-magnetizing current period has to be long enough to fully magnetize all the magnets in the VFM.

5.7 Summary

This chapter demonstrated the use of the proposed vector controller on the operation of the VFM which uses AlNiCo magnets. It has been shown that VFM with AlNiCo magnets can be magnetized and demagnetized using the d-axis current pulse with the proposed vector controller. Due to the use of AlNiCo magnets the converter size can be reduced hence reducing the electric drive cost. The proposed control strategy also implemented a field weakening strategy for speed extension and takes into account the demagnetization properties of the AlNiCo magnets. Machine efficiency can be improved by operating the machine at low copper and iron losses by choosing the appropriate magnetization state. The core loss relationship with the magnet flux state was also illustrated. There was approximately 80% core loss difference between the 25% and 100% magnet states at 2000 rpm. The core loss experimental results serve as vital results for validating the core loss estimation model. The windage, friction and copper losses could easily be separated from the core losses of the VFM due to the ability to demagnetize the magnets in the VFM. The speed range of the machine can be extended by lowering the magnetization state of the PMs and hence reduce the copper losses due to a reduction in the field weakening current.

CHAPTER VI

CONCLUSION AND RECOMMENDATION

The conclusion of this thesis is summarized as follows:

6.1 Chapter 2

This work is concerned with the use of a three level inverter for a SynRM. A new three level inverter modulation algorithm was introduced. The sizing of the capacitors of a three level inverter using the size of the SynRM and other parameters was introduced. The saliency of the machine is not only critical for the performance of the machine but also the sizing of the dc link capacitors. Higher saliency means higher power factor which in effect contributes to the reduction of the dc link capacitors. A comparison between a two and three level inverter SynRM drives was also conducted. The three level inverter registers lower d-axis current ripple and lower current and voltage THD. The low d-axis current ripple indicated that the SynRM driven from a three level inverter had lower iron/core losses.

A comparison of two modulation schemes (mod-1 and Mod-2) was also conducted, both schemes balanced the dc link capacitors differently. There was a trade off on the overall eff ciency of the inverter between Mod-1 and Mod-2 modulation strategies. The d-axis current ripple was independent of the two modulation strategies. Mod-1 was modif ed so that the inverter could operate at a f xed switching frequency. Transients tests were also conducted on the proposed Mod-1 strategy, by changing the speed and load torque of the SynRM machine and the modulation strategy achived satisfactory results.

6.2 Chapter 3

This chapter is concerned with the cost reduction for the electric drive intended for traction applications. The accuracy of the position sensor was compared to that of a 12 bit industrial encoder and there was an error of less than 1 mechanical degree. Test were carried out during change of rotational direction and at relatively low speeds with acceptable torque ripple of less than 14%. An overview of the sources of the mechanical errors was also conducted. The low cost position sensor was also compared to the position sensor used in an electric power steering machine. The low cost position sensor has a higher resolution as compared to the position sensor used in the EPS machine The low cost position sensor has a relatively simpler algorithm for generating the position information as compared to the position sensor used in the EPS machine. The position sensor used in the EPS machine is relatively more costly than the low cost position sensor. The low cost position sensor is a good alternative for the EPS machine due to a relatively simpler algorithm for position information, higher resolution and cost reduction benef ts. The performance of the low cost position sensor was also tested on the EPS machine and a special SynRM and produced satisfactory results. One major disadvantage of the low cost position sensor is the position errors resulting from mechanical misalignments.

6.3 Chapter 4

A comparison between the core losses of a SynRM as a result of the three and two level inverter supply was conducted in this chapter. The use of a three level inverter on the SynRM produced lower core losses as compared to the use of a two level inverter. It was observed that the reduction of the core losses is more signif cant on the stator tooth than

on the stator yoke. The use of the three level inverter will hence reduce the burden of the cooling system on the machine. The effect of the switching frequency on the core losses between the two and three level inverters was also conducted. The three level inverter produced lower core losses while operated at 5 kHz and the two level inverter operated at 10 kHz. The effect of the switching frequency could be observed on the B-H curves.

6.4 Chapter 5

This chapter proposed a new vector controller drive for a variable flux machine using AlNiCo magnets. The controller took into account the demagnetization curve of the AlNiCo magnets. The VFM with AlNiCo magnets can be magnetized and demagnetized using the d-axis current pulse with the proposed vector controller. Due to the use of AlNiCo magnets the converter size can be reduced and hence reduction of the electric drive cost. The proposed control strategy which incoperates field weakening was also demonstrated. Machine efficiency can be improved by operating the machine at low copper and iron losses by choosing the appropriate magnetization state. The speed range of the machine can be extended by lowering the magnetization state of the PMs and hence reduce the copper losses due to a reduction in the field weakening current. The proposed controller was also tested during transients under no load and loaded condition.

The core loss performance of the VFM at different magnet flux levels was also illustrated. There was approximately 80% core loss difference between the 25% and 100% magnet states at 2000 rpm. The core loss experimental results serve as vital results for validating the core loss estimation model. The windage, friction and copper losses could easily be separated from the core losses of the VFM due to the ability to demagnetize the

magnets in the VFM. The effects of the re-magnetizing current pulse on the inverter were also conducted. During the magnetization pulse period, the speed range of the machine is reduced due to a drop in dc supply voltage.

6.5 Future Work

- The use of ultra capacitors to supply the magnetizing current in order to avoid the drop in the supply voltage
- Mitigation of the pulsating torque due to the manipulation of the q-axis current during remagnetization
- The use of the reluctance torque to improve the output power of the VFM machine
- Compensation algorithm for the low cost encoder due to mechanical misalignments at high speeds
- Development of low cost housing for the low cost position sensor assembly

REFERENCES

[1] J. Hu, J. Zou, F. Xu, Y. Li, and Y. Fu, "An improved pmsm rotor position sensor based on linear hall sensors," *Magnetics, IEEE Transactions on*, vol. 48, no. 11, pp. 3591–3594, Nov 2012.

[2] "Running on green power, electric vehicles: 2011-2020 qubec action plan." [Online]. Available: http://vehiculeselectriques.gouv.qc.ca/english/pdf/action-plan.pdf, Accesed on September 8, 2013

[3] Y. Takano, M. Takeno, T. Imakawa, A. Chiba, N. Hoshi, M. Takemoto, and S. Ogasawara, "Torque density and eff ciency improvements of a switched reluctance motor without rare earth material for hybrid vehicles," in *Energy Conversion Congress and Exposition (ECCE), 2010 IEEE*, 2010, pp. 2653–2659.

[4] M. Kamper, F. Van der Merwe, and S. Williamson, "Direct f nite element design optimisation of the cageless reluctance synchronous machine," *Energy Conversion, IEEE Transactions on*, vol. 11, no. 3, pp. 547–555, 1996.

[5] A. Boglietti and M. Pastorelli, "Induction and synchronous reluctance motors comparison," in *Industrial Electronics, 2008. IECON 2008. 34th Annual Conference of IEEE*, 2008, pp. 2041–2044.

[6] J. Germishuizen, F. Van der Merwe, K. Van der Westhuizen, and M. Kamper, "Performance comparison of reluctance synchronous and induction traction drives for electrical multiple units," in *Industry Applications Conference, 2000. Conference Record of the 2000 IEEE*, vol. 1, 2000, pp. 316–323 vol.1.

[7] A. Vagati, A. Fratta, G. Franceschini, and P. Rosso, "Ac motors for high-performance drives: a design-based comparison," *Industry Applications, IEEE Transactions on*, vol. 32, no. 5, pp. 1211–1219, 1996.

[8] A. Vagati, G. Franceschini, I. Marongiu, and G. Troglia, "Design criteria of high performance synchronous reluctance motors," in *Industry Applications Society Annual Meeting, 1992., Conference Record of the 1992 IEEE*, 1992, pp. 66–73 vol.1.

[9] A. Vagati, "The synchronous reluctance solution: a new alternative in ac drives," in *Industrial Electronics, Control and Instrumentation, 1994. IECON '94., 20th International Conference on*, vol. 1, 1994, pp. 1–13 vol.1.

[10] J. Malan and M. Kamper, "Performance of a hybrid electric vehicle using reluctance synchronous machine technology," *Industry Applications, IEEE Transactions on*, vol. 37, no. 5, pp. 1319–1324, 2001.

[11] J. Malan, M. Kamper, and P. Williams, "Reluctance synchronous machine drive for hybrid electric vehicle," in *Industrial Electronics, 1998. Proceedings. ISIE '98. IEEE International Symposium on*, vol. 2, 1998, pp. 367–372 vol.2.

[12] M. Ferrari, N. Bianchi, A. Doria, and E. Fornasiero, "Design of synchronous reluctance motor for hybrid electric vehicles," in *Electric Machines Drives Conference (IEMDC), 2013 IEEE International*, 2013, pp. 1058–1065.

[13] J. Rodriguez, J.-S. Lai, and F. Z. Peng, "Multilevel inverters: a survey of topologies, controls, and applications," *Industrial Electronics, IEEE Transactions on*, vol. 49, no. 4, pp. 724–738, Aug 2002.

[14] L. Tolbert, F. Z. Peng, and T. Habetler, "Multilevel converters for large electric drives," *Industry Applications, IEEE Transactions on*, vol. 35, no. 1, pp. 36–44, Jan 1999.

[15] H. Liu, N. Choi, and G. Cho, "Dsp based space vector pwm for three-level inverter with dc-link voltage balancing," in *Industrial Electronics, Control and Instrumentation, 1991. Proceedings. IECON '91., 1991 International Conference on*, oct-1 nov 1991, pp. 197 –203 vol.1.

[16] J. Zhang, "High performance control of a three-level igbt inverter fed ac drive," in *Industry Applications Conference, 1995. Thirtieth IAS Annual Meeting, IAS '95., Conference Record of the 1995 IEEE*, vol. 1, oct 1995, pp. 22 –28 vol.1.

[17] K. Yamanaka, A. Hava, H. Kirino, Y. Tanaka, N. Koga, and T. Kume, "A novel neutral point potential stabilization technique using the information of output current polarities and voltage vector," *Industry Applications, IEEE Transactions on*, vol. 38, no. 6, pp. 1572–1580, 2002.

[18] C. Newton and M. Sumner, "Neutral point control for multi-level inverters: theory, design and operational limitations," in *Industry Applications Conference, 1997. Thirty-Second IAS Annual Meeting, IAS '97., Conference Record of the 1997 IEEE*, vol. 2, Oct 1997, pp. 1336–1343 vol.2.

[19] N. Celanovic and D. Borojevic, "A comprehensive study of neutral-point voltage balancing problem in three-level neutral-point-clamped voltage source pwm inverters," in *Applied Power Electronics Conference and Exposition, 1999. APEC '99. Fourteenth Annual*, vol. 1, 1999, pp. 535–541 vol.1.

[20] J. Zaragoza, J. Pou, S. Ceballos, E. Robles, P. Ibaez, and J. Villate, "A comprehensive study of a hybrid modulation technique for the neutral-point-clamped converter," *Industrial Electronics, IEEE Transactions on*, vol. 56, no. 2, pp. 294–304, 2009.

[21] G. Orfanoudakis, M. Yuratich, and S. Sharkh, "Hybrid modulation strategies for eliminating low-frequency neutral-point voltage oscillations in the neutral-point-clamped converter," *Power Electronics, IEEE Transactions on*, vol. 28, no. 8, pp. 3653–3658, 2013.

[22] J. Pou, R. Pindado, D. Boroyevich, and P. Rodriguez, "Evaluation of the low-frequency neutral-point voltage oscillations in the three-level inverter," *Industrial Electronics, IEEE Transactions on*, vol. 52, no. 6, pp. 1582–1588, 2005.

[23] R. Trubenbach, A. Mackay, and M. Kamper, "Performance of a reluctance synchronous machine under vector control," in *Power Electronics Specialists Conference, 1993. PESC '93 Record., 24th Annual IEEE*, 1993, pp. 803–808.

[24] I. Boldea, *Reluctance Synchronous Machines and Drives, 1996 :Clarendon Press, Oxford*, 1996.

[25] G. Orfanoudakis, M. Yuratich, and S. Sharkh, "Nearest-vector modulation strategies with minimum amplitude of low-frequency neutral-point voltage oscillations for the neutral-point-clamped converter," *Power Electronics, IEEE Transactions on*, vol. 28, no. 10, pp. 4485–4499, 2013.

[26] J. Pou, D. Boroyevich, and R. Pindado, "New feedforward space-vector pwm method to obtain balanced ac output voltages in a three-level neutral-point-clamped converter," *Industrial Electronics, IEEE Transactions on*, vol. 49, no. 5, pp. 1026–1034, 2002.

[27] T. Matsuo and T. Lipo, "Rotor design optimization of synchronous reluctance machine," *Energy Conversion, IEEE Transactions on*, vol. 9, no. 2, pp. 359–365, 1994.

[28] A. Ostadrahimi and A. Radan, "Utilization of interleaved converter to improve battery performance in electric and electrical hybrid vehicles," in *Power Electronics, Drive Systems and Technologies Conference (PEDSTC), 2014 5th*, Feb 2014, pp. 624–628.

[29] A. T. N. from the Experts in Business-Critical Continuity. (2015, February) Effects of ac ripple current on vrla battery life. [Online]. Available: http://bit.ly/1COHygq

[30] U.-M. Choi, J.-S. Lee, and K.-B. Lee, "New modulation strategy to balance the neutral-point voltage for three-level neutral-clamped inverter systems," *Energy Conversion, IEEE Transactions on*, vol. 29, no. 1, pp. 91–100, March 2014.

[31] J. Pou, J. Zaragoza, P. Rodriguez, S. Ceballos, V. Sala, R. Burgos, and D. Boroyevich, "Fast-processing modulation strategy for the neutral-point-clamped converter with total elimination of low-frequency voltage oscillations in the neutral point," *Industrial Electronics, IEEE Transactions on*, vol. 54, no. 4, pp. 2288–2294, Aug 2007.

[32] A. Choudhury, P. Pillay, and S. Williamson, "Dc-link voltage balancing for a three-level electric vehicle traction inverter using an innovative switching sequence control scheme," *Emerging and Selected Topics in Power Electronics, IEEE Journal of*, vol. 2, no. 2, pp. 296–307, June 2014.

[33] W. Villet and M. Kamper, "Variable-gear ev reluctance synchronous motor drives-an evaluation of rotor structures for position-sensorless control," *Industrial Electronics, IEEE Transactions on*, vol. 61, no. 10, pp. 5732–5740, Oct 2014.

[34] R. Padilha Vieira, C. Cauduro Gastaldini, R. Zelir Azzolin, and H. Grundling, "Sensorless sliding-mode rotor speed observer of induction machines based on magnetizing current estimation," *Industrial Electronics, IEEE Transactions on*, vol. 61, no. 9, pp. 4573–4582, Sept 2014.

[35] R. Morales-Caporal, E. Bonilla-Huerta, M. Arjona, and C. Hernandez, "Sensorless predictive dtc of a surface-mounted permanent-magnet synchronous machine based on its magnetic anisotropy," *Industrial Electronics, IEEE Transactions on*, vol. 60, no. 8, pp. 3016–3024, Aug 2013.

[36] R. Cardenas, R. Pena, S. Alepuz, and G. Asher, "Overview of control systems for the operation of df gs in wind energy applications," *Industrial Electronics, IEEE Transactions on*, vol. 60, no. 7, pp. 2776–2798, July 2013.

[37] N. Patel, T. O'Meara, J. Nagashima, and R. Lorenz, "Encoderless ipm traction drive for ev/hev's," in *Industry Applications Conference, 2001. Thirty-Sixth IAS Annual Meeting. Conference Record of the 2001 IEEE*, vol. 3, 2001, pp. 1703–1707 vol.3.

[38] R. Mizutani, T. Takeshita, and N. Matsui, "Current model-based sensorless drives of salient-pole pmsm at low speed and standstill," *Industry Applications, IEEE Transactions on*, vol. 34, no. 4, pp. 841–846, 1998.

[39] M. Corley and R. Lorenz, "Rotor position and velocity estimation for a salient-pole permanent magnet synchronous machine at standstill and high speeds," *Industry Applications, IEEE Transactions on*, vol. 34, no. 4, pp. 784–789, 1998.

[40] Y. Kano, T. Kosaka, N. Matsui, T. Takahashi, and M. Fujistuna, "Design of saliency-based sensorless drive ipm motors for hybrid electric vehicles," in *Energy Conversion Congress and Exposition (ECCE), 2012 IEEE*, 2012, pp. 4362–4369.

[41] Z. Chen, M. Tomita, S. Doki, and S. Okuma, "An extended electromotive force model for sensorless control of interior permanent-magnet synchronous motors," *Industrial Electronics, IEEE Transactions on*, vol. 50, no. 2, pp. 288–295, 2003.

[42] Y. Kano, T. Kosaka, N. Matsui, T. Takahashi, and M. Fujitsuna, "Signal-injection-based sensorless ipm traction drive for wide-torque range operation at low speed," in *Energy Conversion Congress and Exposition (ECCE), 2012 IEEE*, 2012, pp. 2284–2291.

[43] J. Finch and D. Giaouris, "Controlled ac electrical drives," *Industrial Electronics, IEEE Transactions on*, vol. 55, no. 2, pp. 481–491, Feb 2008.

[44] C.-W. Hung, C.-T. Lin, C.-W. Liu, and J.-Y. Yen, "A variable-sampling controller for brushless dc motor drives with low-resolution position sensors," *Industrial Electronics, IEEE Transactions on*, vol. 54, no. 5, pp. 2846–2852, Oct 2007.

[45] S.-Y. Kim, C. Choi, K. Lee, and W. Lee, "An improved rotor position estimation with vector-tracking observer in pmsm drives with low-resolution hall-effect sensors,"

Industrial Electronics, IEEE Transactions on, vol. 58, no. 9, pp. 4078–4086, Sept 2011.

[46] Z. Zhu, Y. F. Shi, and D. Howe, "Rotor position sensing in brushless ac motors with self-shielding magnets using linear hall sensors," *Journal of Applied Physics*, vol. 99, no. 8, pp. 08R313–08R313–3, Apr 2006.

[47] R. Ramakrishnan, A. Gebregergis, M. Islam, and T. Sebastian, "Effect of position sensor error on the performance of pmsm drives for low torque ripple applications," in *Electric Machines Drives Conference (IEMDC), 2013 IEEE International*, 2013, pp. 1166–1173.

[48] H. Cai, B. Guan, and L. Xu, "Low cost ferrite pm assisted synchronous reluctance machine for electric vehicles," pp. 1–1, 2014.

[49] B. Aslan, J. Korecki, T. Vigier, and E. Semail, "Inf uence of rotor structure and number of phases on torque and f ux weakening characteristics of v-shape interior pm electrical machine," *Journal of Energy and Power Engineering, Transactions on*, vol. 6, pp. 1461–1471, Sept 2012.

[50] J. Bangura and N. Demerdash, "Simulation of inverter-fed induction motor drives with pulse-width modulation by a time-stepping coupled f nite element-f ux linkage-based state space model," *Energy Conversion, IEEE Transactions on*, vol. 14, no. 3, pp. 518–525, Sep 1999.

[51] J.-J. Lee, Y.-K. Kim, H. Nam, K.-H. Ha, J.-P. Hong, and D.-H. Hwang, "Loss distribution of three-phase induction motor fed by pulsewidth-modulated inverter," *Magnetics, IEEE Transactions on*, vol. 40, no. 2, pp. 762–765, March 2004.

[52] A. Boglietti, P. Ferraris, and M. Lazzari, "Induction motor iron losses measurement with a static converter supply using a slotless rotor test bench," *Magnetics, IEEE Transactions on*, vol. 30, no. 6, pp. 4599–4601, Nov 1994.

[53] M. Kawabe, T. Nomiyama, A. Shiozaki, H. Kaihara, N. Takahashi, and M. Nakano, "Behavior of minor loop and iron loss under constant voltage type pwm inverter excitation," *Magnetics, IEEE Transactions on*, vol. 48, no. 11, pp. 3458–3461, Nov 2012.

[54] N. Kurita, K. Onda, K. Nakanoue, and K. Inagaki, "Loss estimation method for three-phase ac reactors of two types of structures using amorphous wound cores in 400-kva ups," *Power Electronics, IEEE Transactions on*, vol. 29, no. 7, pp. 3657–3668, July 2014.

[55] M. Malinowski, S. Stynski, W. Kolomyjski, and M. Kazmierkowski, "Control of three-level pwm converter applied to variable-speed-type turbines," *Industrial Electronics, IEEE Transactions on*, vol. 56, no. 1, pp. 69–77, Jan 2009.

[56] K. Ma and F. Blaabjerg, "Thermal optimised modulation methods of three-level neutral-point-clamped inverter for 10 mw wind turbines under low-voltage ride through," *Power Electronics, IET*, vol. 5, no. 6, pp. 920–927, July 2012.

[57] L. Masisi, P. Pillay, and S. S. Williamson, "Introduction to a three level npc inverter dc capacitor sizing for a synchronous reluctance machine drive," in *Energy Conversion Congress and Exposition (ECCE), 2014 IEEE*, 2014, submitted.

[58] A. Boglietti, P. Ferraris, M. Lazzari, and F. Profumo, "Energetic behavior of soft magnetic materials fed by inverter supply," in *Industry Applications Society Annual Meeting, 1992., Conference Record of the 1992 IEEE*, 1992, pp. 54–59 vol.1.

[59] ——, "Iron losses in magnetic materials with six-step and pwm inverter supply [induction motors]," *Magnetics, IEEE Transactions on*, vol. 27, no. 6, pp. 5334–5336, 1991.

[60] A. Boglietti, M. Lazzari, and M. Pastorelli, "About the choice of the reference magnetic quantity in presence of non sinusoidal waveforms," *Magnetics, IEEE Transactions on*, vol. 33, no. 5, pp. 4002–4004, 1997.

[61] T. Mthombeni and P. Pillay, "Lamination core losses in motors with nonsinusoidal excitation with particular reference to pwm and srm excitation waveforms," *Energy Conversion, IEEE Transactions on*, vol. 20, no. 4, pp. 836–843, Dec 2005.

[62] A. Boglietti, P. Ferraris, M. Lazzari, and M. Pastorelli, "About the possibility of def ning a standard method for iron loss measurement in soft magnetic materials with inverter supply," *Industry Applications, IEEE Transactions on*, vol. 33, no. 5, pp. 1283–1288, Sep 1997.

[63] A. Boglietti, A. Cavagnino, M. Lazzari, and M. Pastorelli, "Predicting iron losses in soft magnetic materials with arbitrary voltage supply: an engineering approach," *Magnetics, IEEE Transactions on*, vol. 39, no. 2, pp. 981–989, Mar 2003.

[64] R. Liu, C. Mi, and D. Gao, "Modeling of eddy-current loss of electrical machines and transformers operated by pulsewidth-modulated inverters," *Magnetics, IEEE Transactions on*, vol. 44, no. 8, pp. 2021–2028, Aug 2008.

[65] K. Sakai, K. Yuki, Y. Hashiba, N. Takahashi, and K. Yasui, "Principle of the variable-magnetic-force memory motor," in *Electrical Machines and Systems, 2009. ICEMS 2009. International Conference on*, Nov 2009, pp. 1–6.

[66] C. Yu and K. Chau, "Design, analysis, and control of dc-excited memory motors," *Energy Conversion, IEEE Transactions on*, vol. 26, no. 2, pp. 479–489, June 2011.

[67] V. Ostovic, "Memory motors," *Industry Applications Magazine, IEEE*, vol. 9, no. 1, pp. 52–61, Jan 2003.

[68] K. Sakai, H. Hashimoto, and S. Kuramochi, "Principle and basic characteristics of hybrid variable-magnetic-force motors," in *Power Electronics and Applications (EPE 2011), Proceedings of the 2011-14th European Conference on*, Aug 2011, pp. 1–10.

[69] T. Kato, N. Limsuwan, C.-Y. Yu, K. Akatsu, and R. Lorenz, "Rare earth reduction using a novel variable magnetomotive force f ux-intensif ed ipm machine," *Industry Applications, IEEE Transactions on*, vol. 50, no. 3, pp. 1748–1756, May 2014.

[70] C. Yu, T. Fukushig, N. Limsuwan, T. Kato, D. Reigosa, and R. Lorenz, "Variable f ux machine torque estimation and pulsating torque mitigation during magnetization state manipulation," *Industry Applications, IEEE Transactions on*, vol. PP, no. 99, pp. 1–1, 2014.

[71] N. Limsuwan, T. Kato, K. Akatsu, and R. Lorenz, "Design and evaluation of a variable-f ux f ux-intensifying interior permanent-magnet machine," *Industry Applications, IEEE Transactions on*, vol. 50, no. 2, pp. 1015–1024, March 2014.

[72] M. Ibrahim and P. Pillay, "Design of high torque density variable f ux permanent magnet machine using alnico magnets," in *Energy Conversion Congress and Exposition (ECCE), 2014 IEEE*, Sept 2014, pp. 3535–3540.

[73] M. Zordan, P. Vas, M. Rashed, S. Bolognani, and M. Zigliotto, "Field-weakening in high-performance pmsm drives: a comparative analysis," in *Industry Applications Conference, 2000. Conference Record of the 2000 IEEE*, vol. 3, 2000, pp. 1718–1724 vol.3.

[74] T. Jahns, "Flux-weakening regime operation of an interior permanent-magnet synchronous motor drive," *Industry Applications, IEEE Transactions on*, vol. IA-23, no. 4, pp. 681–689, July 1987.

[75] Austriamicrosystems. (2014, March) As5215 datasheet (pdf) austriamicrosystems ag. [Online]. Available: http://www.alldatasheet.com/datasheet-pdf/pdf/427493/AMSCO/AS5215.html

APPENDIX A

MACHINE PARAMETERS AND HARDWARE CONFIGURATIONS

A.1 Parameters of the electrical machines

Table A.1.1 shows the parameters of the SynRM and Figs. A.1.1 and A.1.2 shows the measured d-q inductances and the unoptimized prototyped rotor design of the SynRM respectively. Table A.1.2 shows the parameters of the VFM and

Table A.1.1: SynRM machine parameters

Line voltage V_{L-L}	220 V
Rated stator line current (delta) I_{L-L}	16.5 A
Rated induction machine stator	5 hp
Number of pole pairs P	2
Phase resistance R_s	0.9 Ω

Table A.1.2: Variable f ux machine parameters

Rated speed/ current	1080 rpm/9.5 A
Rated torque	29 N.m
Phase resistance R_s	1.3 Ω
D-axis inductance L_d	53 mH
Q-axis inductance L_q	36 mH
Magnet f ux λ_{af}	0 to 0.51 V.s
Connection	Wye

A.2 Low Cost Position Sensor Program

The low cost position sensor IC (AS5215) comes with factory settings which have relatively low amplitudes of the sine and the cosine signals. However it allows for the factory settings

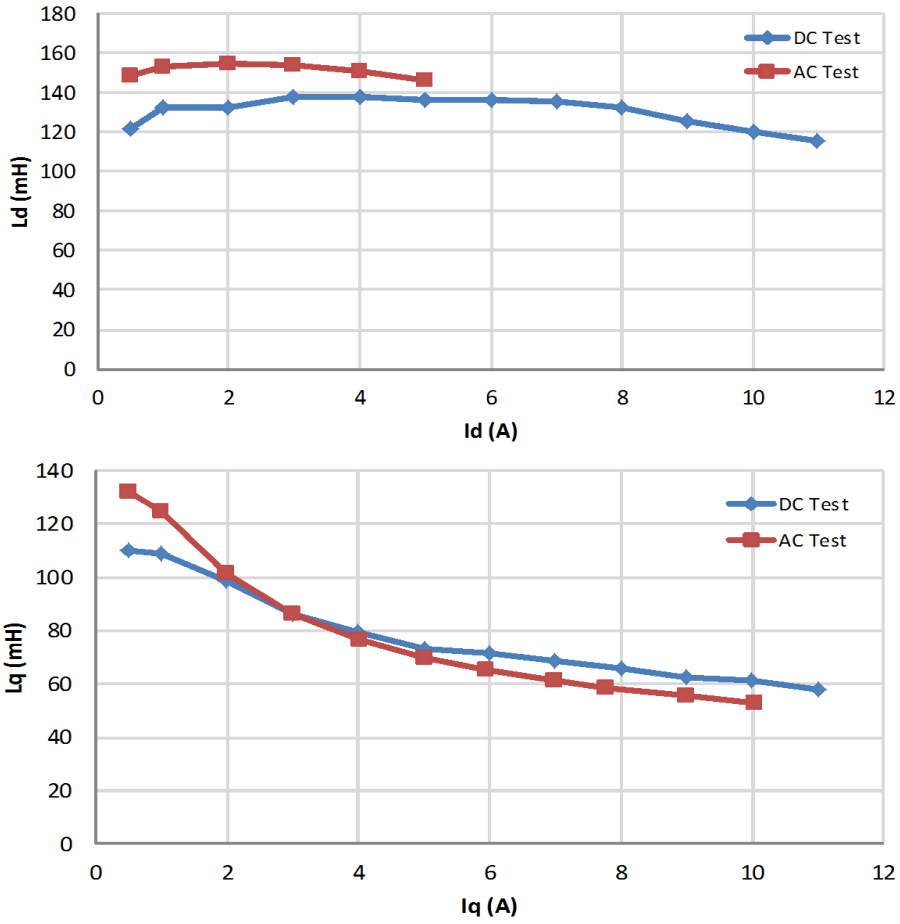

Figure A.1.1: Measured d-q inductances of the SynRM

to be changed, more details cab be found at [75]. Fig. A.2.1 shows the PIC micro-controller that was used for the programming of the OTP of the sensor IC.

A.3 Inverter Dead Time Circuit

The dead time is necessary for avoiding a short connection on the inverter switches. The dead time circuit was designed to create a 2 μ sec dead time. Fig. A.3.1 shows the dead time circuit. The PCB board was designed by the use of a KiCad software.

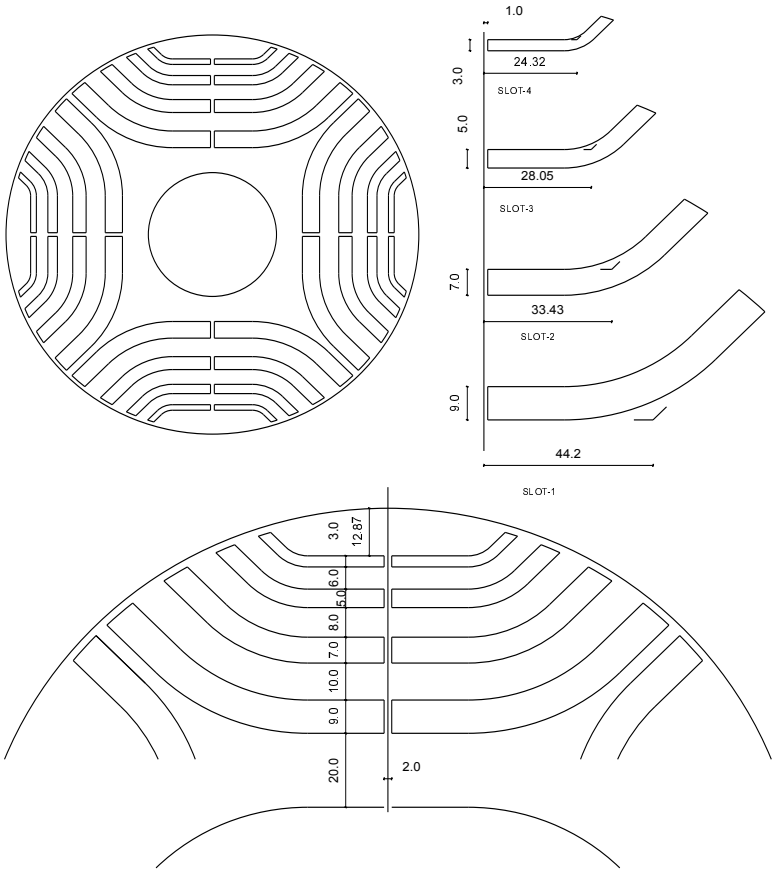

Figure A.1.2: Unoptimized rotor design

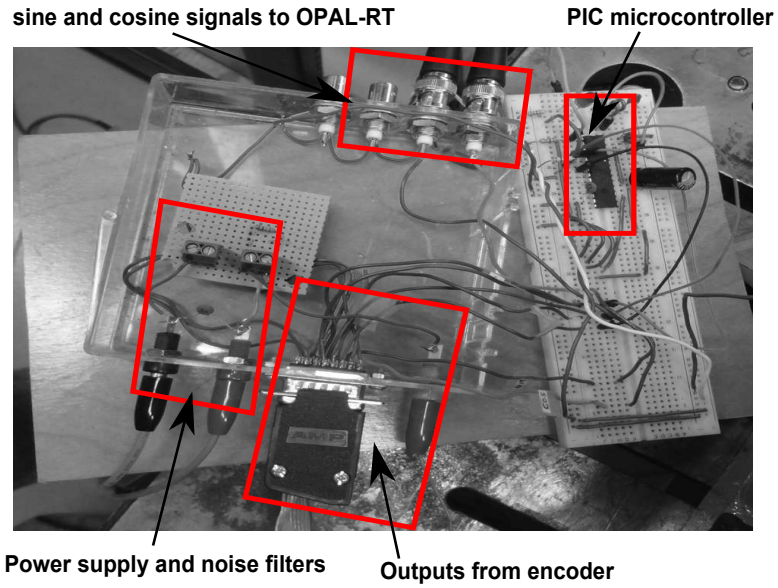

Figure A.2.1: Low cost encoder signal processing and programming

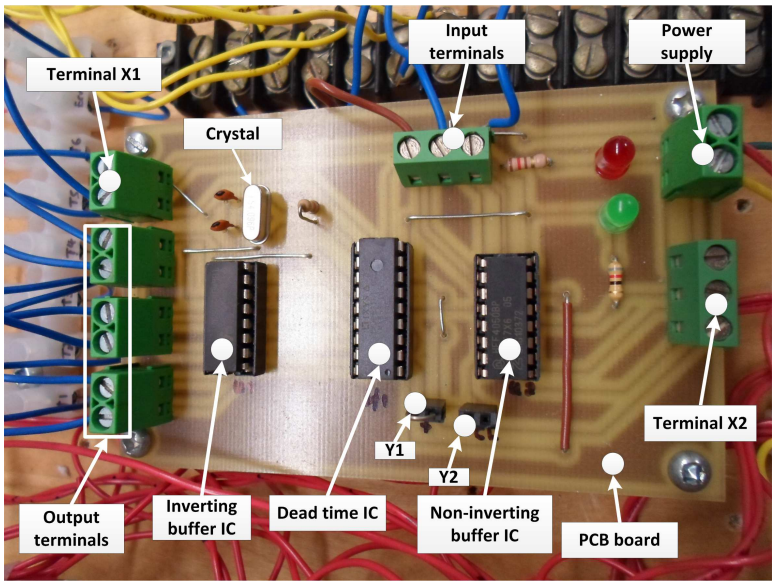

Figure A.3.1: Dead time circuit for inverters